THE OCCURRENCE OF VISCOUS SHEAR HEATING WITHIN THE COLD ROLLING PROCESS

L. Kampstra | s2767163 | Master Mechanical Engineering

Master thesis report

Enschede, June 25, 2024

Author

L. Kampstra
s2767163
Cohort: 2021

Education

University of Twente
Drienerlolaan 5, 7522 NB, Enschede
Faculty: Engineering Technology
Master: Mechanical Engineering
Specialization: High Tech Systems & Materials
Group: Surface Technology & Tribology

Extern Company

Tata Steel Nederland Technology B.V.
Wenckebachstraat 1, 1951 JZ, Velsen-Noord
Department: Research & Development
Group: Rolling, Finishing and Measurement

Supervisors

Tata Steel: L. Jacobs
1st supervisor UT: N.F. Bader
2nd supervisor UT: M. de Rooij

Abstract

One of the steps within the steel-making process is cold rolling, where steel strips are reduced in thickness. A typical cold mill consists of multiple stands, each providing a reduction in strip thickness. To improve the process, an emulsion consisting of water and oil, is used to lubricate and cool the process. However, it can be assumed that due to difference in viscosity, neat oil enters the work zone.

The contact between the strip and the work roll typically occurs in the mixed lubrication regime, where the load is partly carried by asperity contact and partly by the lubricant. Most friction models neglect viscous shear, as friction from asperity contact is significantly higher than that from lubrication. However, previous studies have shown that viscous shear can not be neglected.

Viscous shear is the internal friction of fluid layers within the lubrication film. At very low shear rates, the lubricant behaves as a Newtonian fluid, but at more substantial shear rates the lubricant exhibits shear thinning which can be described by the Eyring model. At really high shear rates, the lubricant can experience thermal effects. Heat generation within the film causes the viscosity to decrease and consequently results in a reduction of the shear stress, also known as viscous shear heating.

This thesis investigates the occurrence of viscous shear heating in the cold rolling process and whether it should be incorporated into friction models. The starting point of viscous shear heating is determined with a limiting isothermal shear rate, indicated by $\dot{\gamma}_L$. A shear rate exceeding this limiting isothermal shear rate induces viscous shear heating.

To investigate the behavior of a typical cold rolling lubricant, a mini traction machine is used. This mini traction machine is a ball-on-disc experiment, which allows to measure the traction of the lubricant at elasto-hydrodynamic contact. This setup allows measurements in a steady-state full film regime, focusing only on the behavior of the lubricant used at Tata Steel, without asperity contacts.

Experiments showed that viscous shear heating starts to occur at $\dot{\gamma}_L \approx 2 \times 10^5\ s^{-1}$ under certain testing conditions. The results indicated that the occurrence of viscous shear heating is influenced by both pressure and temperature. Therefore the limiting isothermal shear rate is obtained as a function of the temperature and pressure. Higher pressure or lower temperature causes viscous shear heating to occur at lower shear rates.

Part of the cold rolling contact can also operate within this range of shear rates, indicating that viscous shear heating can be expected in the cold rolling process. By considering the operating pressure, temperature, and other operational conditions for each stand of the cold mill, it can be determined if viscous shear heating occurs. By comparing the actual shear rate in a stand to the limiting isothermal shear rate, it can be concluded that viscous shear heating occurs within the last stands of the cold mill. This is mainly due to higher pressures and shear rates resulting from increased sliding speeds and reduced film thicknesses.

Acknowledgements

Hereby I would like to thank the following people who helped and supported me throughout my thesis.

Firstly I would like to thank Erik de Vries for his assistance in the lab and helping me with thinking about solutions to the problems that I encountered while testing.

I would also like to thank my UT supervisor Norbert Bader for always finding some time to answer questions, help me with my testing procedure and teaching me the needed background knowledge about EHL contacts.

A third acknowledgement goes out to my second UT supervisor, Matthijn de Rooij, for his feedback and guidance throughout my thesis.

Another special thanks goes out to Leon Jacobs for his guidance throughout my graduation project, teaching me the necessary background information about tribology within the cold rolling process, help me with my report and answering my questions.

Last but not least, I would like to thank my friends, fellow students and family for mentally supporting me with the process where needed and prevent me from working day and night.

Further acknowledgments goes out to everyone who has contributed, directly or indirectly, for the completion of this thesis.

Thank you all.

Nomenclature

Abbreviations

Abbreviation	Meaning
BL	Boundary of Lubrication
CoF	Coefficient of Friction
CM	Cold Mill
EHL	Elasto Hydrodynamic Lubrication
IE	Isoviscous Elastic
IR	Isoviscous Rigid
ML	Mixed Lubrication
MTM	Mini Traction Machine
NP	Neutral Point
PE	Piezoviscous Elastic
PR	Piezoviscous Rigid
RMS	Root Mean Square
SRR	Slide-to-Roll Ratio

Symbols

Greek symbol	Meaning	Unit
α	pressure viscosity coefficient	Pa^{-1}
β	Temperature coefficient	$°C^{-1}$
$\dot{\gamma}$	Shear rate	s^{-1}
η	Viscosity	$Pa\,s$
θ	Inlet angle	Rad
λ	Film parameter	$-$
μ	Friction coefficient	$-$
ν	Poissons ratio	$-$
σ	Stress	Pa
τ	Shear stress	Pa

Roman symbol	Meaning	Unit
A	Contact area	m^2
E	Elasticity modulus	Pa
F	Force	N
G	Shear modulus	Pa
h	Film thickness	m
L	Contact arc length	m
p	Pressure	Pa
q	Hydro-static pressure	Pa
R	Surface roughness	m
r	Radius	m
S	Slip	$\%$
T	Temperature	$°C$
t	Strip thickness	m
U	Entrainment speed	m/s
u	Velocity	m/s
x	Distance in rolling direction	m
z	viscosity-pressure parameter	$-$

Contents

1 Introduction

This chapter provides an introduction to the subject of the research field. This research project is in collaboration with the University of Twente and Tata Steel in the Netherlands. Tata Steel is one of the leading steel producers around the world with operations in 26 countries. The steel production process, characterized by its complexity and extensive duration requires ongoing research to enhance understanding and optimization. The Research & Development department at Tata Steel is engaged in optimizing the steel production process. One of the steps in the overall steel production is the cold rolling process which reduces steel strips from a thickness range of $2-6\,mm$ to $0.2-2\,mm$. While the process of squeezing a metal strip between two rollers seems simple and straightforward, the interactions involved are complex requiring diverse studies including tribological, mechanical, metallurgical and studies within control theory. Tribology is the study of interacting bodies in motion and includes the aspects of friction, lubrication and wear.

1.1 Cold rolling process

As the name implies, the steel that is reduced by the cold mill is relatively cold, indicating that the steel remains well below the recrystallization temperature. In practise the steel strips remain below $200\,^{\circ}C$. Cold rolling induces severe plastic deformation leading to lattice distortion within the crystal structure. This results in increased material hardness (strain-hardening) and yield stress while reducing its ductility. The deformation of the strip can be considered as plane strain, because the strip width remains constant. A reduction in thickness results in a corresponding elongation as volume remains unchanged. [1, 2]

There are several types of cold mill installations such as two-high, four-high and cluster mills. A four-high mill consists of four rolls vertically aligned. Tata Steel utilizes 4 or 5 stands of four-high mills in a row, also known as tandem. A schematic representation of the four-high tandem mill is shown in Figure 1. The steel strip passes through five stands of four-high mills, each contributing to a reduction in thickness. The relatively small diameter of the work roll (3), approximately $d = 0.5\,m$, requires less force for steel deformation than a big work roll, due to small contact area to distribute the forces. A downside of a slender work roll is that it results in deflection and therefore an exit strip with a non-uniform thickness reduction over the width. The work rolls bend in a similar manner to a loaded beam supported at both ends [3]. To increase the stiffness and decrease the deflection, back-up rolls (2) are installed to support the work rolls. These back-up rolls are 2.5 to 3 times larger than the working rolls. The uncoiler (1) unwinds and provides steel for the mill, while the coiler (5) at the end winds up the steel.

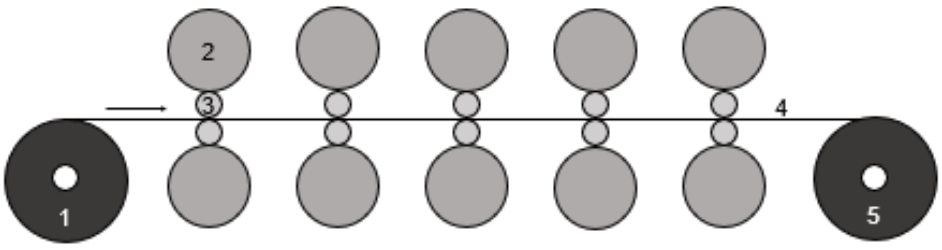

Figure 1: Schematic overview of a 5 stands cold mill with four-high mills, where 1 represents the uncoiler, 2 the back up roll, 3 the work roll, 4 the strip and 5 the uncoiler.

After the cold rolling process, the coils undergo further processes like annealing, temper rolling and potential coating before it is dispatched to the customer. Customers can be from diverse sections, such as automotive, packaging and white goods.

1.1.1 General cold rolling theory

As the strip passes through a stand of the cold mill, it comes into contact with the work roll. The contact zone between the strip and the work roll is called the roll bite and is shown in Figure 2 by the dashed lines.

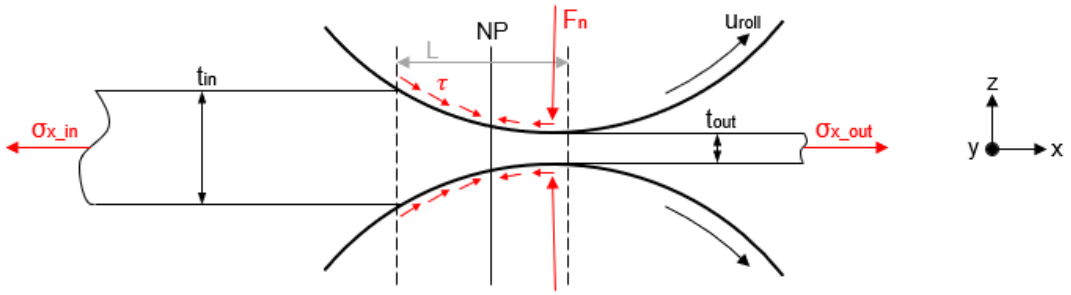

Figure 2: Schematic overview of the Neutral point in a cold rolling process.

In the roll bite, the workpiece undergoes changes in velocity due to elongation. As the workpiece passes through the roll bite, its velocity increases due to elongation. While the workpiece increases its velocity, the velocity of the work roll remains constant. The point where the velocity of the work roll equals the tangential velocity of the workpiece is known as the neutral point (NP) and is a fundamental aspect in cold rolling. For stable cold rolling, the velocity of the work roll is higher than the entry speed and lower than the exit speed of the strip. This indicates that the neutral point lays within the contact arc length, denoted by L.

The relative speed difference between the work roll and the strip is called slip. A forward slip at the exit of the roll bite indicates that the exit speed of the strip is greater than the speed of the work roll. A neutral point located within, but closely to the end of the contact arc length means that the exit speed of the strip is almost equal to the speed of the work roll, which minimizes forward slip. The exact position of the NP can not be established by direct measurements, but can be indicated by determining the forward slip S_{fw}, which can be calculated with the following equation:

$$S_{fw} = \frac{u_{strip} - u_{roll}}{u_{roll}} \cdot 100\% \tag{1}$$

where u_{strip} is the strip exit speed and u_{roll} the rolling speed [3].

Shear stresses between the work roll and workpiece are caused by sliding speed. Before the neutral point the velocity of the work roll is higher than the strip, which causes shear stresses on the strip in the forward direction, as can be seen in Figure 2. At the neutral point, the shear stresses changes direction as the velocity of the strip is higher than that of the work roll. The optimum placement of the neutral point is close to the exit of the roll bite for providing process stability and avoiding mill chatter [4].

The strip shown in Figure 2 undergoes plastic deformation within the roll bite, where it experiences compression in the z-direction, resulting in a stress state. An equivalent stress of this stress state can be computed by Von Mises (right side of Equation 2). Plastic deformation takes place when the equivalent stress in the workpiece is equal to the flow stress which is the stress required to deform material, see Equation 2, representing the von Mises yield criterion:

$$\sigma_{flow} = \sqrt{\frac{(\sigma_x - \sigma_y)^2 + (\sigma_y - \sigma_z)^2 + (\sigma_z - \sigma_x)^2 + 6(\tau_{xy}^2 + \tau_{zy}^2 + \tau_{zx}^2)}{2}} \tag{2}$$

where σ_x is the stress in the rolling direction, σ_y the stress in the width direction and σ_z the stress in the thickness direction. The shear stresses in their respective directions are denoted by τ.

Front and back strip tensions reduces the normal pressure needed for this deformation. A higher mean normal pressure on the workpiece within the contact arc length requires a higher normal force of the work mills. However, the cold mills are limited by a maximum normal force they can exert, making it essential to control pressure and friction. A typical pressure distribution curve (also known as friction hill) along the contact arc length shows a peak located at the NP as illustrated in the bottom graph of Figure 3. The total area underneath the pressure distribution curve corresponds to the total mill force.

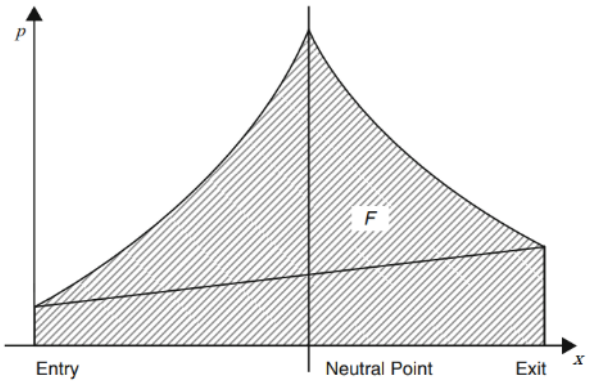

Figure 3: Pressure hill distribution within the roll bite over the rolling direction x, divided into top and bottom section by division line. Adapted from [5].

The pressure difference between the exit and entry points arises from strain-hardening. A division line connecting the entry and exit pressure is shown to separate the pressure hill in a top and bottom section. The bottom section beneath the division line, shown in Figure 3 represents the contact pressure necessary for achieving ideal plastic deformation. This area increases with low front and back tensions or with high material yield strength. Conversely, the area in the top section represents the pressure needed to overcome frictional forces. This region is increased when the process is poorly lubricated and the friction forces are high. This results in a higher peak leading to higher forces on the mills which are beyond the limitation. Controlling and regulating friction and lubrication in the roll bite is therefore extremely important.

1.1.2 Friction in the cold rolling process

The interaction between the work rolls and the strip involving microscopic surface peaks, known as asperities causes friction, which is a crucial factor in cold rolling and could be advantageous or disadvantageous [3]. Excessive friction demands a normal force beyond the limitation of the mill, while insufficient friction leads to skidding and the workpiece will remain motionless [4]. Therefore it is important to monitor the friction and keep it in an optimum range to prevent an unstable rolling process.

The roll bite coefficient of friction (CoF) expresses the ratio of tangential and normal stress. Several factors influence the CoF, such as roll roughness, roll surface hardness, strip hardness, lubrication, temperature, and mill speed. The CoF increases with higher Root Mean Square (RMS) surface roughness and temperatures, while it decreases with proper lubrication and higher mill speed [3]. An increase in the CoF results in a shift of the neutral point towards the start of the contact arc length, while a lower CoF shifts the neutral point to the exit of the roll bite.

1.1.3 Lubrication in the cold rolling process

A cooling system is crucial in cold rolling to facilitate heat removal generated by friction and plastic deformation. Usually a cooling system incorporates high-pressure sprays directed at the workpiece and work roll. An ideal emulsion composition should provide both high thermal conductivity and high heat capacity. The emulsion consists mainly of water ($95 - 99\%$), serving as a coolant and a small percentage of oil ($1 - 5\%$) which serves as a lubricant. Tandem mills are normally equipped with a recirculating oil system, ensuring continuous recycling of the emulsion throughout the cold rolling process.

A distinction can be made between stable and unstable emulsion and is dependent on the mixture stability of the oil in water. As the name implies an unstable emulsion has a low emulsion stability index and consists of large oil droplets in the water when agitated. Leaving this emulsion without agitation, the oil will be totally separated from the water. A stable emulsion consists of a stable mixture of oil and water, due to the addition of emulsifiers which prevents the oil micelles from coalescing [4]. The oil droplets in a stable emulsion are relatively small compared to an unstable emulsion. The composition of a rolling oil consists mainly of base esters, emulsifiers, mineral oil, EP/AW additives, viscosity additives, pH stabilizers and anti-foam additives. The base esters serve to establish a bond between the oil and the surface of the strip, involving the interaction of negative oxygen atoms with the positive iron atoms.

Lubricant entrainment
As stated before, the oil in the emulsion provides lubrication in the roll bite, with two distinct mechanisms facilitating this lubrication. The oil can access the roll bite due to plate out, enrichment or a combination of both. Plate out occurs when the oil forms a layer on the strip, as illustrated in (Figure 4a).

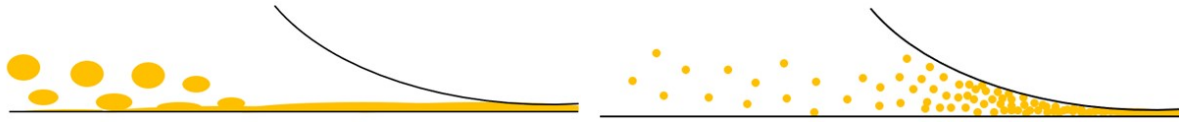

(a) Plate out lubrication (b) Enrichment lubrication

Figure 4: Entrainment of oil into the roll bite.

A stable emulsion may fail to provide effective plate out lubrication as the oil droplets lack time to disengage from the water and adhere to the workpiece's surface. Conversely, a dispersion provides favorable plate out lubrication. Enrichment is an increase in oil concentration just before the roll bite entry. This phenomenon, as illustrated in (Figure 4b), occurs at higher viscosity and larger oil droplets which draws the oil into the roll bite, resulting in a shift from an oil-in-water to a water-in-oil emulsion. Although approximately 1% of water enters the roll bite, this proportion is negligible, allowing the lubrication to be considered as neat oil [6]. In the cold rolling process, the lubrication will enter the roll bite through a combination of enrichment and plate out.

1.2 Objectives of this research

The aim of this research is to determine the relevant rheological parameters of an industrial rolling oil used for the cold rolling process at Tata Steel. In particular the possibility of viscous shear heating in the cold rolling process will be investigated. The fundamental understanding of friction, the three different lubrication regimes and the behavior of lubrication oil in the cold rolling process is therefore necessary. This research project aligns with the currently ongoing PhD-project "Friction in Cold Rolling" by Leon Jacobs. From this main objective, the following objectives can be deduced:

- Obtain the fundamental understanding of the underlying theory on friction and lubrication in the cold rolling process.
- Determine the relevant rheological parameters of the lubrication oil that is currently used at Tata Steel.
- Establish when viscous shear heating occurs in the lubrication oil.
- Predict whether viscous shear heating takes place in the cold rolling process.

The obtained knowledge of this research can be used as a tool in further studies and research of the optimization of lubrication in the cold rolling process.

1.3 Outline of this thesis

This thesis is organized into several chapters, each contributing distinct elements to the overall research. The current chapter serves as an introduction explaining the subject and states the objectives of the research study. The following chapter is the literature study and delves into the existing theoretical background related to friction and lubrication in the cold rolling process and the rheological behavior of a lubrication oil. The research gap of this literature review and problem definition is stated at the end of this chapter. Chapter 3 focuses on the methodology on how to obtain the desired results and explains the equipment, specimens and experimental methods. The results obtained from these experiments will be provided in chapter 4 and discussed in the following chapter, which contains a detailed interpretation and discussion regarding these results. The conclusion can be found in chapter 6 and summarises the key findings and answers the research questions stated in subsection 2.7.1. The final chapter is dedicated to any recommendations and the appendices can be found at the end of the thesis report.

2 Fundamentals of friction models in the cold rolling process and rheology of lubricants

One of the first models for the cold rolling process was developed by von Karman [7] in 1925. von Karman layed the basis for the well-known slab method using the coulomb friction law. The slabmethod is based on a differential equation of the interface pressure between the surfaces of the roll and the workpiece by stating the equilibrium equations on a strip segment in the roll bite [8]. Such a strip segment is illustrated in Figure 5, where x is the rolling direction. With this method the pressure distribution can be calculated along the roll bite. In these friction models the lubrication is left out and it is assumed that the CoF is constant along the roll bite, but experimental measurements by Liu et al. [9] state otherwise.

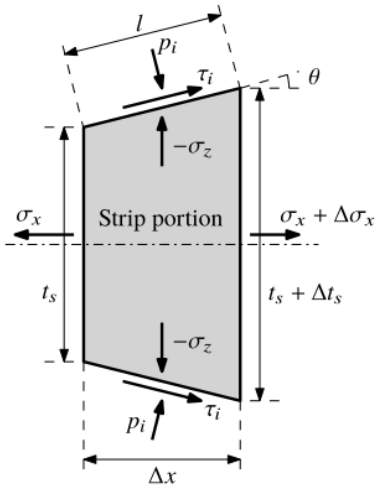

Figure 5: A strip segment of width Δx exhibits various stresses, adapted from [8].

As stated before the lubrication film thickness plays a significant role in the value of the CoF. Laugier et al. [10] looked into flexible lubrication concepts to adapt the amount of oil supply in the cold rolling process to control the friction coefficient, while Guillaument [11] et al. focused on the plate out mechanism to apply the lubricant. The lubrication theory took off in 1886 when Reynolds [12] developed a method to describe the pressure change in a lubricant in a converging gap for which is the case in the cold rolling process. The Reynolds equation can be simplified for the cold rolling process, which is a one dimensional steady state process, to the following equation [13]:

$$\frac{\partial}{\partial x}\left[\frac{\rho h^3}{\eta}\frac{\partial \rho}{\partial x}\right] = 6(u_{Roll} + u_{strip})\frac{\partial(\rho h)}{\partial x} + 6\rho h\frac{\partial(u_{Roll} + u_{Strip})}{\partial x} \tag{3}$$

Where η is the viscosity, ρ the density and h the film thickness. A shooting method to solve the Reynolds equation numerically has been obtained by Marsault [14] and a finite difference method to obtain the film thickness is used by Qiu et al. [15].

2.1 Models for the film thickness

Multiple researchers have studied and experimented on the film thickness in the cold rolling process. Wilson and Walowit [16] recognized the necessity of including the yield stress of the workpiece and came up with an equation for the film thickness for isothermal hydrodynamic lubrication. One of the experiments to determine the film thickness in the cold rolling process

is the oil droplet method first introduced by Saeki and Hashimoto [17] and further explained by Azushima [18]. This technique involves placing an oil droplet on the workpiece and roll it through the mill. The thickness of the film can be calculated using the volume of the applicated oil droplet and the area of the spread out oil. Cuperus [19] found good reproducibilty of the oil droplet method in his experiments. Other researchers such as Zhu [20] and Cassarini [21] delved into the film thickness with oil-in-water emulsion lubrication. Zhu experimented with a cylinder-on-disk method and confirmed that the lubrication film thickness is dependent on speed. He discovered that as speed surpasses a first critical value, a transition phase takes place where no stable oil pool forms, marked by fluctuating film thickness and decreasing local oil concentration in the inlet zone. Beyond a second critical speed, film thickness stabilizes and increases consistently, reflecting a constant local oil concentration similar to bulk lubricant supply. The film thickness for oil-in-water emulsions in the inlet zone is also studied by Cassarini, he developed a model for the lubricant film formation by the dynamic concentration mechanism.

Jacobs [22] showed that the film thickness is dependent on the inlet angle of the work roll compared to the workpiece. A factor that influences the inlet angle, thus the lubrication film, is roll flattening due to elasticity of the work rolls. Tsau and Sargent [23] show that this factor is important and needs attention when looking into friction and lubrication in the roll bite. There are several researchers that studied and developed models involving roll flattening. Hitchcock [24] and Bland and Ford [25] included roll flattening into their models by increasing the radius of the work roll, thus circular roll flattening as shown in Figure 6a. Additionally non-circular roll flattening, illustrated in Figure 6b, was introduced by Jortner et al. [26] and Boemer [8] worked with this method in his model for cold rolling.

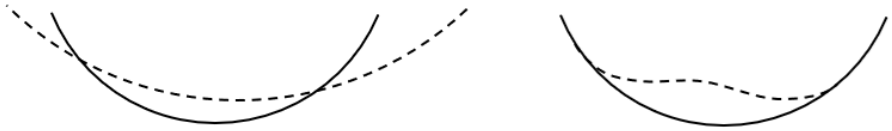

(a) Circular (b) Non-circular

Figure 6: Roll flattening, where the solid line represents the undeformed work roll and the dashed line the deformed worked roll.

Azushima [6] studied the importance of taking thermal effects into account when calculating the inlet film thickness. He derived equations related to the Reynolds equation and the energy equation to determine the film thickness, considering factors such as pressure and temperature which influences the viscosity of the lubricant. The study revealed significant differences in oil film thickness with and without thermal effects. Without thermal effects, the film thickness is linear on Log-Log scale compared to the speed. However when taking thermal effects into account, the film thickness shows non-linear behavior on the Log-Log scale. A decrease in film thickness is revealed for a combination of elevated relative speeds and viscosity as shown in Figure 7.

2.2 Different lubrication regimes

In the cold rolling process, the lubrication between the roll and the workpiece is an important factor that influences the rolling force and the quality of finished strip. Lubrication can be classified into three different regimes: hydrodynamic, mixed and boundary lubrication (Figure 8). Hydrodynamic or full film lubrication implies complete separation of the work roll and the strip by an oil film layer. In this regime, the lubricant film carries the entire load, preventing direct contact between the surfaces. Boundary lubrication is in contrast with hydrodynamic lubrication and comes into play when the lubricant film thickness is negligible in comparison to the surface roughness. In this case, the load is fully carried by the asperity contact. This regime may occur

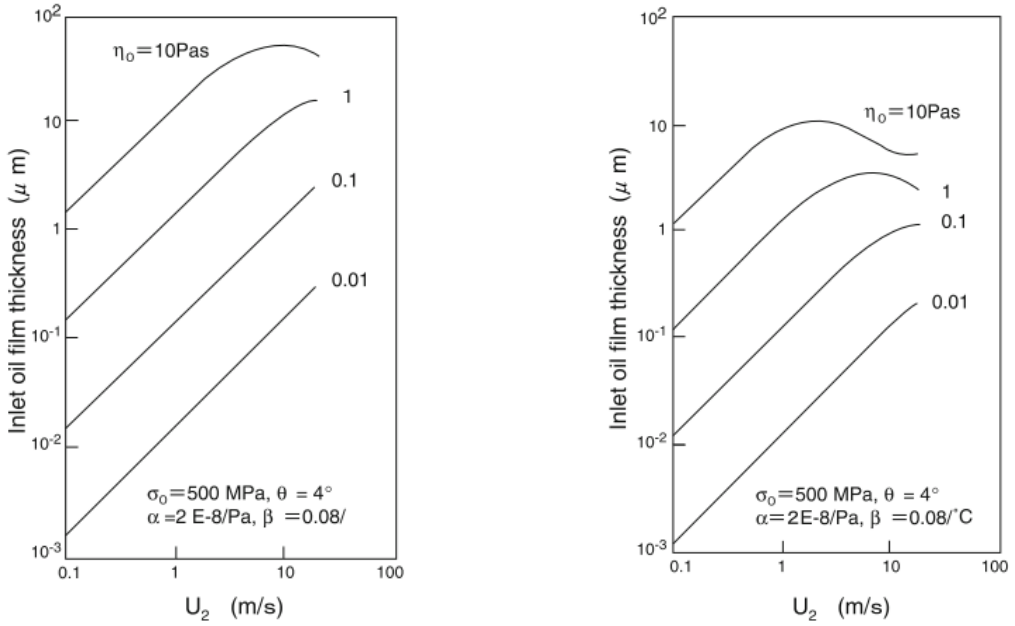

(a) Relative speed 0.1 (b) Relative speed 0.4

Figure 7: Relationship between inlet oil film thickness and roll speed using lubricants with different viscosities of 0.01, 0.1, 1, and 10 Pa s. Model conditions at a yield stress of $\sigma_0 = 500\ MPa$, semi inlet angle of $\theta = 4°$, pressure coefficient of $\alpha = 2e-8\ Pa^{-1}$ and a temperature coefficient of $\beta = 0.08\ °C^{-1}$. Adapted from [6].

at very low rolling speeds, high surface roughness or when the lubrication exhibits very low viscosity. The regime most relevant in the cold rolling process is the mixed lubrication regime, where the film thickness is in the same order of the surface roughness. In this regime, the load is carried partly by the lubricant film and partly by the asperity contact. To determine the active lubrication regime, the film parameter λ can be calculated using the following equation.

$$\lambda = \frac{h}{\sqrt{\left[R^2_{q.strip} + R^2_{q.roll}\right]}} \tag{4}$$

Where h represents the lubricant film thickness and R_q the surface roughness.

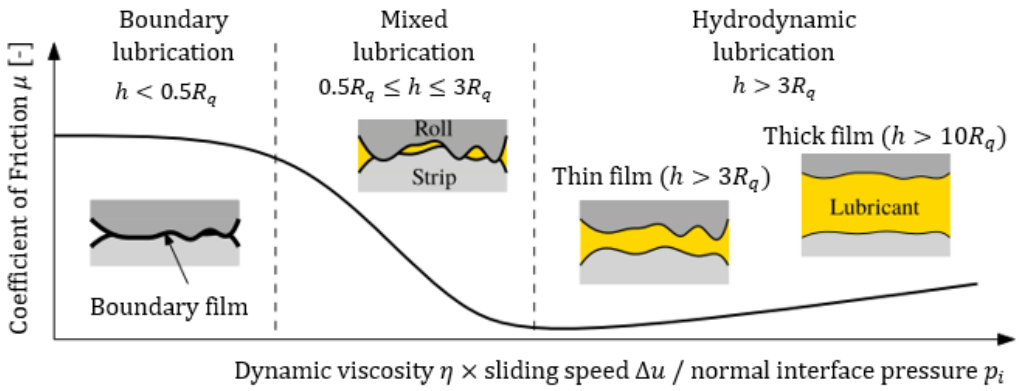

Figure 8: Division of the three lubrication boundary regimes in the Stribeck curve, adapted from [6].

When $\lambda < 0.5$ boundary lubrication predominates, resulting in a high CoF. When $0.5 < \lambda < 3$, the lubrication transitions through a mixed boundary region. For values of λ exceeding 3, the lubrication regime is considered to be fully hydrodynamic [4]. However, different researchers propose alternative transition values, such as 1 and 4 [6]. The various lubrication regimes and their corresponding CoF can be graphically visualized against the Hersey number, which is a function of speed, viscosity and load. This graphical representation is commonly referred to as the Stribeck curve.

2.2.1 Boundary lubrication

Boundary lubrication is a lubrication regime where the load is fully carried by asperity contact, representing the real contact area between the work roll and the strip. Despite the real contact area carrying the load, lubrication in this regime still affords some protection to the surfaces of the work roll and the strip. Lubricant could be located in the valleys, but will not contribute to carrying the load, see Figure 9. In this scenario, the surfaces experience increased friction and wear, making it crucial to understand the mechanisms that play a role. Ploughing and boundary shear are two key aspects in boundary lubrication that occur within the interactions between surfaces.

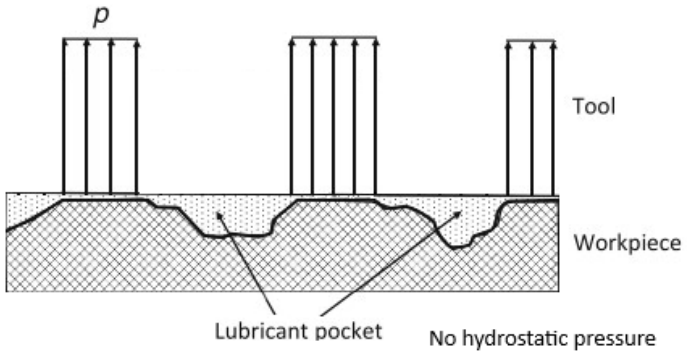

Figure 9: Load division with the boundary lubrication regime between two surfaces, adapted from [6].

Ploughing
Ploughing is a mechanical process at microscale when two surfaces slide against each other. The asperity of one surface penetrates through the opposing surface creating grooves and contributes to surface damage.

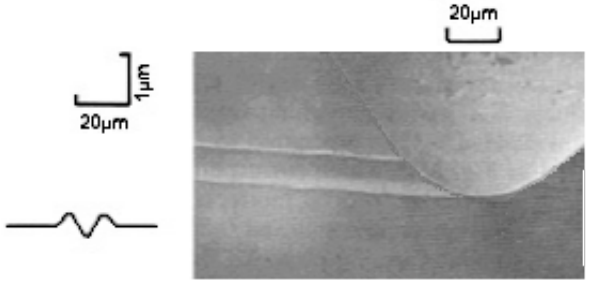

Figure 10: Illustration of ploughing at micro scale, adapted from [27].

Boundary shear
Boundary shear is the tendency of the two different surfaces sticking together. As surfaces come into contact, attractive inter-molecular forces between molecules on the opposing surfaces leads

to resisting movement. The adhesive forces can result in material transfer between the surfaces, also leading to surface damage.

Once the solid contact region is known, boundary friction models are applied to compute the shear stress on top of the asperities. A laboratory method for evaluating the boundary lubrication of cold rolling oil has been investigated by Zang [28]. Wilson [29] created a friction model, but as noted by Tabary [30] it is still unclear whether the boundary shear or the ploughing component is dominant. However Mekicha [4] claims that ploughing is the dominant deformation phenomena that occurs in the cold rolling process.

2.2.2 Mixed lubrication

Within the mixed lubrication regime, the overall normal load is carried by both the asperity contacts and the lubricant. A schematic overview of the load division between the workpiece and tool of a mixed lubrication regime is shown in Figure 11. The relevant friction mechanisms that play a role in the lubricated contact along the roll bite are boundary shear, ploughing and viscous shear [31]. The first two friction mechanisms are active within the asperity contact while viscous shear is active in the lubricant.

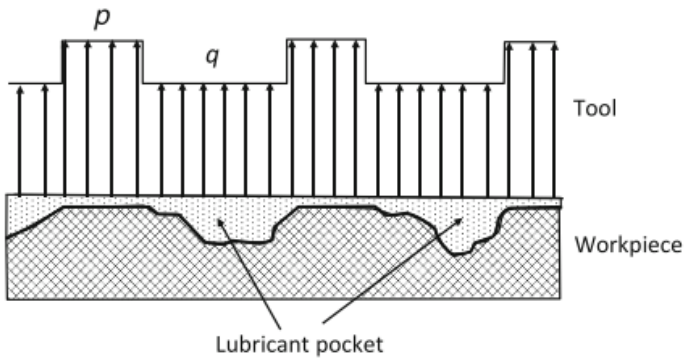

Figure 11: Load division with the mixed lubrication regime between two surfaces, adapted from [6].

Marsault [14] developed a mixed lubrication model for the cold rolling process. This software model includes elasto-plastic strip deformations, elastic roll deformations (FEM), lubricant flow and asperity flattening. Several researchers such as Boman, Stephany and Carretta have worked, implemented or improved the mixed lubrication model [32, 33, 34]. However the current state of art of this model appears to be the work of Boemer [8], who divided the roll bite into different zones to integrate the equation explicitly from zone to zone.

Within the contact of the cold rolling process the lubricant film transits from a mix of mainly hydrodynamic with boundary to mainly boundary with hydrostatic, as can be seen in Figure 12. The division can be explained with different fractions; α is the fraction of boundary lubrication region, β is the fraction of hydrodynamic lubrication and γ is the fraction of the hydrostatic lubrication. α and γ increases, while β decreases throughout the contact zone, but the following relation should be satisfied [6] throughout.

$$\alpha + \beta + \gamma = 1 \tag{5}$$

The normal load P is now given by

$$P = \alpha p_b A + \beta p_f A + \gamma q A \tag{6}$$

where p_b, p_f is the pressure at the boundary and hydrodynamic lubrication respectively, q the pressure at hydrostatic lubrication and A the full contact area of the roll bite. The frictional force can be determined by

$$F_{fric} = \alpha \tau_b A + (1 - \alpha)\, \tau_f A \tag{7}$$

Where τ_b, τ_f the shear stresses of the boundary and hydrodynamic lubrication respectively. Multiple researchers claim that the contribution of shear stress is negligible ($\tau_b >> \tau_f$) and therefore lots of mixed lubrication models are based on the shear stress of the asperity contact only as shown in the following equation. [6] However studies have shown that the viscous shear in hydrodynamic lubrication can not be neglected. Jacobs [13] presented that the viscous shear in the cold rolling process contributes substantially to the total CoF. The shear stresses in the mixed lubrication model can therefore be calculated by the following equation.

$$\tau_{mix.tot} = \alpha \tau_b + (1 - \alpha)\, \tau_f \tag{8}$$

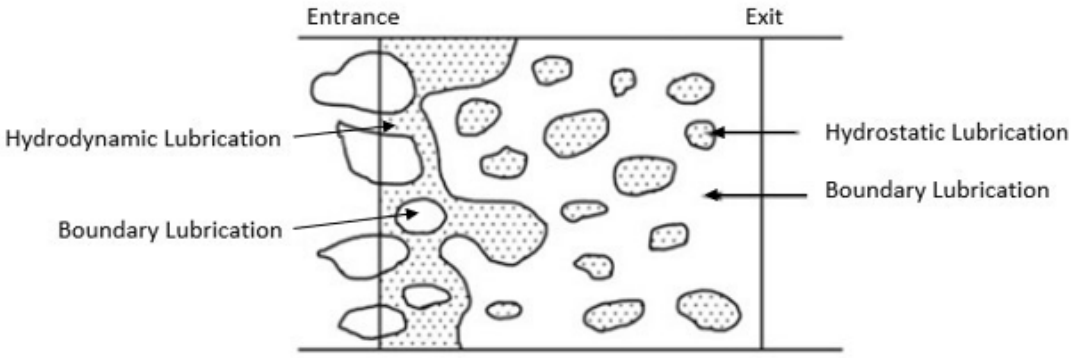

Figure 12: Schematic overview of the mixed lubrication in the roll bite, adapted from [6].

2.2.3 Hydrodynamic (Full film) lubrication

The full film lubrication is a condition where the film thickness is sufficient to completely separate the work roll from the work piece. In this regime, the load is entirely carried by the lubricant and the film layer increases with higher viscosity and rolling speed. To achieve a full film lubrication, a proper selection of lubricant and operating conditions must be satisfied. A fully hydrodynamic model for the cold rolling process is created by Lugt [35].

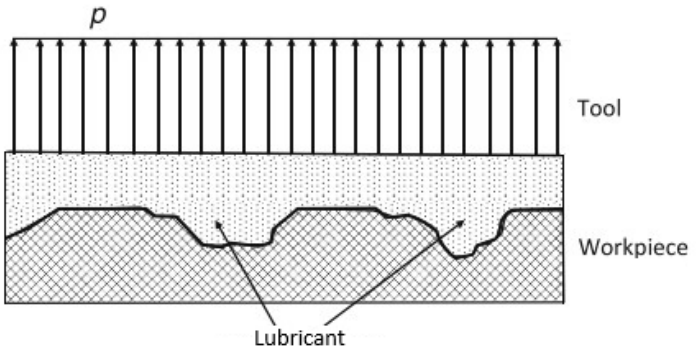

Figure 13: Load division with the hydrodynamic lubrication regime between two surfaces, adapted from [6].

Non-conformal contacts can be categorized into four distinct full film lubrication regimes. They are categorized by elastic deformation of the solids and the impact of pressure on the viscosity. Johnson [36] identified the following four regimes:

Isoviscous-Rigid (IR)
In this regime the shape of the solids surface remains unchanged, because the elastic deformation of the material can be neglected and the material is considered as rigid. The viscosity of the lubricant is unaffected by the applied pressure of the solid bodies. This scenario is encountered when machines operate with very low loads.

Piezoviscous-Rigid (PR)
The pressure that is applied on the lubrication film is so high that the viscosity of the lubricant increases, but does not reach a magnitude to alter the shape of the solid bodies. This regime occurs when liquids have a high sensitivity to pressure.

Isoviscous-Elastic (PE)
This regime is denoted by solids that show elastic deformation and therefore alter the shape of the contact zone. However the lubricants viscosity is independent of pressure and occurs when machine components show elastic behavior and the lubricant viscosity is insensitive to pressure.

Piezoviscous-Elastic (PE) or EHL
A thin lubrication film between rolling or sliding solids that are non-conformal is called the elasto-hydrodynamic lubrication. In this regime, the influence of high pressure both effects the shape of the bodies and the viscosity. It is prevalent in systems such as rolling element bearings and gears lubricated by viscous organic liquids. Pressure dependency of the viscosity and non-Newtonian lubricant behavior are important factors in EHL contacts. [37]

2.3 Elasto-Hydrodynamic Lubrication

The rheological behavior of a lubricant can be observed within an elasto-hydrodynamic lubrication (EHL) contact. Large amount of studies and experiments have been done on EHL theory and the knowledge on this topic increased. The hydrodynamic lubrication of conformal and non-conformal surfaces has been successfully studied by the Reynolds equation (Equation 3) and around 1939 Ertel [38] included the elastic deformation of the contacting solids and the pressure dependent viscosity. The model of Ertel shows thicker film thickness than previous hydrodynamic theory and models [39]. Moes [40] and Grubin [41] also studied the EHL film thickness and came up with equations to determine the EHL film thickness. An iterative method for the EHL film thickness in line contacts is developed by Dowson and Higginson in 1959 [42] and is experimentally verified by Crook [43] and Gohar and Cameron [44]. EHL researchers have extended their studies to develop models describing mixed EHL. The mixed EHL is a lubrication regime where parts of the surface asperities come into direct contact. Such a scenario can take place during the start up of a normal EHL operation, where the contact starts off as dry Hertzian contact and changes into a full film lubricated contact as the velocity increases. Zhao et al. [45] provided research of smooth surfaces in the mixed EHL contact and expressed the transition of boundary to mixed to full film lubrication.

Lots of models use approximations, for example with the pressure distribution. A typical pressure distribution of an EHL contact is shown in Figure 14. The inlet zone shows a build up of pressure and a local maximum is shown around the center of the contact. However the highest peak of pressure is near the exit, which is known as the pressure spike. After the pressure spike the pressure decreases rapid at the contact exit.

Within models, this pressure distribution if often replaced by the Hertz contact pressure which has a parabolic shape for a line contact and an ellipsoidal shape for a point contact, shown

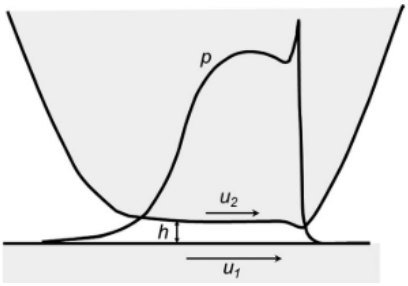

Figure 14: Pressure distribution in an Elasto-Hydrodynamic Lubrication contact, adapted from [46].

in Figure 15 respectively. Where r_a is the half-contact width or contact radius and p_{max} the maximum contact pressure.

(a) Line contact

(b) Point contact

Figure 15: Hertz pressure distribution, adapted from [46].

2.4 Viscous shear

In a lubricated contact, such as an EHL contact, two bodies are moving at different speeds. Therefore, the lubricant experiences internal friction caused by layers of fluid moving at different velocities, known as viscous shear. Figure 16 shows a visual image of a lubricant that experiences viscous shear by two bodies moving at different speeds.

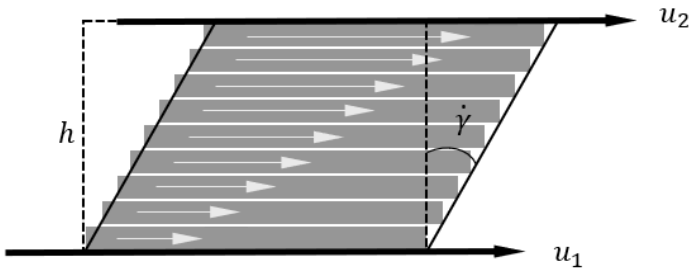

Figure 16: Lubricant represented by multiple layers bounded by two moving solids.

The rate at which the two boundary solids move relative to each other is defined as the shear rate. The shear rate, denoted by $\dot{\gamma}$, can be calculated by the following equation:

$$\dot{\gamma} = \frac{u_s}{h} \tag{9}$$

where h is the film thickness of the fluid layer and u_s the sliding speed, which is the absolute difference in speed between the two bodies $u_s = |u_1 - u_2|$.

Viscous shear is a function of the shear rate and the viscosity of the fluid. Increasing the shear rate or viscosity will increase viscous shear. The influence of viscosity on viscous shear is explained in the following subsection.

2.4.1 Viscosity of a fluid

Viscosity is a measure of resistance to flow and is highly dependent on pressure. A high viscosity of a fluid indicates more resistance to flow, which leads to higher viscous shear stress. Barus [47] derived an equation for the viscosity dependency with pressure.

$$\eta(p) = \eta_a \exp(\alpha p) \tag{10}$$

where η_a is the viscosity at ambient pressure and reference temperature and α the viscosity-pressure coefficient.

Murch and Wilson [48] studied viscous shear and used an exponential viscosity-temperature model, which is an extension on the Barus equation and incorporates the temperature dependency.

$$\eta(p,T) = \eta_s \exp(\alpha p - \beta [T - T_s]) \tag{11}$$

where η_s is the base viscosity at base temperature T_s and ambient pressure p_s and β is the viscosity-temperature coefficient. However these exponential equations overestimate the viscosity at higher pressures and Roelands [49] introduced a more accurate viscosity equation for these higher pressures.

$$\eta(p,T) = \eta_s \exp\left[\left(\ln\frac{\eta_s}{\eta_0} + 9.67\right)\left(\left[\frac{p-p_0}{p_s-p_0}\right]^z \left[\frac{T_s-T_0}{T-T_0}\right]^{s_0} - 1\right)\right] \tag{12}$$

where η_0, p_0 and T_0 are universal constants, z the viscosity-pressure parameter, T the temperature and s_0 is the temperature index of the viscosity [40].

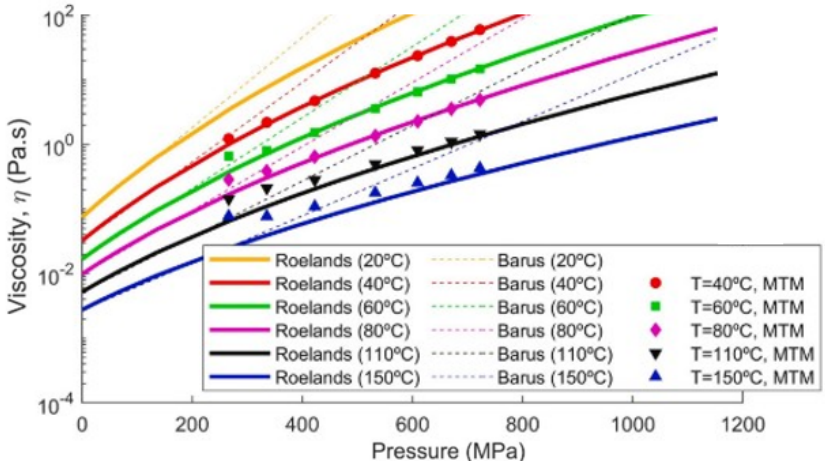

Figure 17: Viscosity resulting from ball-on-disc experiments, fitted by Roelands and Barus. Adapted from [13].

Jacobs [13] and Bair [37, 50] both showed by experiments that the viscosity is described more accurately by the Roelands equation. The difference in viscosity between Barus and Roelands is shown in Figure 17, where both equations are plotted for a lubrication oil tested with a ball on disk experiment.

2.4.2 Viscous shear models

Viscous shear is an important aspect in the rheological behavior of fluids, which can be either Newtonian or non-Newtonian. A fluid is considered Newtonian when the relation between shear rate and shear stress is linear. Water is for example a Newtonian fluid and the viscosity remains unchanged when exposed to shear.

$$\tau = \eta(p,T)\,\dot{\gamma} \tag{13}$$

However most fluids exhibit non-Newtonian behavior which can be further classified as shear thinning, where the viscosity decreases with increasing shear rate or shear thickening, where the viscosity increases with increasing shear rate.

Researchers such as Eyring [51] and Carreau & Yasuda [52] have studied shear thinning and developed non-linear equations for the shear stress, which are shown respectively below.

$$\tau = \tau_e\ \sinh^{-1}\left(\frac{\eta(p,T)\,\dot{\gamma}}{\tau_e}\right) \tag{14}$$

$$\tau = \eta(p,T)\,\frac{\dot{\gamma}}{\left[1+\left(\frac{\eta(p,T)\,\dot{\gamma}}{\tau_0}\right)^a\right]^{\frac{1-n}{a}}} \tag{15}$$

Where n and a are constants and τ_e,τ_0 is the shear stress corresponding to the value at which shear thinning starts to become significant.

Jacobs [13] studied and experimented the basics of friction and viscous shear of fluids in EHL by using a ball-on-disc experiment. By running experiments with the same oil, but under different temperatures and pressures, he measured the friction force as function of the SRR (Slide-to-Roll Ratio). The relation between the friction force and the SRR can be captured in a traction curve. The SRR can be calculated with the entrainment speed U, which is the mean of both rolling speeds $U = (u_1 + u_2)/2$ and the sliding speed u_s.

$$SRR = \frac{2|u_1 - u_2|}{(u_1 + u_2)} \cdot 100\% \tag{16}$$

Figure 18 shows the results of the ball-on-disc experiment conducted with a normal load of $F_n = 20\ N$ and a temperature of $T = 40\ °C$. Jacobs showed that an elevated temperature causes a lower CoF, due to the fact of a decrease in viscosity. Conversely, an increase in pressure leads to higher viscosity, consequently resulting in an increased CoF. In instances of pure rolling (SRR=0), where both bodies move at identical velocities, the CoF is approximately zero. However, with the presence of sliding (SRR>0), an increase in CoF is observed and eventually levels out. These traction curves can be converted into mean shear stress versus shear rate curves, as illustrated in (Figure 18b, which provide a description of the rheology of the EHL film. The mean shear stress can be calculated by the friction force divided by the Hertz contact area of the two surfaces.

$$\overline{\tau} = \frac{F_{fric}}{A_{Hertz}} \tag{17}$$

From Figure 18b it can be seen that the experimental data behaves Newtonian for low shear rates ($\dot{\gamma} < 2 \times 10^5\ s^{-1}$), but deviates from the Newtonian model when exceeding aforementioned shear rate due to shear thinning. Therefore the Eyring model shows a better fit for the experimental data.

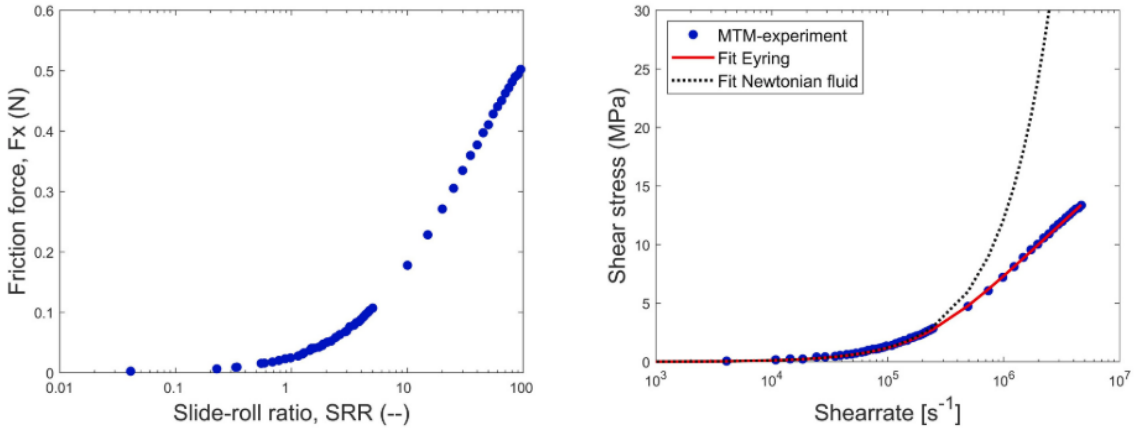

(a) Traction curve

(b) Shear stress versus shear rate curve

Figure 18: Experimental data results of ball-on-disc experiment performed with a normal load of $F_n = 20\ N$ and a temperature of $T = 40\ °C$, adapted from [13].

2.5 Viscous shear heating in EHL

Viscous shear heating, due to sliding friction, occurs from frictional forces between fluid layers moving at different velocities. As fluids experience shear stress, characterized by the relative motion between adjacent layers, internal friction generates thermal energy, contributing to an increase in temperature within the fluid. Under elevated shear stresses and shear rates the aspect of viscous shear heating becomes relevant and the temperature of the lubricant within the contact begins to rise. This temperature increase causes the traction curves to level out and, in certain instances it starts to decrease. There are three different heating effects which can result in a temperature rise in the EHL film:
i) Shear heating caused by the sliding component of friction
ii) Shear heating caused by the rolling component of friction
iii) Compressive heating caused by compression due to for example a pressure rise.

2.5.1 Viscous shear heating at the contact zone

The second heating effect (ii) is considered negligible in the contact region as shown by Spikes [46]. Cheng [53], Habchi [54] and Reddyhoff et al. [55] studied the third case and found out that the heat generation from compression is very small in comparison to that caused by shearing under sliding conditions. Habchi found that compressive heating is of the same order as shear heating when pure rolling is considered. However, under rolling–sliding conditions, as soon as the slightest sliding occurs, heat generation within these contacts is governed by shear heating. Therefore shear heating caused by sliding friction is the main aspect of the temperature rise in the EHL contact. This heating within the contact results in a reduction of the friction coefficient.

Grieve and Spikes [56] experimented with temperature mapping and focused on a technique for obtaining detailed maps of shear stress based on measured temperature rise of EHL contacts. It was found that almost all of the energy dissipation and thus temperature rise within a rolling-sliding contact results directly from the shear of the lubricant film. Temperature rise and shear stress maps in a pure EHL sliding contact are shown in Figure 19.

The left side of both maps in Figure 19 represents the inlet of the contact and the right represents the exit. The temperature at the exit is higher than the bulk temperature due to convection in the plane of the film.

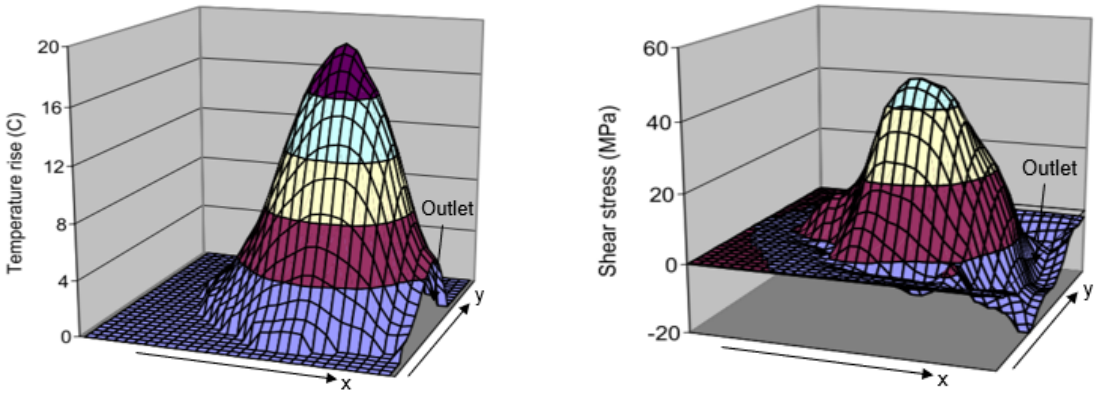

(a) Temperature rise

(b) Shear stress

Figure 19: Map of EHL contact at $SRR = 100\,\%$, $U = 1.6\,m/s$, $\overline{p} = 0.97\,GPa$, $T_s = 50\,°C$. Adapted from [56].

2.5.2 Viscous shear heating at the inlet zone

Goksem [57] investigated the effect of viscous shear heating in the inlet region and introduced a new equation for both fully flooded film thickness and rolling traction. Experimental results indicate that under pure rolling conditions, a maximum traction value occurs at a relatively low speed, but the film thickness at this speed is not significantly reduced from the value predicted by isothermal theories. While compressive heating has shown to play a minor role in the heat generation, the viscous shear heating effect is found to reduce the film thickness by a considerable amount at high speeds.
Murch and Wilson [48] also concluded that inlet shear heating effects can substantially reduce the film thickness from the isothermal value. Due to the temperature rise within the lubricant the viscosity drops which leads to a reduction in the film thickness. Murch and Wilson used a thermal Reynolds equation derived by Wilson and Mahdavian [58], instead of the conventional Reynolds equation. This thermal equation incorporates the effect of viscosity variation across the lubricant film due to viscous heating.

2.6 Research gap

Models for friction in the cold rolling process have been around for more then a century. The significance of lubrication and its impact on the CoF is highlighted. Several researchers have studied the film thickness in the cold rolling process which is necessary to determine the active lubrication regime. Multiple lubrication regimes can occur, such as boundary, mixed or hydrodynamic lubrication, however most mixed lubrication models neglect viscous shear. It is addressed that this phenomena can not be neglected.
When delving into lubrication oils, it is stated that viscosity is highly dependent on pressure and temperature. The role of viscous shear in lubricants in EHL, including its importance in rheological behavior, is mentioned. The literature study includes experiments on friction and viscous shear, revealing temperature and pressure effects on the coefficient of friction and therefore the mean shear stress. The literature study is concluded by discussing different heating effects, which contributes to a temperature rise in the EHL film.
Azushima mentioned the importance of thermal effects within the cold rolling process for the inlet film thickness. However little research has been done on viscous shear heating in the cold rolling process. Therefore this study focuses on the possibility of viscous shear heating within the cold rolling process.

2.7 Problem definition

This section uses the missing aspects in the literature stated in subsection 2.6 to shape the research question.

2.7.1 Research question

The following main research question of this thesis is established:

"*Under which conditions can viscous shear heating be expected within a cold rolling tandem mill?*"

The hypothesis is that viscous shear heating will occur in the cold rolling process due to relative high sliding speeds and low film thickness. The viscosity of the lubricant also increases due to increasing pressure, which increases viscous shear.

To answer the main research questions, several sub-questions have been formulated.

1. What is a proper methodology to test the relevant rheological parameters?
2. What are the parameters/factors that influence the occurrence of viscous shear heating in EHL?
3. What are the rheological parameters of the cold rolling lubrication oil, used at Tata Steel?
4. How can the occurrence of viscous shear heating in the lubricant be predicted in EHL?
5. How can the data of the EHL contact experiments be correlated to the cold rolling process?

2.7.2 Scope of the research

This work provides an analysis of lubrication and friction phenomena in the cold rolling process and in particular the detailed effects of viscous shear heating. The study is limited by looking into one lubrication oil and dealing with stable steady-state rolling models. External factors such as mill vibrations and surface quality are not within the scope of this research.

While the cold mill typically operates within the mixed lubrication regime, this research focuses on conducting experiments under conditions that simulate the elastohydrodynamic lubrication regime. By investigating the lubricant behavior in the EHL regime, the aim is to enhance understanding of how lubricants behave under higher pressures, temperatures and velocities encountered during cold rolling.

3 Methodology

The current chapter delves into the methodology used for this research. It explains the experimental setup, materials used, testing range and the computational approach. Therefore it addresses the first sub-question: "*What is a proper methodology to test the relevant rheological parameters?*"

This chapter is organized in the following way:

Section 3.1 approaches various methods for evaluating the rheological behavior of a fluid in an EHL contact. Three different methods will be compared and the most suitable method for this thesis will be chosen and elaborated in more detail.

Section 3.2 outlines the testing procedure such as testing specimens, calibrations and the testing range. Additionally an error analysis shows the reliability of the testing methodology.

Section 3.3 explains how the experimental results can be processed to usable data for answering sub-questions 3 and 4. The computational approach used to obtain the rheological parameters are explained with a flow diagram.

Section 3.4 explains how to obtain a model that establishes the conditions under which viscous shear heating is anticipated to occur.

Finally, section 3.5 explains how viscous shear heating can be predicted in the cold rolling process.

3.1 Experimental methods for rheological parameters

There are several ways to measure rheological parameters of a fluid. The three most common methods; conventional rheometry, steady state rheometry and impact rheometry will be discussed. After further elaboration of the three methods, one method is suggested for the experiments of this thesis.

Conventional rheometry
A conventional set up is arranged from a rotating cylinder in a cup. The cylinder is attached to a shaft which contains a torque sensor that tracks the shear stress. The cylinder can be controlled at different rotating speeds, but the cup stays stationary. Different sliding speeds can be obtained in this way, but pure rolling conditions can not be achieved in this method. The film thickness is equivalent to the gap width between the cylinder and the cup. The shear rate can in this case easily be controlled with the stationary film thickness and fluctuating sliding speeds. A fluids viscosity can be measured under different conditions such as temperature, sliding speed and film thickness. However the pressure can not be increased and thus only experiments at atmospheric pressure can be conducted.

Steady state rheometry
One of the most common approaches to study the EHL rheology of a fluid is to set up a steady state EHL film, which can be achieved by a ball on disk experiment. The Mini Traction Machine, abbreviated by MTM, is such a ball on disk experiment and measures friction over a range of slide to roll ratios. The ball is pressed against the flat surface of the disc and is submerged in lubricant within the test chamber. The ball shaft is tilted so that its axis intercepts the centre of rotation of the upper surface of the disc to minimise spin in the contact. The disc and ball are driven by separate motors to enable any desired combination of entrainment speed and sliding speed. This enables friction to be studied as a function of the SRR at a fixed entrainment speed and thus a presumably fixed film thickness. This experimentation would not be possible if one

specimen remained stationary with zero speed. Friction is measured by a load cell attached to the ball shaft housing. A schematic overview of the MTM is shown in Figure 20.

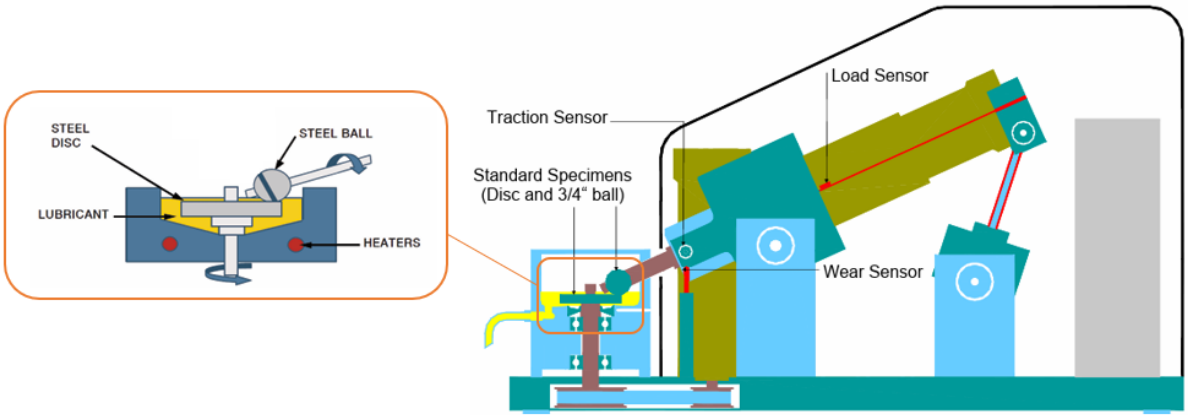

Figure 20: Schematic overview MTM, adapted from [59].

Impact rheometry
Impact rheometry is based on a a thin film of fluid between the surfaces of a pair of solid bodies. One of the bodies is subjected to a sudden shock wave, typically by the impact of a projectile. The displacement of the opposing body is measured to determine the behavior of the fluid to sudden compression. By angling the fluid layer, it is possible to measure both the compressive and shear response under transient imposition of very high pressure and shear wave.

Both the conventional and impact rheometry have limitations with respect to mimicking EHL conditions. With conventional rheometry only atmospheric pressure can be exerted, while with impact rheometry it is easy to reach very high pressures up to $p = 3\ GPa$ and higher. It is, however, more difficult to obtain accurate rheological data at pressures beneath 1 GPa due to difficulty of measuring the really small displacement of the opposing body. The major advantage of the steady state method such as the ball on disc experiment is that it simulates a realistic EHL contact. The main disadvantage is that the measurements are based on average measurements such as the pressure over the whole contact. However pressure and therefore the viscosity varies over the contact area. The second disadvantage is that the film thickness and viscosity can not be measured directly and have to be obtained otherwise. Despite these two disadvantages the steady state ball on disc method will be used for this research to obtain the rheoligical parameters of the lubrication oil. The wide measuring range and the good simulation of an EHL contact are important aspects and therefore this method is preferable.

3.2 Testing procedure on the MTM

The MTM will be used to establish the rheological parameters of the lubrication oil under EHL conditions. This is done to make sure that the measured CoF is purely based on the fluid behavior and not the asperity contact. The lubrication oil that is investigated in this thesis is partly a synthetic oil mainly based on Esters.

To ensure that only viscous effects of the lubricant will be investigated, the Deborah number (De) will be calculated. The Deborah number serves as a criterion for characterizing the behavior of a fluid with respect to elastic and viscous properties. $De > 1$ signifies that the fluid shows mainly elastic behavior, while $De < 1$ implies that the fluid has mainly viscous properties. When $De \approx 1$, the fluid shows both elastic and viscous behavior and can be determined as visco-elastic. The Deborah number can be calculated with the following equation.

$$De = \frac{\eta \left(u_{ball} + u_{disc}\right)}{2\, G\, r_a} \tag{18}$$

where G represents the shear modulus of the lubricant and r_a the contact radius determined by Hertz. The results show that the Deborah number consistently remains far below the value of 1, hence the lubricant can be assumed to be viscous and therefore elastic effects can be neglected. [60]

3.2.1 Specimens

The specimens utilized within the MTM are a highly polished ball and disc made of 52100 AISI steel, with an elasticity modulus of $E = 207\ GPa$ and a Poisson's ratio of $\mu = 0.29$. They are mounted to shafts which are located within the MTM to secure them in place, see the close up in Figure 20. There are two different sizes of balls, the big one is the $3/4$" equivalent to a radius of $r_{ball} = 9,525\ mm$ and the small ball is $1/2$", which corresponds to a radius of $r_{ball} = 6.35\ mm$. They can be used interchangeably to achieve the desired pressure in combination with the corresponding normal load. The $3/4$" ball will be used for experiments up to its maximum mean pressure of $\overline{p} = 846\ MPa$ and the higher pressures will be obtained with the $1/2$" ball. An overview of the applied normal forces for each ball with their corresponding normal loads can be found in subsection 3.2.4.

Within the experiments the goal is to measure and observe the lubricant behavior. Therefore it is necessary to stay within the full film regime so asperity contact will be avoided. To achieve full film lubrication, the specimens are supplied with a smooth surface roughness finish of $R_a \leq 0.02\ \mu m$. An image of the MTM specimens is shown in Figure 21.

Figure 21: Specimens for the MTM machine. Left the ball and on the right the disk, obtained from [59].

3.2.2 Calibration

Calibration of the MTM will be conducted prior to the first round of testing with the $3/4$" ball. The calibration for the loading and traction system will be performed, by hanging specific weights to the shaft of the ball. A load sensor will be calibrated to the corresponding force of the weight. Additionally, prior to the second round of testing with the $1/2$" ball, the aforementioned calibrations will be carried out again to maintain the accuracy of the testing results.

3.2.3 Error estimation

An error estimation of the MTM is conducted to ensure the accuracy of the test results. A series of traction experiments is performed under fixed conditions of a temperature $T = 30\ °C$, a normal load of $F_n = 40\ N$ and entrainment speed of $U = 1\ m/s$. The traction experiments are executed in ten repetitions in both forward and backward direction of the SRR. Each run

thus measures two points which are presented in one data point representing the average of the traction coefficient obtained from one forward-backward cycle. These experimental data points, along with their mean value are shown in Figure 22a. A close up of one set of ten data points is visualized in Figure 22b.

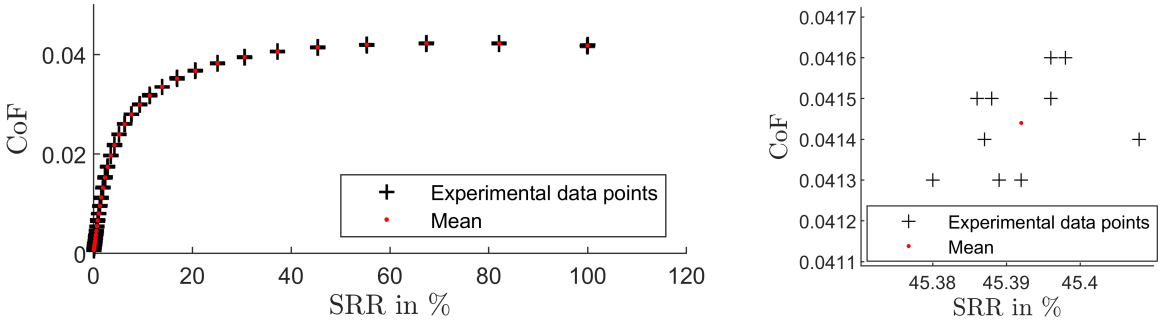

(a) Full Traction curve

(b) Close up

Figure 22: Traction experimental data points at $T = 30\ °C$, $F_n = 40\ N$ and $U = 1\ m/s$ measured by the MTM, where (a) shows the full traction curve and (b) a close up at a SRR of $45,39\ \%$.

The standard deviation of the ten data points relative to their mean in both the SRR and CoF is plotted in Figure 23 with respect to the SRR. This plot shows, at very low SRR ranging from $0\% < SRR < 1\%$, for both the SRR and the CoF quite a big error, 29.9% and 31.5% respectively. However the error reduces fast and converges to an error of 0.05% for the SRR and 0.4% for the CoF, which is acceptable for experimental tolerances. The elevated error observed in the low SRR can be neglected for this thesis considering that thermal effects are anticipated to occur at high shear rates, thus higher SRRs.

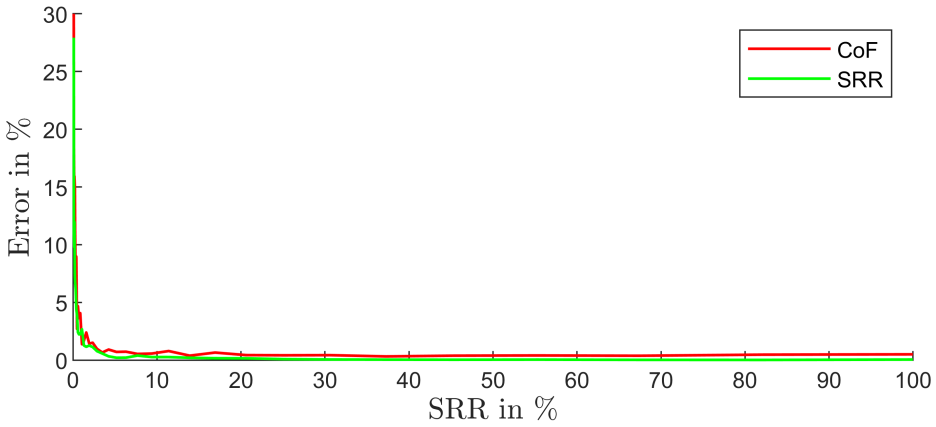

Figure 23: Error estimation of the MTM of the CoF and SRR in percentage over a range of SRRs.

3.2.4 Testing range

The testing range must be sufficiently wide to obtain accurate rheological parameters, while also being within the operational range of the cold rolling process. Testing parameters that can be changed are SRR, temperature, normal load and entrainment speed. The testing range of aforementioned parameters are elaborated below. To ensure smooth specimen surfaces throughout testing and to maintain unchanged surface roughness, the order of testing is arranged such that any occurrence of mixed lubrication occurs at the end of the testing procedure. All combinations possible will be tested with the experiments on the MTM.

Slide to Roll Ratio
The SRR is chosen within the range of $0.1\% \leq SRR \leq 150\%$. This range includes almost pure rolling conditions which occurs around the neutral point within the roll bite and allows the observation of very high shear rates which could be encountered during cold rolling. A lower limit of 0.1% SRR is selected due to the challenges and big error associated with measuring at extremely low SRR values. The upper limit of 150% SRR is selected, because higher SRRs will exceed the limitation of the MTM with the entrainment speed of $U = 2\ m/s$. It is expected that viscous shear heating becomes significant at high SRR. The 35 points interval on a logarithmic scale ensures linear spread out points on the shear stress - shear rate curve.

$SRR = [0.10, 0.12, 0.15, 0.19, 0.24, 0.29, 0.36, 0.41, 0.56, 0.69, 0.86, 1.07, 1.32, 1.64, 2.03, 2.52, 3.12, 3.87, 4.80, 5.96, 7.38, 9.16, 11.35, 14.08, 17.46, 21.65, 26.84, 33.28, 41.27, 51.17, 63.45, 78.68, 97.56, 120.97, 150.00]$

Temperature
The temperature range is chosen from $T = 40\ °C$ to $T = 130\ °C$. At Tata Steel the emulsion is applied at a temperature that varies between $T = 40 - 60\ °C$. The temperature of the oil in the roll bite will gradually increase due to plastic deformation and frictional heating generated during the cold rolling process. The temperature intervals are chosen at 10 °C for lower temperatures, where viscous shear heating is expected to be more present and at the higher temperatures an interval of 20 °C is taken.

$T = [40, 50, 60, 70, 80, 90, 110, 130]\ °C$

Normal load
From the Roelands equation it is known that a higher viscosity gradient is present in the low pressure range. Thus to capture the full lubricant behavior under pressure, the normal load is selected from $F_n = 10\ N$ to $F_n = 75\ N$ for the $3/4$" ball with intervals of $10\ N$ for lower loads and $15\ N$ for the higher loads. The associated mean pressures are calculated by the Hertz pressure distribution theory. The $1/2$" ball is used to achieve even higher pressures and therefore the normal load is set at the maximum of $F_n = 75\ N$ to obtain a pressure of $\overline{p} \approx 1,1\ GPa$.

Table 1: Testing conditions for the 3/4 inch ball and 1/2 inch ball.

$3/4$" ball	$1/2$" ball
$F_n = [10, 20, 30, 45, 60, 75]\ N$	$F_n = [45, 60, 75]\ N$
$\overline{p} = [432, 544, 623, 713, 785, 846]\ MPa$	$\overline{p} = [939, 1029, 1108]\ MPa$

Entrainment speed
The entrainment speed is chosen from $U = 1\ m/s$ to $U = 2\ m/s$ with an interval of $0.5\ m/s$. Rolling speeds at a cold rolling process can easily exceed $2\ m/s$, but unfortunately testing at higher entrainment speeds is not possible due to speed limitations of the ball or disk of the MTM.

$U = [1, 1.5, 2]\ m/s$

3.3 Processing experimental data to determine rheological parameters

The MTM gives a text file as output that contains all measured and controlled values. These raw data values are loaded into the data processor Matlab. Measured values, such as the friction force and sliding speed are categorized and saved under suitable names. From this point all computations can be carried out with the measured values from the MTM. Traction curves can be shown immediately by plotting the CoF against the SRR. However the shear stress - shear rate curves can not be plotted without the use of a model. The average shear stress can be calculated with the raw data from the text files, but the film thickness is needed for the calculation of the shear rate. The MTM does not measure the film thickness, thus a model will be used to estimate the film thickness. The computational approach used in Matlab to determine the rheological parameters will be elaborated in this section.

First of all the experimental mean shear stress can be calculated by the following equation:

$$\overline{\tau} = \frac{F_{fric}}{\pi r_a^2} \tag{19}$$

where F_{fric} is the measured friction force and r_a the contact radius calculated by Hertz theory for a point contact shown in the equation below.

$$r_a = \left(\frac{3\, F_N\, r_{ball}}{2\, E'} \right)^{1/3} \tag{20}$$

The experimental shear stress will be compared with the theoretical shear stress calculated with the theory of Eyring (Equation 14). Eyring is chosen above the Carreau-Yasuda theory (Equation 15), because it typically fits the experimental EHL friction data very well and has been the preferred choice of EHL researchers since early on [46]. The viscosity, shear rate and the Eyring stress are needed to calculate the theoretical shear stress by the Eyring equation. The shear rate can be calculated by Equation 9, but as stated before the film thickness is still undetermined.

To compute the film thickness using the theory of Moes, elaborated in subsection 3.3.3, certain prior calculations have to be performed to obtain necessary parameters. One of these parameters is the pressure-viscosity coefficient, which describes the behavior of the lubricant under varying pressures. The computations for the pressure viscosity coefficient is further elaborated in subsection 3.3.2.

Similarly, when computing the viscosity using the equation of Roelands, an important parameter is still unknown. This parameter, denoted by z is another parameter describing the pressure viscosity relation. By fitting experimental results to the theoretical model, the z value can be determined.

The last unknown parameter needed to calculate the theoretical shear stress is the Eyring stress τ_e. The Eyring stress is the stress where shear thinning becomes relevant. Given that both the z value and the Eyring stress are initially unknown, the computational approach starts with an initial guess for these parameters. Based on this initial guess the theoretical shear can be calculated. If the error between the theoretical and experimental shear stress exceeds acceptable limits, the calculations will be repeated with a different guess for the z value and Eyring stress. This iterative process is repeated until the error between theoretical and experimental shear stress is minimum and convergence is reached. The flow diagram in Figure 24 visually explains the iterative computational approach, where each loop represents a cycle of taking a new guess for

the z value and the Eyring stress. The computations for the necessary parameters are elaborated in the following subsections.

3.3.1 Computation of the viscosity by Roelands

The viscosity is determined using Roelands (Equation 12) shown in section 2.4 and repeated below.

$$\eta(p,T) = \eta_s \exp\left[\left(\ln\frac{\eta_s}{\eta_0} + 9.67\right)\left(\left[\frac{p-p_0}{p_s-p_0}\right]^z \left[\frac{T_s-T_0}{T-T_0}\right]^{s_0} - 1\right)\right]$$

The constants η_0, p_0 and T_0 are known constants and p_s, T_s are values based on the base conditions of the oil. The base temperature of the oil is set at $T_s = 40\,°C$ under atmospheric pressure of $p_s = 101325\,Pa$ and η_s is the viscosity under these ambient conditions. The ambient viscosity and the parameter s_0 are both unknown. By measuring the ambient viscosity for multiple temperatures, the s_0 value can be determined as well by fitting the Roelands equation. Therefore the ambient viscosity will be measured using the Haake RheoStress 6000, which is a conventional rheometry machine that can measure the viscosity of a fluid at different temperatures under atmospheric pressure. The maximum temperature the Haake RheoStress 6000 can reach is $T = 75\,°C$. Therefore the testing range will be $T = 30 - 75\,°C$ with increment steps of $10\,°C$ at the beginning and the last step is $T = 5\,°C$.

The z value is not needed to determine the s_0 coefficient. With $p = p_s$ the pressure division term will become 1, so the power of z will not change outcome of this term. However the z value will be needed later on for determining the viscosity by Roelands and will be obtained as explained in 3.3. Even more precise is the extended Roelands equation, which accounts for a small interdependence of the term related to temperature and the term related to pressure. Therefore this z value can be calculated by the following equation.

$$z = D + C\,\ln\left(\frac{-T_0}{T-T_0}\right) \tag{21}$$

here $T_0 = -135\,°C$ and D, C are constants that have to be fitted with the known z and corresponding T values.

3.3.2 Computation of the pressure viscosity coefficient by Blok

The pressure viscosity coefficient α is a parameter that is needed to determine the film thickness by the theory of Moes. This parameter can be calculated by Equation 22, however this equation is accurate for lower pressures, normally up till pressures of $p = 100\,MPa$ [40].

$$\alpha_a = \left(\ln\frac{\eta_a}{\eta_0} + 9.67\right)\frac{z}{|p_0|} \tag{22}$$

In this equation η_0 and p_0 are known constants and η_a is the viscosity under atmospheric pressure and reference temperature. A more accurate relation to describe the pressure viscosity coefficient for more substantial pressures can be calculated by Blok [61], shown in Equation 23. Because of this reason the pressure viscosity coefficient will be calculated by Blok.

$$\alpha^* = \frac{\alpha_a}{1 + \frac{1-z}{\alpha_a\,|p_0|}} \tag{23}$$

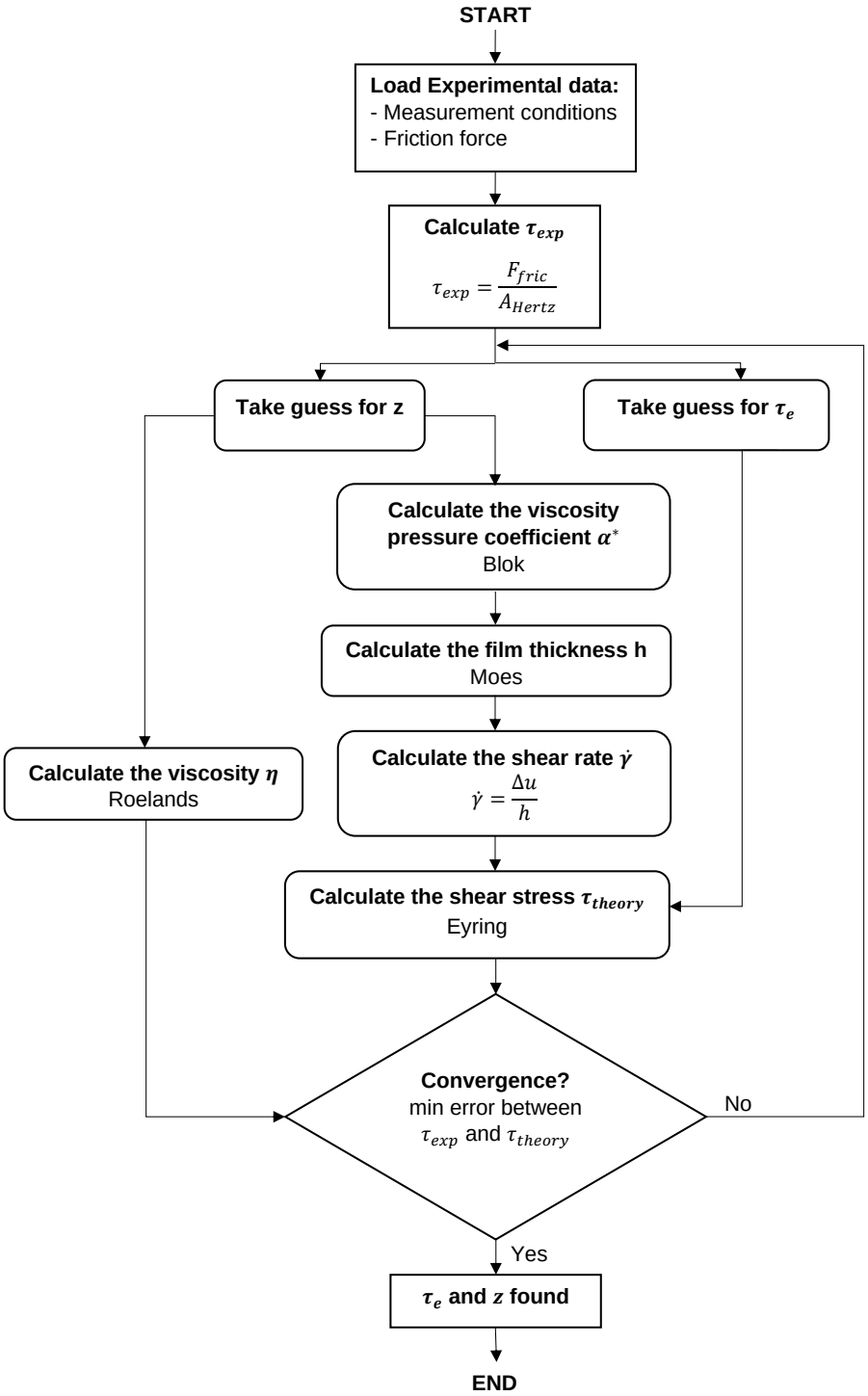

Figure 24: Flow diagram of the computational approach used to determine the z and τ_e values.

3.3.3 Computation of the film thickness by Moes

The central film thickness h in an EHL point contact can be calculated by the formula of Moes [40].

$$h = H\ r_{ball}\ \left(\frac{E'\ r_{ball}}{\eta_a\ U_{sum}}\right)^{-1/2} \tag{24}$$

where E' represents the combined Young's modulus, r_a the radius of the ball specimen, U_{sum} is the sum speed of the ball and disc and H can be determined with

$$H = \left[\left(H_{RI}^{3/2} + \left(H_{EI}^{-4} + 0.1\right)^{-3/8}\right)^{2s/3} + \left(H_{RP}^{-8} + H_{EP}^{-8}\right)^{-s/8}\right]^{1/s} \tag{25}$$

where

$$s = \frac{3}{2}\left[1 + \exp\left(-1.2\frac{H_{EI}}{H_{RI}}\right)\right] \tag{26}$$

and

$$H_{RI} = 145(1.796)^{-15/7}\ N^{-2} \tag{27}$$
$$H_{RP} = 1.29(1.691)^{-2/3}\ L^{2/3} \tag{28}$$
$$H_{EI} = 3.18(1.630)^{-14/25}\ N^{-2/15} \tag{29}$$
$$H_{EP} = 1.48(1.630)^{-7/20}\ N^{-1/12}\ L^{3/4} \tag{30}$$

in which N and L are determined by

$$N = \frac{F_n}{E'\ r_{ball}^2}\left(\frac{E'\ r_{ball}}{\eta_a\ U_{sum}}\right)^{3/4} \tag{31}$$

$$L = \alpha^*\ E'\left(\frac{\eta_a\ U_{sum}}{E'\ r_{ball}}\right)^{1/4} \tag{32}$$

3.4 Finding the starting point for viscous shear heating

As stated before, it is more straightforward to detect the onset of viscous shear heating in the stress strain curve than in the traction curve. The methodology for obtaining the stress strain curves is provided in the previous section. The shear stress based on experimental data is fitted with the theoretical shear stress derived from Eyring theory. A graphical representation is illustrated in Figure 25. The black dots represent the experimental data, while the red line denotes the shear stress calculated by Eyring. The model of Eyring exhibits a consistent linear line on a logarithmic scale for $\tau > \tau_e$. Shear stress based on the experimental data follows this model of Eyring up to a certain point where it starts to deviate negatively from the linear line. This point is indicated with the dashed line and can be computed by setting a tolerance error.

The tolerance error is the maximum stress deviation that the experimental data can have compared to the Eyring model. The precise tolerance error will be determined when the shear

stresses are calculated, because it will depend on the magnitude. It is assumed that the maximum shear stress will not exceed $\bar{\tau} = 50\ MPa$. A tolerance error of approximately $1 - 2\ \%$ of the maximum shear stress will be used. When the tolerance error is chosen too large, the onset of viscous shear heating will be underestimated. A tolerance factor too small, may lead to detecting small measurement errors instead of the onset of viscous shear heating.

The limiting isothermal shear rate $\dot{\gamma}_L$ is the threshold for which Eyring is applicable and corresponds to the point where the divergence in shear stress exceeds the tolerance error. After this threshold viscous shear heating occurs. The starting point of viscous shear heating is preferred to be indicated in terms of shear rate over the shear stress. This is due to the fact that the shear rate is easier to determine within the cold rolling process.

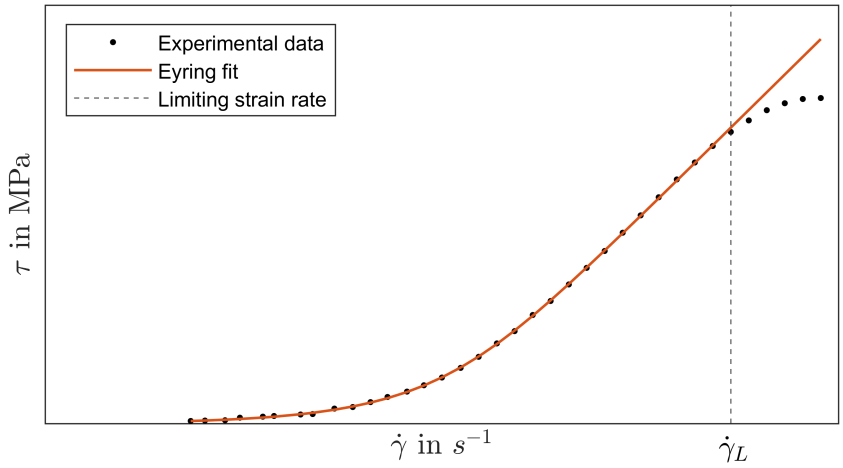

Figure 25: Starting point of viscous shear heating indicated by the dashed line.

The absence of numerical values on the x- and y-axis in Figure 25 is because of the current lack of precise values and magnitudes. The assumption is that limiting isothermal shear rate is approximately in the order of $\dot{\gamma}_L \approx 10^6 - 10^7\ s^{-1}$. The limiting isothermal shear rate $\dot{\gamma}_L$ will be visualized by plotting it against the parameters that influences the onset of viscous shear heating.

3.5 Linking viscous shear heating to the cold rolling process

The geometry of the cold rolling process as shown in Figure 2 will be modelled in Matlab with dimensions that are common for the strips and stands of the cold mills at Tata steel. Within the modelling of the cold rolling process, circular roll flattening is taken into account. Every stand will be modelled focusing on the following three areas: inlet zone, work zone and outlet zone.

First of all an investigation has to take place for the area with the highest likelihood of the occurrence of viscous shear heating in the cold rolling process. After it is stated if viscous shear heating is most likely to occur within the inlet zone, work zone or outlet zone, it can be checked if the cold rolling process is within the range of viscous shear heating.

4 Results

This chapter states the results from every set of experiments along with observations, remarks and statistics. Interpretation and further discussion points can be found in chapter 5. This chapter is structured in the following way:

Section 4.1 presents the results of the experiments in traction curves elaborated with observations.

Section 4.2 provides the outcome of the calculated film thickness in the contacts of the experiments. These calculated film thicknesses are used in the following sections of this chapter.

Section 4.3 shows the results of all fitted parameters to describe the rheological behavior of the lubrication oil. Parameters such as the z value, pressure viscosity coefficient, Roelands parameters and the Eyring stress are discussed within subsections of this section.

Section 4.4 shows the results of the stress strain curves obtained with the fitted rheological parameters.

Section 4.5 states when viscous shear heating can be predicted with taking the fitted parameters into account.

The last section of this chapter, section 4.6, states whether viscous shear heating is predicted within the cold rolling process and if so, what the connection is that links viscous shear heating to the cold rolling process.

4.1 MTM results

The output files of the MTM experiments are text files containing data such as the SRR, sliding speed, entrainment speed, traction force and the CoF. The sliding speed and traction forces are important data that is needed to determine the rheological parameters of the lubricant and will be used later on. For each temperature the traction curves can be shown by plotting the CoF against the SRR.

While testing with the $1/2$" ball certain issues occurred with the testing range specified in subsection 3.2.4. The machine was not capable of running the tests at an entrainment speed of $U = 2\ m/s$ and exceeding a SRR of $85\ \%$. The reason behind this is not quite clear, but the assumption is that because of the smaller disc the machine has to rotate faster to achieve the desired speed. Another assumption is that the shaft of the ball is extended by an extension part which elongates the shaft. Therefore it is less rigid and has more trouble staying stable.

Appendices B.1 and B.2 contain all traction curves for the $3/4$" and $1/2$" ball respectively. Some traction curves are shown in Figure 26, where the figures on the left side are traction curves obtained with the $3/4$" ball and the right side shows traction curves obtained with the $1/2$" ball.

Observation 1
The first observation is that the tests run at an entrainment speed of $U = 2\ m/s$ for the $3/4$" ball shows drastic falls in the CoF at the end of the traction curve when reaching a $SRR > 120\%$. To make sure that this drop is not due to viscous shear heating some more experiments were carried out within the range of $100\% < SRR < 150\%$ with small interval steps. Unfortunately the machine showed again instantaneous drops or spikes in CoF, approximately around a SRR of 130%. When reaching this value the machine was making a hard grinding noise. It could be due to the fact that the speed of the ball or disc was reaching the speed limit of the MTM and the machine had trouble taking stable measurements. A slide to roll ratio of $SRR = 150\%$ and an entrainment speed of $U = 2\ m/s$ corresponds to speeds of $u_1 \approx 0.5\ m/s$ and $u_2 \approx 3.5\ m/s$, which is close to the speed limit of the MTM. In further computations and analyses the last measuring point of the SRR will be neglected, because these measurements are not reliable.

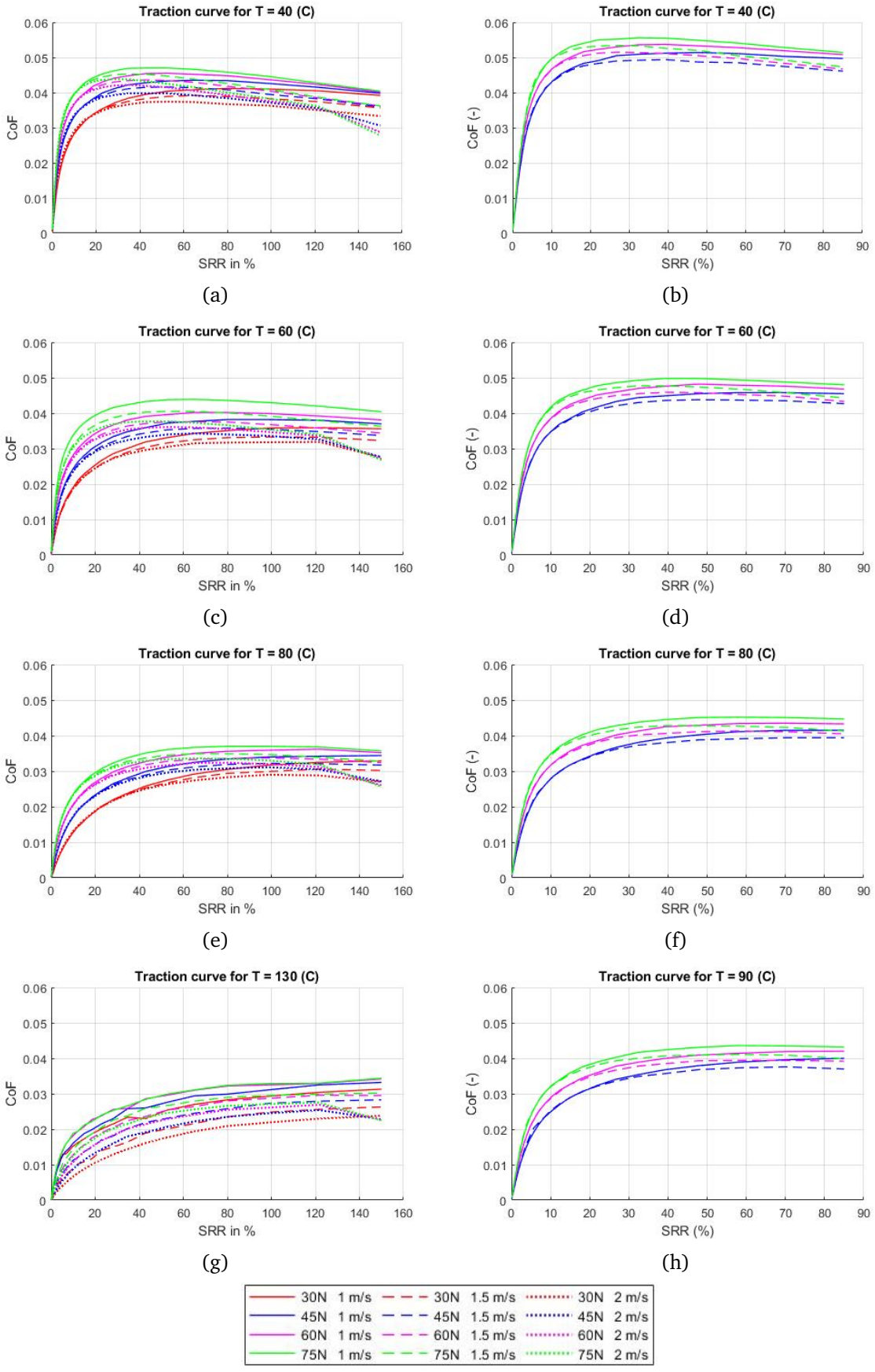

Figure 26: Traction curves at the left side for the $3/4$" ball and on the right side $1/2$" ball.

Observation 2
The second observation is that viscous shear heating occurs more dominantly at lower temperatures than at higher temperatures. As stated before, the traction curves starts with a big increase in CoF and levels out, followed by a minor drop. This dropping phenomena is characterized by viscous shear heating. It can be seen that the traction curves at a condition of $T = 40\,°C$, shown in Figure 26a and Figure 26b, levels and drops, but the traction curves fo $T = 130\,°C$, shown in Figure 26g, do not show this phenomena. Therefore it can be seen that viscous shear heating probably occurs sooner in lower temperatures in contrast to higher temperatures. This is probably because of the fact that at high temperatures, the change in viscosity is less than at lower temperatures. The curves show viscous shear heating behavior up until a temperature of $T = 90\,°C$. Later in the report it is exactly determined under which conditions viscous shear heating starts to occur.

Observation 3
Another observation is that the traction curves start to become 'wobbly' at a temperature of $T = 130\,°C$. When examining the traction curve shown in Figure 26g for a normal load of $F_n = 45\ N$ and an entrainment speed of $U = 1\ m/s$, indicated by the solid blue line, it shows irregular fluctuations. The assumption is that the viscosity of the oil dropped due too a relative high temperature which results in a decreased film thickness such that the mixed lubrication regime becomes active. This assumption is further investigated in section 5.1 after which the film thickness is obtained and the film parameter can be computed for the different conditions.

Observation 4
The final observation is that the traction curves at a low temperature show a clear distinction between the different pressures within the lower SRR values, but this division gradually diminishes when temperature rises. At a temperature of $T = 90\,°C$ the distinction is there between the normal loads of $F_n = 30\ N$ and $F_n = 15\ N$, but for higher normal loads and thus pressures this distinction is not as clear. At a temperature exceeding $T = 110\,°C$ the distinction between pressures has disappeared. The reason for this phenomena is most likely the same as stated in the earlier observation that the mixed lubrication regime is active. For this reason the measurements for $T = 110\,°C$ and $T = 130\,°C$ are excluded from further analyses and computations.

4.2 Film thickness

The film thickness is calculated with Moes (Equation 24) for every single traction curve. The film thickness is plotted in Figure 27 against the pressure for multiple entrainment speeds. Note that the film thickness shown in these figures are theoretical data calculated with the computational approach as explained in section 3.3 and not direct measured values.

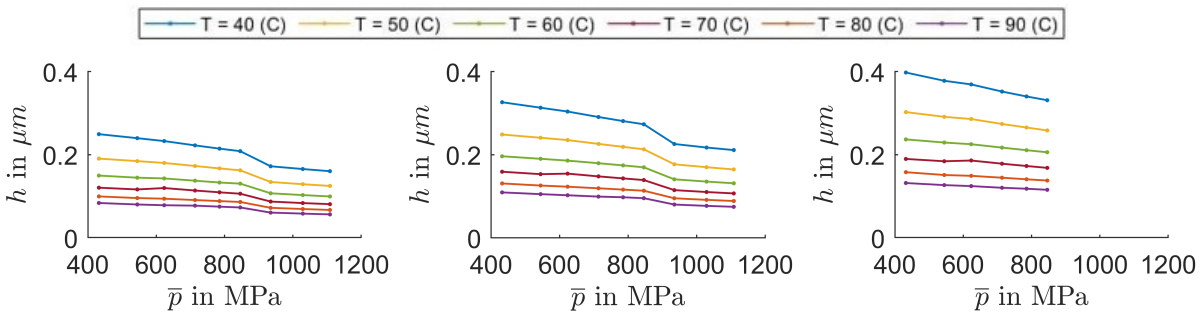

(a) $U = 1\ m/s$ (b) $U = 1.5\ m/s$ (c) $U = 2\ m/s$

Figure 27: Calculated film thickness by Moes, plotted against pressure for the three different entrainment speeds.

From theory it is known that the film thickness is dependent on the viscosity of the lubricant in the inlet zone. A thick film results from a lubricant with high viscosity, which can be recognized in Figure 27 by the temperature conditions. Decreasing the temperature results in higher viscosity, which subsequently results in a thicker film.

On the contrary, increasing the mean pressure in the contact zone results in a relative small decrease in film thickness. The film thickness decreases linearly with respect to pressure, but shows a big drop from $\overline{p} = 846\ MPa$ to $\overline{p} = 935\ MPa$. This drop is a result from changing the ball specimen from the $3/4$" ball to the $1/2$" ball. The variation in ball size affects the inlet angle and therefore the film thickness. Prior research by Jacobs [22] showed the importance of inlet angle on the film thickness.

It is also known from theory that a higher entrainment speed should also lead to an increase in film thickness, which can be easily seen in the three different plots for the film thickness shown in Figure 27. The film thickness at a temperature of $T = 40\ °C$ and an entrainment speed of $U = 1\ m/s$ is $h \approx 0.25 \times 10^{-6}\ m$, while the film thickness at an entrainment speed of $U = 2\ m/s$ at the same temperature is approximately $h \approx 0.4 \times 10^{-6}\ m$. To obtain a better visualization of the influence of the entrainment speed on the film thickness, the film thickness is plotted against the entrainment speed in the following figure.

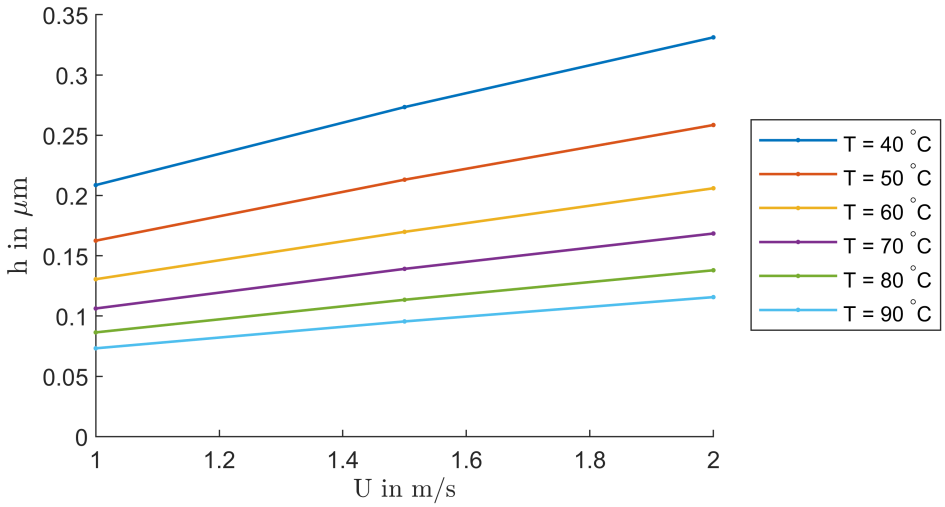

Figure 28: Fitted film thickness against the entrainment speed at a pressure of $\overline{p} = 846\ MPa$ for different temperatures.

Figure 28 shows the film thickness against the entrainment speed for different temperatures and a fixed mean pressure of $\overline{p} = 846\ MPa$. This figure shows clearly that the film thickness is dependent on the entrainment speed for a fixed pressure. It can be noted that the film thickness increases more with entrainment speed for lower temperatures, which probably is a result of a higher viscosity for a relative low temperature.

4.3 Rheological parameters

This section delves into a detailed analysis of results for the parameters needed to describe the rheological behavior of the EHL contact formed by the lubrication oil used at Tata Steel. This section starts off with a subsection that states the parameters needed to compute the viscosity. The following subsection states the results of the pressure viscosity coefficient, followed by a subsection which presents the results of the Eyring stress, which is needed to compute the theoretical shear stress.

4.3.1 Viscosity parameters

This subsection elaborates on the fitted parameters for the Roelands equation, specified in Equation 12 and repeated below.

$$\eta(p,T) = \eta_s \exp\left[\left(\ln\frac{\eta_s}{\eta_0} + 9.67\right)\left(\left[\frac{p-p_0}{p_s-p_0}\right]^z \left[\frac{T_s-T_0}{T-T_0}\right]^{s_0} - 1\right)\right]$$

The s_0 value will be fitted by measuring the viscosity at atmospheric pressure for multiple temperatures. Figure 29 shows the experimental results from the Rheo Haake Stress 6000. The viscosity at ambient pressure η_a shows a decrease with respect to temperature which is expected. The base viscosity, which is the ambient viscosity at a temperature of $T_s = 40\ °C$, is measured as $\eta_s = 0.03657\ Pas$. The Roelands fit through the experimental data values showed the best fit with a value of $s_0 = 1.0014$. With these parameters the ambient viscosity can be determined by Roelands for every temperature at ambient pressure, see following equation.

$$\eta_a(T) = \eta_s \exp\left[\left(\ln\frac{\eta_s}{\eta_0} + 9.67\right)\left(\left[\frac{T_s-T_0}{T-T_0}\right]^{s_0} - 1\right)\right] \tag{33}$$

The Roelands parameters can be found in Table 2.

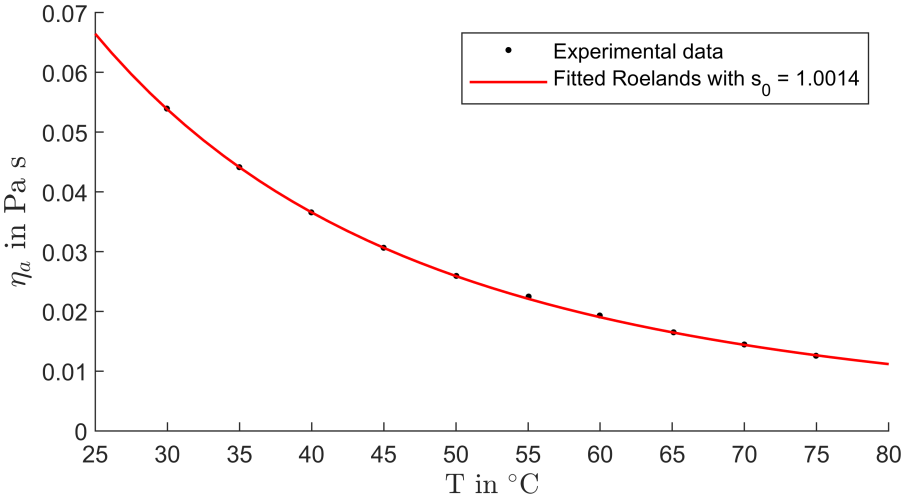

Figure 29: Experimental data of the viscosity of the lubrication oil and the fitted Roelands equation under atmospheric pressure.

With s_0 and η_s known, the z value can be determined by using the experimental data from the MTM and the computational approach shown in Figure 24. The results of this computational approach gives a z value for every traction curve measured by the MTM. These z values are plotted by dots against the temperature in Figure 30. The colors of the dots corresponds with the pressures mentioned in the legend, resulting in three points for each pressure-temperature combination up to a pressure of $\overline{p} = 846\ MPa$ and two points for $\overline{p} = 935\ MPa$ and beyond. These points represent the different entrainment speeds. The limitation of only having two points for higher pressures arises from the inability to run at an entrainment speed of $U = 2\ m/s$ for the $1/2$" ball. However, as can be seen in Figure 30, the entrainment speed has a negligible influence on the z value.

Almost all z values fall within the range of $0.45 < z < 0.6$. The z value increases slightly with increasing temperature, but also increases with decreasing pressure. However literature states

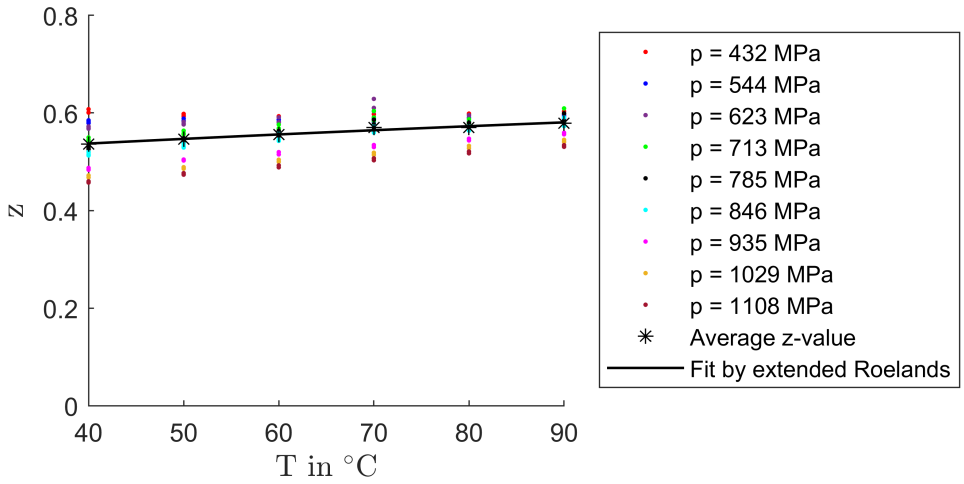

Figure 30: z values fitted by the computational approach and the fitted z by the extended Roelands equation represented by the black line.

that z is only dependent on temperature and can be calculated with the extended Roelands equation (Equation 21, repeated below).

$$z = D + C \ln\left(\frac{-T_0}{T - T_0}\right)$$

Too fully describe the viscosity by Roelands, the C and D constants can be fitted with the computed z values out the computational approach. The average of the z values is taken for every temperature measurement and plotted with the black star. The black line shows the best fit by the extended Roelands equation through all the z values. The best fit to describe the z values by the extended Roelands equation is with the constants $C = -0.17$ and $D = 0.49$. All parameters to determine the viscosity using Roelands theory are gathered in Table 2.

Table 2: Roelands parameters

Universal constants	Oil constants
$\eta_0 = 1\ Pa\ s$	$\eta_s = 0.03657\ Pa\ s$
$T_0 = -135\ °C$	$T_s = 40\ °C$
$p_0 = -0.2\ GPa$	$p_s = 101325\ Pa$
	$C = -0.17274$
	$D = 0.49239$
	$s_0 = 1.0014$

4.3.2 Pressure viscosity coefficient

The pressure-viscosity coefficient, denoted as α^* is defined as the rate of change in viscosity with pressure. A high pressure viscosity coefficient indicates that the viscosity will increase more by pressure than with a relatively low pressure viscosity coefficient.

Within the computational process used in this thesis, the pressure-viscosity coefficient is calculated by Blok (Equation 23), utilizing the converged z value represented by the dots in Figure 30. Therefore, every computed α^* corresponds with a z value shown in Figure 30.

The range of the pressure-viscosity coefficient falls in between $11\ GPa^{-1} < \alpha^* < 18\ GPa^{-1}$.

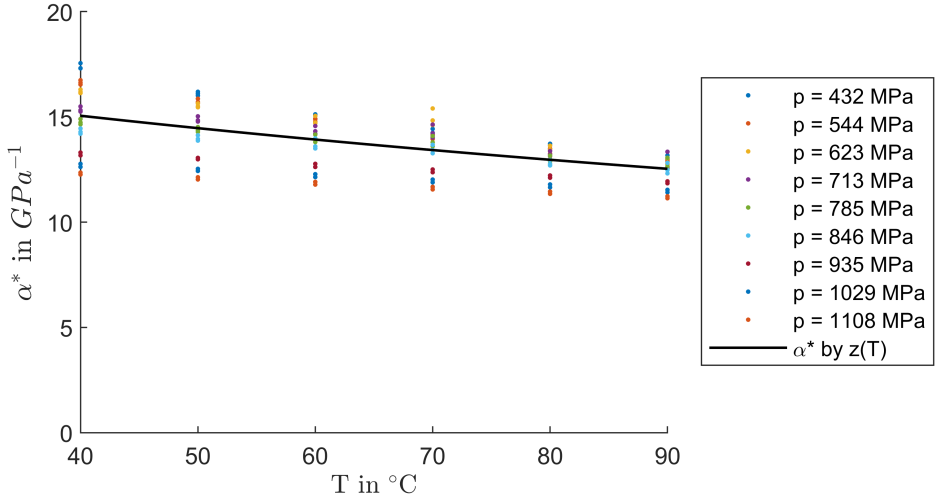

Figure 31: Pressure viscosity coefficient computed by Blok with the computational approach. The black solid line is the pressure viscosity coefficient as a function of the extended Roelands equation.

A rise in temperature results in a decrease of the pressure-viscosity coefficient. It is worth noting that α^* is influenced by pressure as can be seen from the range of z values for one fixed temperature, which is in contradiction with theoretical expectations. The range of the pressure-viscosity coefficient falls in between $11\ GPa^{-1} < \alpha^* < 18\ GPa^{-1}$. A rise in temperature or an increase in pressure results in a decrease of the pressure-viscosity coefficient.

The black solid line plotted in Figure 31 represents the pressure-viscosity coefficient derived from the equation of Blok using the z value calculated based on the extended Roelands equation with the corresponding fitted parameters shown in Table 2.

4.3.3 Eyring stress

The Eyring stress τ_e is the shear stress at which the lubrication oil starts to exhibit shear thinning behavior and transitions from Newtonian to non-Newtonian. This parameter is needed for modelling shear thinning behavior by the model of Eyring (Equation 14).

The obtained values for the Eyring stress are plotted against the pressure and shown in Figure 32. The points represents the Eyring stresses fitted with the computational approach for different temperatures and pressures. The three different entrainment speeds are plotted in one graph to clearly visualize the small difference and fitted by one exponential function of the form, $\overline{\tau}_e = a\ exp(b\ \overline{p}) + c$ in MPa. This is repeated for all six different temperatures. The parameters for a, b and c can be found in Table 3 along with the coefficient of determination R^2 in the last column, which represents the measure of how well the function fits the data.

The Eyring stress increases with increasing pressures, but decreases with increasing temperature. At a low pressure of approximately $\overline{p} \approx 500\ MPa$, the Eyring stress is equivalent for all temperatures with a magnitude of $\tau_e \approx 4\ MPa$. From this pressure onward, the Eyring stress increases slightly up to a mean pressure of $\overline{p} \approx 900\ MPa$. Exceeding this pressure, the Eyring stress increases more rapidly for all temperatures, which is probably a result of different size specimen.

From Figure 32, it can be concluded that the lubrication oil exhibits the longest duration of Newtonian behavior under conditions of high pressure and low temperature. This means that the oil maintains a constant viscosity for a more extended range of shear rates, before transitioning

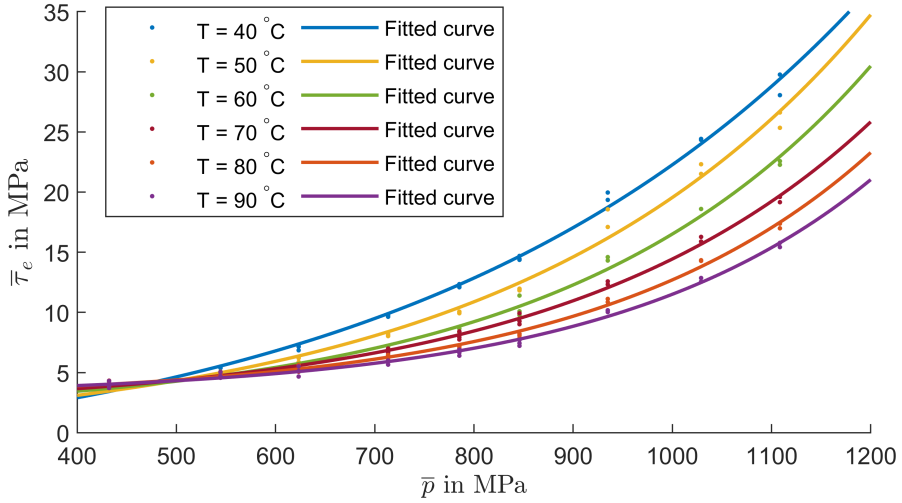

Figure 32: Results of Eyring Stress from computational approach, plotted against the mean pressure for different temperatures. Results are fitted with an exponential function of the form $\overline{\tau}_e = a\, exp(b\, \overline{p}) + c$.

to shear thinning behavior. Conversely, the lubricant starts to show early signs of shear thinning behavior when subjected to low pressures, independent of temperature.

Table 3: Parameters fit for Eyring stress.

Temperature	a	b	c	R^2
$T = 40\ °C$	2.90	0.0022	−4.10	0.996
$T = 50\ °C$	1.22	0.0028	−0.65	0.989
$T = 60\ °C$	0.59	0.0033	1.29	0.992
$T = 70\ °C$	0.50	0.0032	1.84	0.995
$T = 80\ °C$	0.26	0.0036	2.76	0.994
$T = 90\ °C$	0.20	0.0038	3.03	0.992

4.4 Stress strain curves

All traction curves shown in appendices B.1 and B.2 are converted to stress strain curves with the fitted parameters discussed in the previous section. The stress strain curves for all conducted experiments can be found in appendix B.3.

Figure 33 shows the stress strain curves for the conditions of $T = 40\ °C$ and $T = 90\ °C$ at an entrainment speed of $U = 1\ m/s$. The dots represent the experimental shear stress obtained from experimental data, while the solid lines represent the theoretical shear stress modeled using Eyring (Equation 14). The experimental shear stress show a good fit with the Eyring model. The shear stress increases exponentially at low shear rates followed by the shear thinning region, which is linear on the logarithmic scale. At a higher shear rate the experimental shear stress deviates negatively from the theoretical shear stress and is therefore not accurately described by Eyring due to viscous shear heating of the lubricant, which will be elaborated in the next section.

For low pressures and higher temperatures, experimental data shows good agreement with theoretical predictions over a wider range. However, at higher pressures, the experimental shear stress can deviate significantly from theoretical values, indicated by the negative deviation. This suggests that viscous shear heating begins to influence the results earlier in the shear rate range.

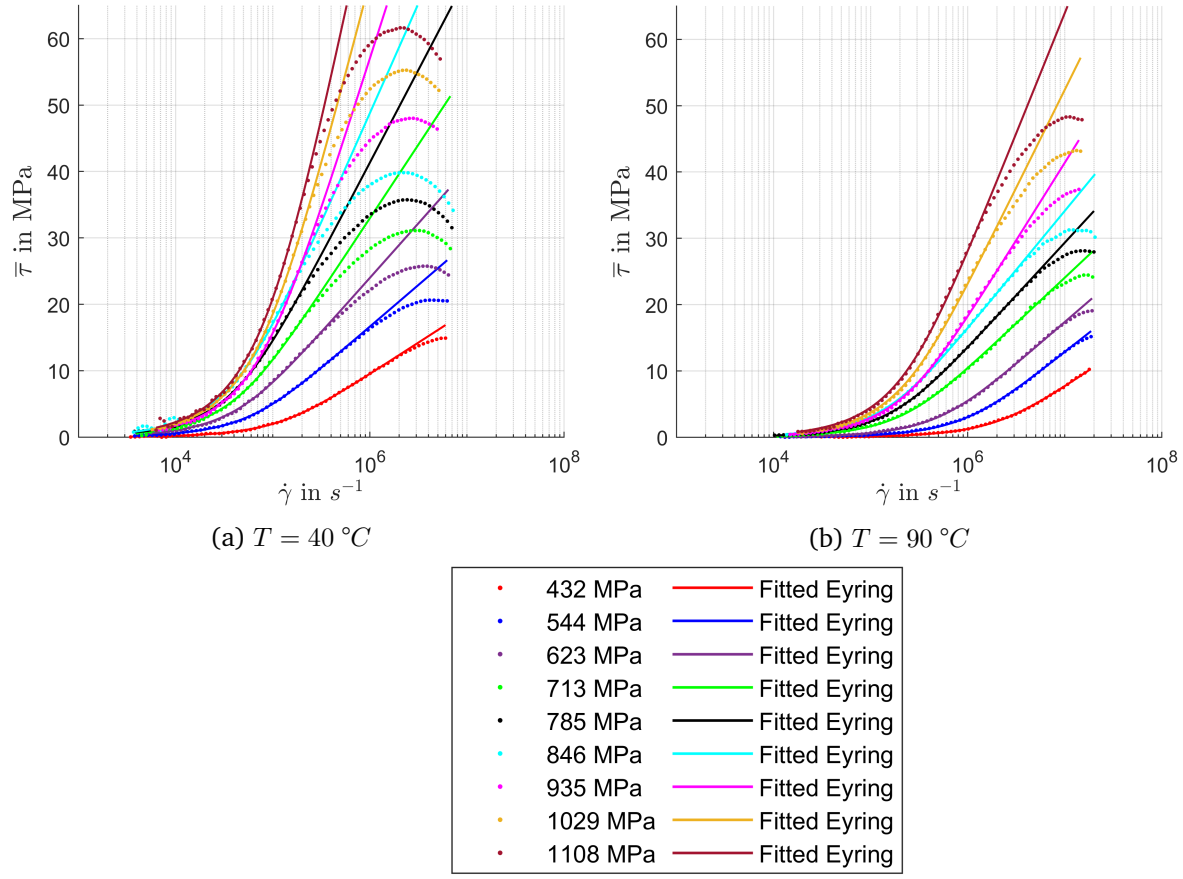

Figure 33: Experimental shear stress and theoretical shear stress modelled by Eyring at an entrainment speed of $U = 1\ m/s$.

Ignoring the effect of viscous shear heating at high pressures can result in substantial errors when predicting shear stress at high shear rates by the model of Eyring. For example, at a pressure of $\overline{p} = 935\ MPa$ and a temperature of $T = 90\ °C$ and a shear rate of $\dot{\gamma} = 10^7\ s^{-1}$, the experimental shear stress is approximately $\overline{\tau}_{exp} = 36\ MPa$, which is $6\ MPa$ lower than the theoretical shear stress at $\overline{\tau}_{theory} = 42\ MPa$. This results in an error of $14,3\ \%$. The error is even larger when looking at the same pressure, but at a temperature of $T = 40\ °C$ and a shear rate of $\dot{\gamma} = 10^6\ s^{-1}$. Experimental shear stress under these conditions is measured at $\overline{\tau}_{exp} = 45\ MPa$, while the theoretical shear stress by Eyring has a value of $\overline{\tau}_{theory} = 57\ MPa$, resulting in an error of $21\ \%$. These errors show that it is important to include the effect of viscous shear heating in friction models when operating at high shear rates, especially at high pressures and low temperatures.

The influence of temperature and pressure on shear stress is significant, while the effect of entrainment speed is negligible. It can be seen in Figure 33 that an increase in pressure results in higher shear stresses and an increase in temperature results in lower shear stresses. Figure 34 presents stress-strain curves at $T = 90\ °C$ and $\overline{p} = 623\ MPa$ for different entrainment speeds. The small separation between the curves for various speeds is negligible compared to the effects of temperature and pressure. The minimal influence of entrainment speed on shear stress will be further discussed in section 5.3.

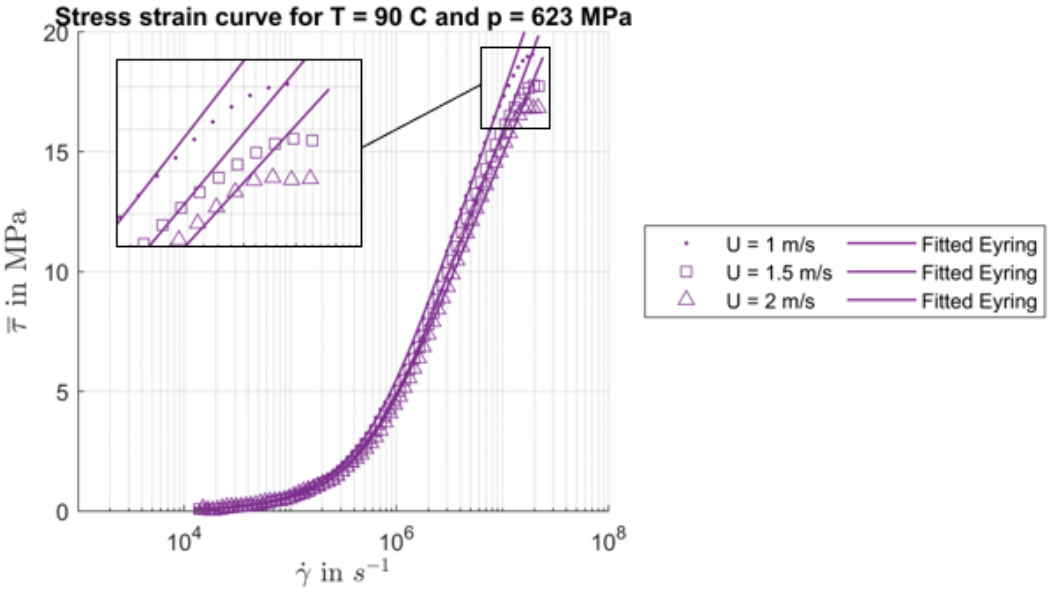

Figure 34: Stress strain curves at $T = 90\,°C$ and $\overline{p} = 623\ MPa$ with fitted Eyring model for different entrainment speeds.

4.5 Starting point of viscous shear heating

As previously discussed, the onset of viscous shear heating, denoted by $\dot{\gamma}_L$, is indicated the threshold till which Eyring theory fits the experimental based shear stress. The negative deviation from the Eyring is a result from frictional heating effects within lubricant film. Viscous shear within the oil becomes that significant that the oil heats up causing a reduction in the viscosity, which subsequently results in a decrease of mean shear stress. The close up in Figure 34 shows a clear image of this point where the experimental data starts to deviate from the Eyring fit and show effects of viscous shear heating. It can be seen that for lower pressures the Eyring fit holds longer and therefore the shear rate from which viscous shear heating starts is higher. Contrarily, higher temperatures results in higher limiting isothermal shear rates. The limiting isothermal shear rate is determined for each stress strain curve obtained from the experimental data from the MTM experiments. All stress strain curves can be found in Appendix B.3.

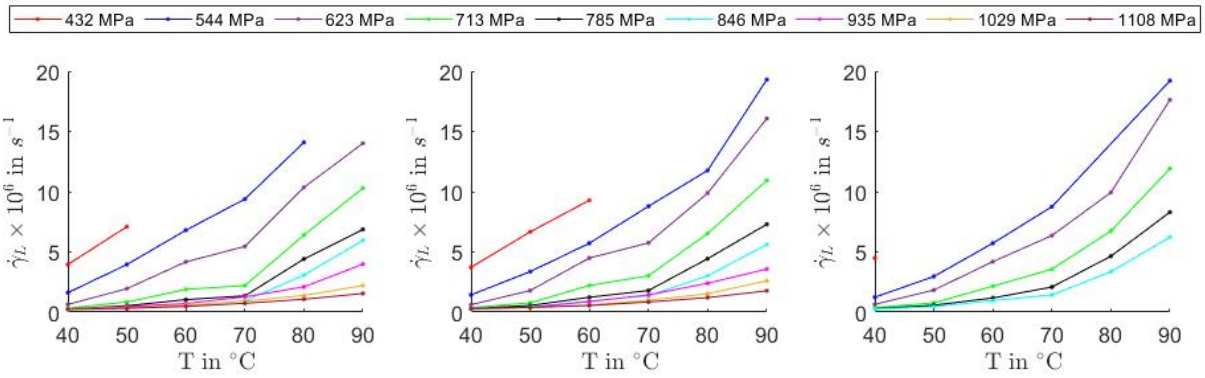

(a) $U = 1\ m/s$ (b) $U = 1.5\ m/s$ (c) $U = 2\ m/s$

Figure 35: Onset of viscous shear heating against the pressure for different temperatures.

Figure 35 illustrates a visual representation of the onset of viscous shear heating for multiple pressures against the temperature at different entrainment speeds. The aforementioned statements about higher temperature leading to a higher limiting isothermal shear rate and a higher

pressure resulting in a lower shear rate can be easily recognized in these graphs. The influence of entrainment speed appears to have minimal impact on the limiting isothermal shear rate. Another observation is that for certain lower pressure conditions at higher temperatures, no limiting isothermal shear rate is present. This absence is due to the fact that the shear stress based on experimental data remains in alignment with the Eyring theory and does not deviate, thus no viscous shear heating is detected.

All data points from the three graphs for the different entrainment speeds shown in Figure 35 are plotted in one graph so the negligible effect of the entrainment speed can be clearly visualized. The data points are plotted in Figure 36. A curve is fitted through the different entrainment speeds to guide the eye for obtaining the onset of viscous shear heating.

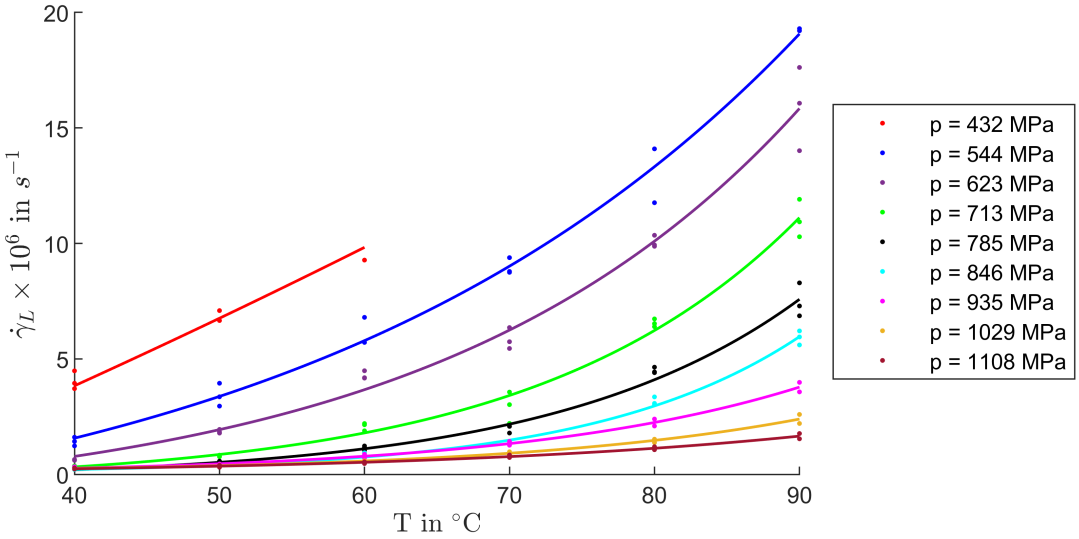

Figure 36: Shear rate at which viscous shear starts to occur, plotted against the temperature for multiple pressures. Curves are fitted to guide the eye.

The expectation mentioned in section 3.4 suggested that the limiting isothermal shear rate would likely be in the range of the order $\dot{\gamma}_L \approx 10^6 - 10^7\ s^{-1}$. However, results reveals that the actual range is bounded by $2 \times 10^5 < \dot{\gamma}_L < 2 \times 10^7\ s^{-1}$. The hypothesis was based on previous studies and experiments with an ester based lubrication oil. It can be stated that the rheological parameters can differ within ester oils and therefore the hypothesis was partly incorrect.

The onset of viscous shear heating depends on pressure and temperature. A lower temperature results in earlier start of viscous shear heating, while lower pressures results in viscous shear heating starting at higher shear rates. The entrainment speed has a negligible effect on the onset of viscous shear heating. The latter seems to be in contradiction with existing literature [62] and will be further discussed in section 5.3.

4.6 Viscous shear heating in the cold mill

In the following section the aspect of viscous shear heating within the cold rolling process will be explained. This section starts with modelling standard operational conditions in a cold mill. The second part elaborates on the location of viscous shear heating within a stand of the cold mill using shear rate as indication. The last aspect in this section is whether viscous shear heating is expected to occur in a standard process of the cold mill.

4.6.1 Cold mill in operation

Cold mill 11 and cold mill 12, which are 4-stand and 5-stand mills respectively, as schematically in Figure 1, are considered under standard operational conditions. These operational conditions such as work roll velocity, strip thickness, material yield stress, reduction and surface roughness are obtained from an internal report. It is assumed that the film thickness is constant along the roll bite and equal to the surface roughness of the work roll, $h = R_a$. The correctness of this assumption is discussed in section 5.4. However the strip velocity at the entry or exit of the stands is still unknown, but given the importance of the sliding speed in viscous shear heating, it can be determined using Equation 1 assuming a forward slip of $S_{fw} = 5\ \%$. This results in a an exit strip speed of $u_{out} = 1.05 u_{roll}$ and the incoming strip speed of a stand can be calculated using the principle of mass conservation:

$$u_{in} = \frac{t_{out} \cdot u_{out}}{t_{in}} \tag{34}$$

The following computations are carried out for all 9 stands, but due to repetitive calculations, only the first stand of CM (Cold Mill) 12 is elaborated in this subsection. Results of other stands can be found in Appendix D. The geometry of stand 1 is shown in Figure 37. Note that only the upper half of the strip and a portion of the upper work roll is shown, because the process is symmetric along the centerline of the strip. Considering this geometry, the velocity profile within the work zone can be calculated using the mass conservation equation (Equation 34). As the strip thickness decreases by following the profile of the work roll, the velocity of the strip increases. The velocity profile of the strip at stand 1, along with the constant velocity of the work roll is shown in Figure 38. The intersection, where both velocities are equivalent, indicates the location of the neutral point.

Given the known velocities of the strip and the work roll, the sliding speed Δu can be computed. With the sliding speed and film thickness known, the shear rate can be computed by $\dot{\gamma} = \Delta u / h$ (Equation 9). The shear rate distribution over the rolling direction of stand 1 is plotted in Figure 39. The maximum shear rate in a stand occurs at the entry of the work zone, where the sliding speed is high and the film thickness low. As the neutral point shifts towards the entry the sliding speed will decrease in the inlet and increases at the outlet. However assuming a forward slip of approximately $S_{fw} \approx 5\ \%$ for each stand, the maximum shear rate will consistently be located at the entry of each stand and will be denoted as $\dot{\gamma}_{entry}$. Figures 37, 38 and 39 are computed for all 9 stands and can be found in Appendix D.

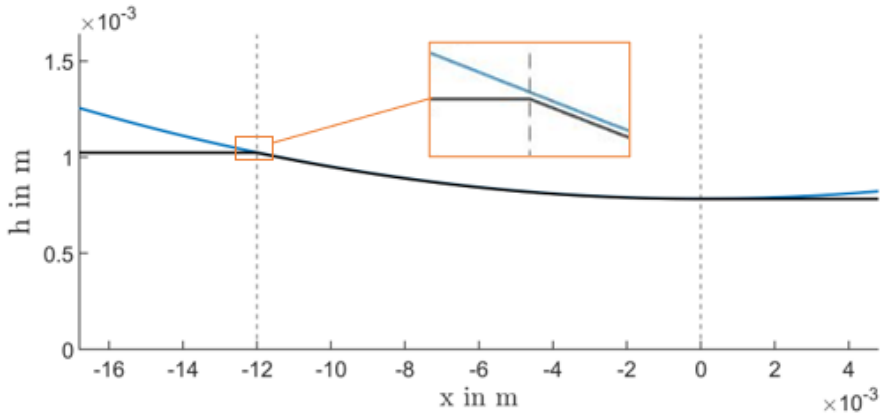

Figure 37: Geometry of the work roll (blue) and the strip (black) of stand 1, where the vertical dashed lines mark the boundaries of the work zone.

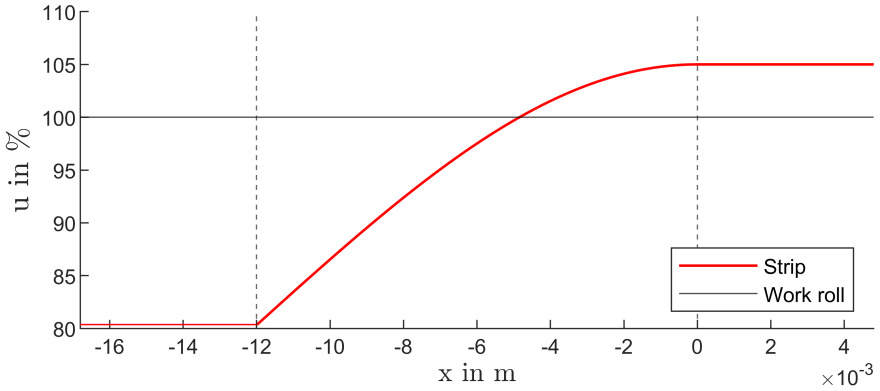

Figure 38: Velocity of the work roll and strip in percentage of stand 1 over rolling direction x. The vertical dashed lines mark the boundaries of the work zone.

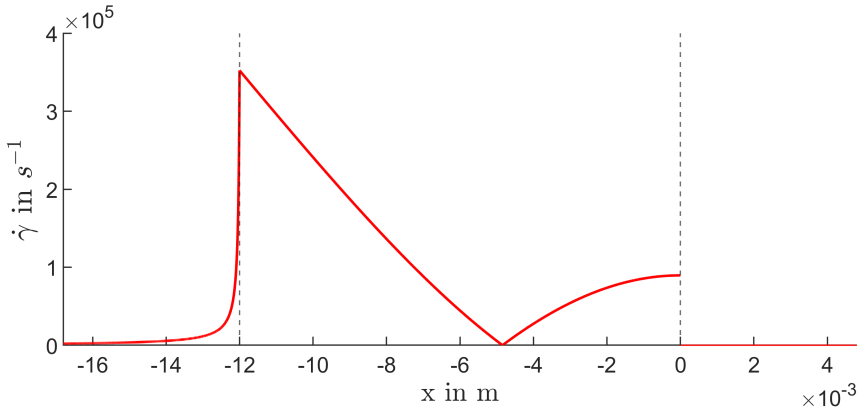

Figure 39: Estimated shear rate in the lubricant of stand 1 over rolling direction x. The vertical dashed lines mark the boundaries of the work zone.

4.6.2 The appearance of viscous shear heating within the cold mill

The shear rate at the entry is computed for all 4 stands of cold mill 11 and 5 stands of cold mill 12 and the values are shown in Table 4. The entry shear rates of the 9 stands lays within the range of $3.5 \times 10^5 < \dot{\gamma}_{entry} < 1.0 \times 10^7\ s^{-1}$.

Table 4: Entry shear rate per stand of cold mill 11 and 12.

Stand	1	2	3	4	5
$\dot{\gamma}_{entry}$ of CM 11 in s^{-1}	0.6×10^6	2.4×10^6	6.2×10^6	8.4×10^6	-
$\dot{\gamma}_{entry}$ of CM 12 in s^{-1}	0.4×10^6	1.8×10^6	2.2×10^6	9.7×10^6	10.3×10^6

To determine if viscous shear heating is to be expected within the cold rolling process, the order of the entry shear rate is compared to the order of the limiting isothermal shear rate. In section 4.5 it is concluded that viscous shear heating starts within the range of $2 \times 10^5 < \dot{\gamma}_L < 2 \times 10^7\ s^{-1}$. This is within the same range of the entry shear rates in the cold mills, so viscous shear heating might occur. However, the limiting isothermal shear rate as shown in Figure 36 is dependent on temperature and pressure. Therefore the temperature and pressure at the entry of the roll bite are taken into account.

Figure 40 shows the fitted lines of Figure 36 of the pressures that are relevant within the stands of the cold rolling process. The markers in the graph represents the estimated shear rate at

the entry of each stand, as presented by Table 4. The diamond, square, star, triangle and circle figures represents stands 1 to 5 respectively. Open figures corresponds to CM 11, while solid figures corresponds to CM 12. The colors of the markers indicate at which pressure the stands operate.

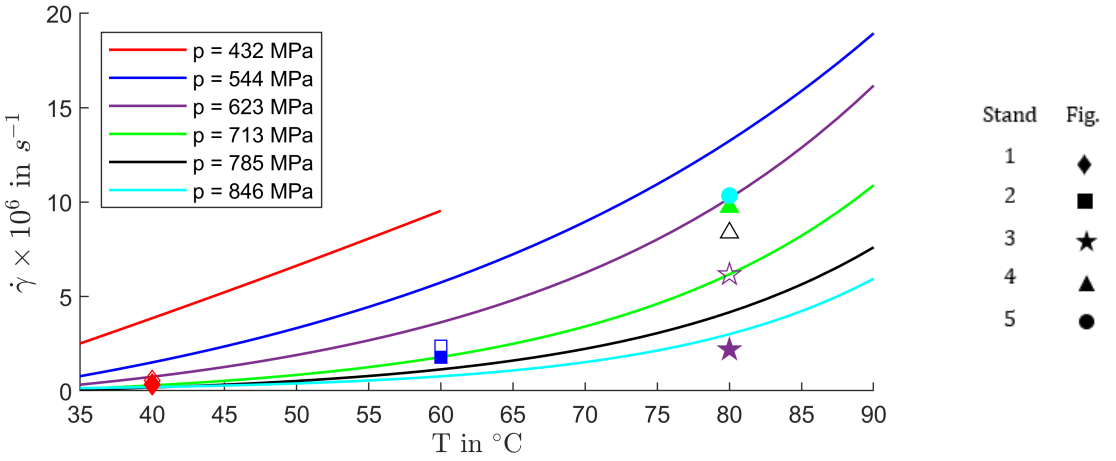

Figure 40: Estimated entry shear rate of CM 11 (open) and CM 12 (solid) compared to the limiting isothermal shear rate.

For stand 1 of both cold mills, the operating pressure is $p \approx 432\ MPa$ and temperature $T = 40\ °C$. The entry shear rate in stand 1 is $\dot{\gamma}_{entry} = 0.6 \times 10^6\ s^{-1}$ for CM 11 and $\dot{\gamma}_{entry} = 0.4 \times 10^6\ s^{-1}$ for CM 12, while viscous shear heating at the corresponding pressure and temperature starts occurring at $\dot{\gamma}_L \approx 4 \times 10^6\ s^{-1}$. Thus it can be concluded that no viscous shear heating occurs at standard operating conditions for stand 1 at CM 11 and CM 12. When looking at stand 2 and 3 of both cold mills, indicated by the square and star respectively, it can be seen that the markers remain below the corresponding line indicated with the same color. Therefore the entry shear rate is below the limiting isothermal shear rate and no viscous shear heating is expected within these stands. Stand 2 operates at $p = 544\ MPa$, $T = 60\ °C$ and stand 3 operates at $p = 623\ MPa$, $T = 80\ °C$.

However, looking at stand 4 of CM 11, viscous shear heating is to be expected. The stand, indicated by the black triangle, operates at a pressure of $p = 785\ MPa$ and temperature $T = 80\ °C$. The entry shear rate within the stand is $\dot{\gamma}_{entry} = 8.4 \times 10^6\ s^{-1}$, while viscous shear heating starts occurring at $\dot{\gamma}_L \approx 4 \times 10^6\ s^{-1}$ under these conditions. Stand 4 and 5 of CM 12 also operates at conditions where viscous shear heating is to be expected.

It can be concluded that the location of viscous shear heating is to be expected at the entry of the work zone of each stand. The entry shear rate of the stands 1-3 of CM 11 and CM 12 remain below the limiting isothermal shear rate, so no viscous shear heating is expected within these stands. On the contrary, both stands 4 and stand 5 of CM 11 operate at a shear rate that exceeds the limiting isothermal shear rate and viscous shear heating is to be expected within these stands.

5 Discussion

This chapter will elaborate on some results, how it is obtained and the relation with the existing literature.

The chapter is organized in the following way:

Section 5.1 delves into the active lubrication regime during the experiments. This section focuses on the film thickness compared to the surface roughness of the specimens. By computing the film parameter it can be discussed whether the active lubrication regime ensures consistent full film lubrication throughout all experiments.

Section 5.2 discusses the location of viscous shear heating within the EHL contact and in the cold rolling process.

Section 5.3 questions the correctness of the applied computational approach to compute the limiting isothermal shear rate.

Section 5.4 elaborates on the assumption of the chosen film thickness across the work zone within the stands of the cold mill.

5.1 Surface roughness

As stated in observation 3 of section 4.1, the traction curves obtained at temperatures of $T = 110\,°C$ and $T = 130\,°C$ for the 3/4" ball showed 'wobbly' curves. These irregular fluctuations in curves are expected to be a consequence of the contact being in the mixed lubrication regime. For this reason these temperatures were excluded from further analyses and computations.

This section aims to examine whether the aforementioned conditions were indeed a consequence of the mixed lubrication regime. The active regime within a lubricated contact can be determined by the film parameter λ which can be calculated by Equation 4 and is repeated below.

$$\lambda = \frac{h}{\sqrt{\left[R_{q.strip}^2 + R_{q.roll}^2\right]}}$$

Within the computational approach the film thickness is calculated, leaving the consideration of the surface roughness parameter R_q. The manufacturer of the MTM specimens, PCS Instruments, provides a datasheet that states that the surface roughness parameter of ball and disc is $R_a < 20\ nm$, approximately equivalent to $R_q < 24\ nm$. R_a signifies the average of the absolute values of the profile heights and R_q denotes the root mean square average of the profile heights across an evaluation length. To validate the accuracy of these provided values, a new set of specimens are analysed under a microscope (Sensofar) with a 50x magnification. The surface parameter R_q is determined in the radial direction and the transverse direction at multiple positions and averaged to obtain one value. All values are reported in the surface roughness report which can be found in Appendix C. From these experiments it can be concluded that the new specimens have the following surface roughness values:

$$\begin{aligned} &\text{New disc:} && R_q = 9\ nm \\ &\text{New ball:} && R_q = 29\ nm \end{aligned}$$

The film parameter, denoted as λ, is computed for each traction curve to state whether the mixed lubrication regime is active. At a temperature of $T = 110\ °C$, the film parameter varies within

Table 5: Film parameter range for MTM experiments at different temperatures.

Temperature	New specimens	Used specimens
$T = 40\,°C$	$10.91 < \lambda < 13.10$	$5.52 < \lambda < 6.63$
$T = 50\,°C$	$8.51 < \lambda < 9.97$	$4.31 < \lambda < 5.04$
$T = 60\,°C$	$6.78 < \lambda < 7.81$	$3.43 < \lambda < 3.95$
$T = 70\,°C$	$5.55 < \lambda < 6.26$	$2.81 < \lambda < 3.17$
$T = 80\,°C$	$4.54 < \lambda < 5.21$	$2.30 < \lambda < 2.63$
$T = 90\,°C$	$3.81 < \lambda < 4.35$	$1.93 < \lambda < 2.20$
$T = 110\,°C$	$2.80 < \lambda < 3.17$	$1.42 < \lambda < 1.61$
$T = 130\,°C$	$2.14 < \lambda < 2.47$	$1.08 < \lambda < 1.25$

the interval $2.80 < \lambda < 3.17$ and at $T = 130\,°C$ it lies within $2.14 < \lambda < 2.47$. This implies that the mixed lubrication regime is indeed active. Conversely, at $T = 90\,°C$, the film parameter ranges from $3.81 < \lambda < 4.35$, indicating that the full film lubrication regime is active. The film parameter for all sets of experiments can be found in Table 5 under the column 'New specimens'.

However during testing the specimens showed signs of wear and a track was formed on both the disc and ball. This wear is assumed to be from testing at an entrainment speed of $U = 2\,m/s$. While testing at this speed the machine had trouble maintaining the stability of the ball shaft at elevated SRRs (SRR > 120%). Vibrations were observed in the ball shaft leading to unintended contact between the rotating ball and disc. After the first set of the testing procedure, indications of track formation became apparent and a new set of specimens were used to complete the remaining experiments. The used specimens are again observed with the Sensofar. From these images it can be seen that the disc shows more wear then the ball. This is due to the fact that the ball was changed from side halfway within the experiments, which gives a clean surface without any wear. Conversely, the disc can not be flipped and undergoes repeated contact with the ball along the same radius. The width of the wear track is measured as $L = 400\ \mu m$, which should correspond with double the contact radius. This contact radius is determined by Hertz theory and denoted with the letter r_a.

$$r_a = \frac{3\,F_n\,r_{ball}}{2\,E'} \tag{35}$$

where F_N represents the normal load applied to the ball, r_{ball} the radius of the ball and E' refers to the combined Young's modulus. The maximum contact radius will occur with the load of $F_N = 75\ N$ and the 3/4" ball ($r_{ball} = 9,525\ mm$), which results in a contact radius of $r_a = 336\ \mu m$. However images show a slightly wider contact width, potentially because of repetitive replacement of the specimens resulting in minor variations in zone of contact.

The surface roughness parameter is measured again over this contact length, utilizing the same technique as before, but only in transverse direction of the wear track. The root mean square average surface roughness parameters for the the used specimens are as followed:

$$\begin{aligned} \text{Used disc:} \quad & R_q = 48\,nm \\ \text{Used ball:} \quad & R_q = 36\,nm \end{aligned}$$

These findings suggest that the mixed lubrication regime is active at earlier stages of the experiments. The film parameter is recalculated with the R_q values obtained from the used disc and ball. Updated values for the film parameter are presented in Table 5 under the column 'Used

specimens'. It can be stated that the mixed lubrication is active from $T = 70\,°C$ onwards. The experimental procedure is carried out with a step wise temperature manner starting from low temperatures. The ball was flipped between the $T = 70\,°C$ and $T = 80\,°C$. This should indicate that the tests performed at $T = 70\,°C$ were partly active within the mixed lubrication regime and traction curves for $T = 80\,°C$ in the full film lubrication regime due to a clean surface of the ball specimen. When taking a closer look at the traction curves, shown in Figure 41, it can be seen that there is indeed a difference in traction curves. The traction curves measured at $T = 70\,°C$ exhibit less separation between pressures than the traction curves for $T = 80\,°C$ at low SRR, which indicates that the measurements were conducted in the mixed lubrication regime.

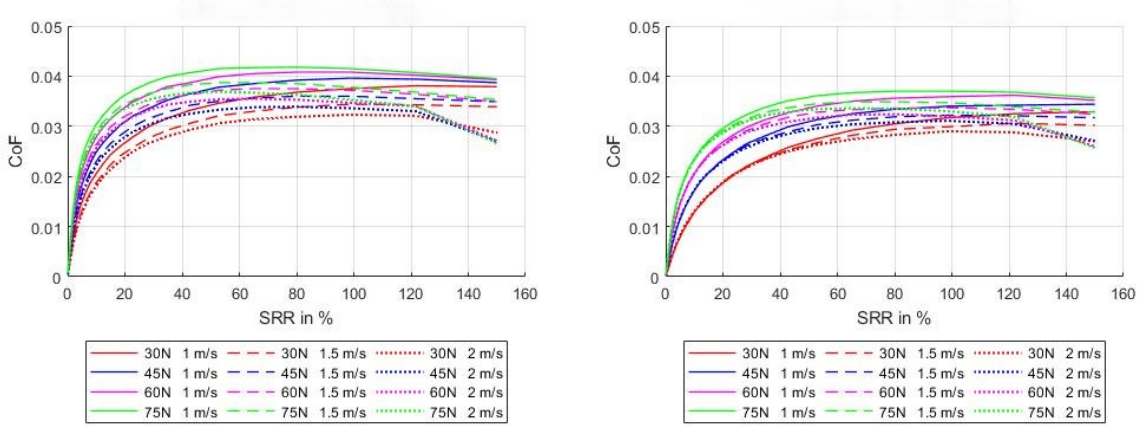

(a) $T = 70\,°C$ (b) $T = 80\,°C$

Figure 41: Traction curves from MTM experiments (3/4" ball) with conditions of $F_N = [30, 45, 60, 75]\ N$ and $U = [1, 1.5, 2]\ m/s$.

As mentioned in section 4.1 (observation 4), the division between the pressures becomes less with increasing temperature. It can be concluded that this is due to increasing surface roughness of the specimens which resulted in measuring within the mixed lubrication regime. However, the tests at $T = 80\,°C$ were performed with a clean surface of the ball specimen leading to full film regime in the measurements. The tests conducted at $T = 70\,°C$ and $T > 90\,°C$ are most likely in the mixed lubrication regime and thus less reliable.

5.2 Location of viscous shear heating

This section examines the location of viscous shear heating within ball-on-disc and cold mill contacts. Determining the location of viscous shear heating is crucial, as it significantly impacts contact conditions when viscous shear heating occurs in the inlet. The inlet conditions influence the film thickness in the work zone. Viscous shear heating in the inlet reduces viscosity, leading to a thinner film in the work zone. Therefore it is essential to identify the location of viscous shear heating.

5.2.1 Location of viscous shear heating within MTM experiments

Research has shown that in ball-on-disc setups, viscous shear heating occurs at the center of the contact zone [56]. As mentioned in section 2.3, the typical pressure distribution in an EHL contact follows a Hertz contact pressure distribution, with the maximum pressure in the middle of the contact. This pressure distribution for one of the MTM test conditions is plotted in Figure 42a. Viscosity increases with pressure and also peaks at the center of the contact, as plotted in Figure 42b. This central peak in viscosity creates the biggest resistance against

flow, resulting in the most heat generation at this point. This aligns with the existing literature by Spikes [56], as shown in Figure 19, who mapped the temperature rise across an EHL point contact. It can be seen that the highest temperature rise is at the center of contact.

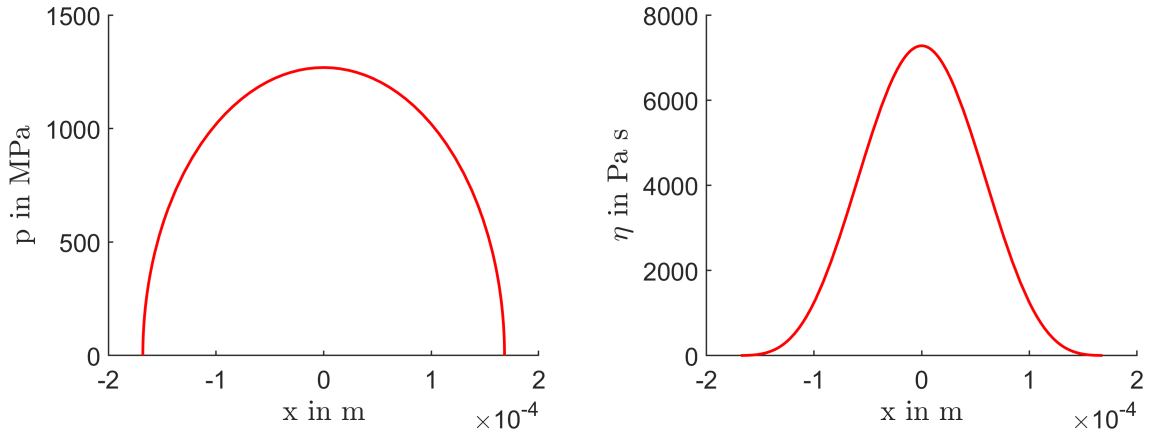

(a) Pressure distribution

(b) Viscosity distribution

Figure 42: Pressure and viscosity distribution of the ball on disc contact with the $3/4$" ball, a normal load of $F_n = 75\ N$ and at a temperature of $T = 40\ °C$.

This however is true for ball-on-disc EHL contacts, but existing literature discusses the location of viscous shear heating in rollers-on-flat EHL contacts. In roller-on-flat set ups, the location of viscous shear heating can occur in the inlet due to back flow. Not all lubricant formed in the inlet pool can be entrained into the contact and therefore some fluid flows in the opposite direction, also known as back flow. This back flow causes higher shear rates in the inlet zone, which can result in viscous shear heating. This phenomena is studied by Greenwood [63] and Murch [48] who derived correction factors for the film thickness within the contact due to thermal effects of back flow in the inlet zone. It can be discussed that the cold mill also acts like a roller on flat. The next subsection discusses the location of viscous shear heating within the cold mill.

5.2.2 Location of viscous shear heating within the cold rolling process

In subsection 4.6.1 it is stated that viscous shear heating is expected at the entry of the work zone of a cold mill stand. However it can be discussed if viscous shear heating already occurs at the inlet due to back flow. Trijssenaar [64] is one of the researchers who has studied back flow at the inlet zone of a cold mill. An illustration of the back flow in the inlet zone is shown Figure 43.

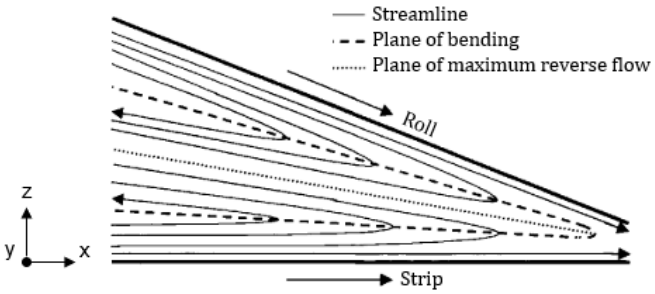

Figure 43: Back flow in the inlet zone over the rolling direction, adapted from [64].

As shown in Figure 43 the lubricant at $z = 0$ and $z = h$ flows at the speed of the strip and roll respectively. Closer towards the middle, there is a plane where the lubricant has zero forward

velocity, which is indicated as the bending plane. Between these two bending planes the lubricant flows back. Approximately in the middle between the strip and the roll, there is a plane where the reverse flow is at its maximum and is denoted with the dotted line. Trijssenaar [64] derived an equation (Equation 36) for the velocity in the rolling direction over the height.

$$u(z) = u_{roll}\left[r\frac{z}{h} - 3(2-r)\frac{h-h_0}{h^3}z(h-z) + (1-r)\right],\ 0 \leq z \leq h \tag{36}$$

With Equation 36 the back flow at the inlet zone for every stand can be calculated. Figure 44 shows the velocity in z-direction at stand 1 of CM 12 at height $h = 1\ mm$. The entry speed of the strip is $u_{entry} \approx 2\ m/s$ and the work roll has a velocity of $u_{roll} \approx 2.5\ m/s$.

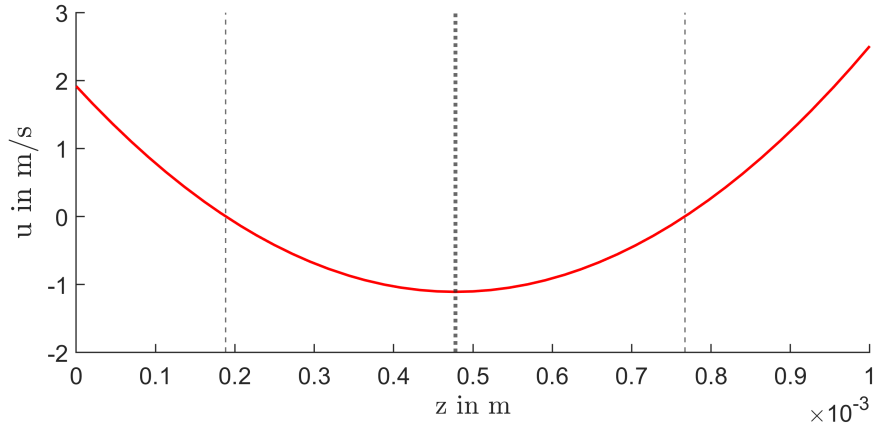

Figure 44: Velocity profile over z-direction at height $h = 1\ mm$ of stand 1 (CM 12), where the dashed lines represents the bending planes and the dotted line represents the plane of maximum reverse flow.

The velocity of the back flow is around $u_{bf} = 1\ m/s$. From computing the back flow of all stands it can be concluded that the higher the entrainment speed, the higher the back flow. The shear rate is defined as the gradient of the velocity over the z-direction ($\dot{\gamma} = \partial u/\partial z$). So with higher entrainment speeds and higher back flows, the gradient will be higher and therefore the shear rate increases. Taking the absolute average of the derivative of the profile shown in Figure 44, the shear rate can be calculated at this point. Repeating this for multiple heights in the inlet zone, the shear rate distribution can be captured over the rolling direction x. It must be noted that the back flow is constant along the inlet zone up to the stagnation point, where it rapidly decreases to zero. The stagnation point is the point where no back flow is present anymore and all lubricant enters the work zone. The absolute mean shear rate over the inlet zone, together with shear rate as computed in subsection 4.6.1 is plotted in Figure 45. It can be stated that the shear rate in the inlet is higher than the shear rate without taking the back flow into account.

The shear rate as computed by Trijssenaar shows a big peak at the entry of the work zone, however it can be discussed whether this peak makes sense. Out of calculations with the Trijssenaar model, back flow is present up till $0.034\ mm$ in front of the entry of the work zone, which seems unreasonable small. Another method to determine the stagnation point is with the equation of the Reynolds number, given in Equation 37. This formula calculates the height of the gap h_{lam}, from which on the flow becomes laminar.

$$h_{lam} = \frac{2000 * \eta(p,T)}{\rho * U} \tag{37}$$

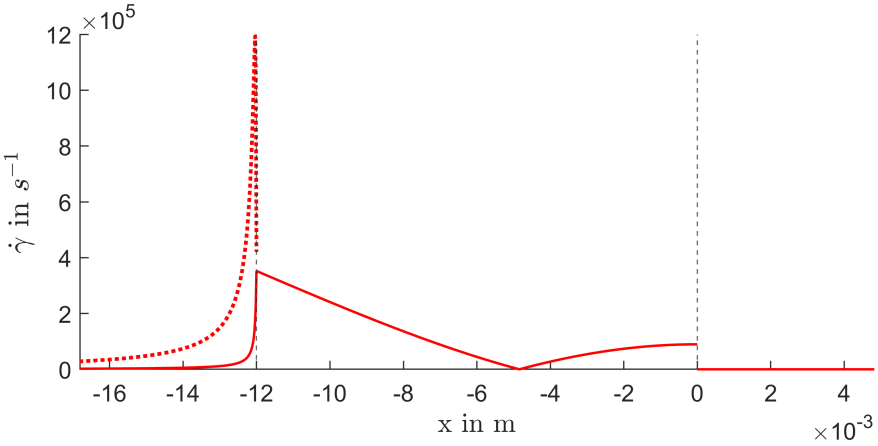

Figure 45: shear rate over rolling direction x, where the red solid line represents the shear rate as computed in subsection 4.6.1 and the dashed line in the inlet is the absolute mean shear rate computed by Trijssenaar.

Using this equation with a viscosity of $\eta(p,T) = 0.001\ Pas$, density of $\rho = 998\ kg/m^3$ and the entrainment speed of $U = 2.25\ m/s$, the calculated gap height from which the flow becomes laminar is $h_{lam} = 9 \times 10^{-4}\ m$, corresponding to the position of $x_{lam} \approx -12.46\ mm$. This indicates that there is no backflow from $x \approx -12.46\ mm$ onwards, which seems to be more realistic. With these numbers it is suggested that there is laminar flow before the peak as shown in Figure 45 computed by the absolute mean shear rate. Therefore it can This probably means that the shear rate in the inlet will not exceed the entry shear rate of $\dot{\gamma} = 3.5 \times 10^5\ s^{-1}$. However, it can be concluded that considering back flow in the inlet zone will result in a higher shear rate distribution.

5.3 The influence of entrainment speed on the limiting isothermal shear rate

This section discusses the anticipated effects of entrainment speed on the limiting isothermal shear rate. Followed by a subsection which elaborates the influence of entrainment speed on the limiting isothermal shear rate as found within the results of this thesis. Finally it analyses the cause of why the expectations do not match the obtained results.

5.3.1 Expectations

It is expected that the entrainment speed has an effect on the limiting isothermal shear rate. It is assumed that a higher entrainment speed causes more energy into the system, leading to increased heat generation or less heat dissipation. Consequently, the temperature in the contact will rise, resulting in viscous shear heating.

Increasing the entrainment speed by a certain factor, κ while keeping the SRR constant indicates that the sliding speed also increases by this factor κ.

$$SRR = \frac{u_s}{U} = \frac{\kappa\, u_s}{\kappa\, U} \tag{38}$$

The shear rate is defined as sliding speed defided by the film thickness. However the film thickness increases almost linear with the entrainment speed, which means that the film thickness is almost κ times as thick. This indicates that the shear rate remains unaffected with a higher entrainment

speed. Due to the unchanged shear rate, the shear stress also remains unaffected by an increase in entrainment speed.

$$\dot{\gamma} = \frac{u_s}{h} = \frac{\kappa\, u_s}{\kappa\, h} \tag{39}$$

The heat generation (HG) per unit square area per second is given by the product of the sliding speed and the shear stress [46]. This means that the heat generation per unit area per second increases by approximately the same factor κ as the entrainment speed.

$$HG = \tau\, u_s \rightarrow \tau\, \kappa\, u_s \tag{40}$$

However it can be said that the volume passing through the contact also increases by this factor κ and therefore the film has less time to heat up and more heat is lost. It is known that a part of the generated heat conducts through the contact area into the solids. The increased film thickness makes it more difficult for the generated heat to conduct through the surface. Therefore is is assumed that an increased entrainment speed causes viscous shear heating to occur sooner at a fixed shear rate. The expectation is in line with existing literature [62].

5.3.2 Outcome of experimental results and analysis

From experimental results it is shown that the entrainment speed has a negligible effect on the limiting isothermal shear rate. However existing literature indicates that entrainment speed does influence the occurrence of viscous shear heating. Liu et al. [62] reported that an increase in entrainment speed results in a bigger temperature rise due to less heat dissipation, which consequently lowers the limiting isothermal shear rate.

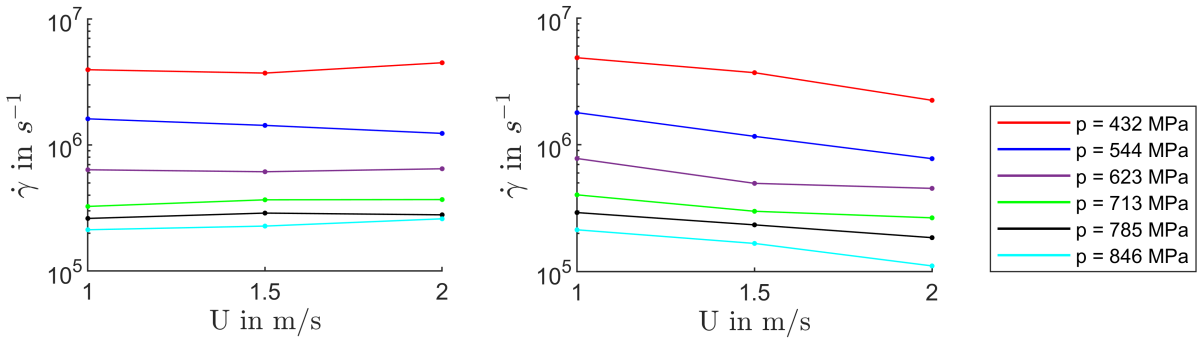

(a) Original computational approach (b) Alternative computational approach

Figure 46: Entrainment dependency on the limiting isothermal shear rate for different pressures at a temperature of $T = 40\ °C$.

Figure 46a shows the dependency of the three measured entrainment speeds on the limiting isothermal shear rate. Contrary to existing literature, no decrease in the limiting isothermal shear rate is observed with increasing entrainment speed.

This is probably due to the fact that the computational approach, as explained in chapter 3, fits every independent stress strain curve with an individual Eyring fit. This implies that the stress strain curves at different entrainment speeds are fitted independently within the approach used in this thesis.

An example of the stress strain curves under conditions of $T = 40\ °C$ and a mean pressure of $\overline{p} = 544\ MPa$ is shown in Figure 47. The computational approach calculates a different z value,

resulting in different viscosity, and Eyring stress τ_e for the different speeds. This means that the stress strain curves for one fixed temperature and pressure for multiple entrainment speeds exhibits slight variations in slope and potential shifts along the x-axis.

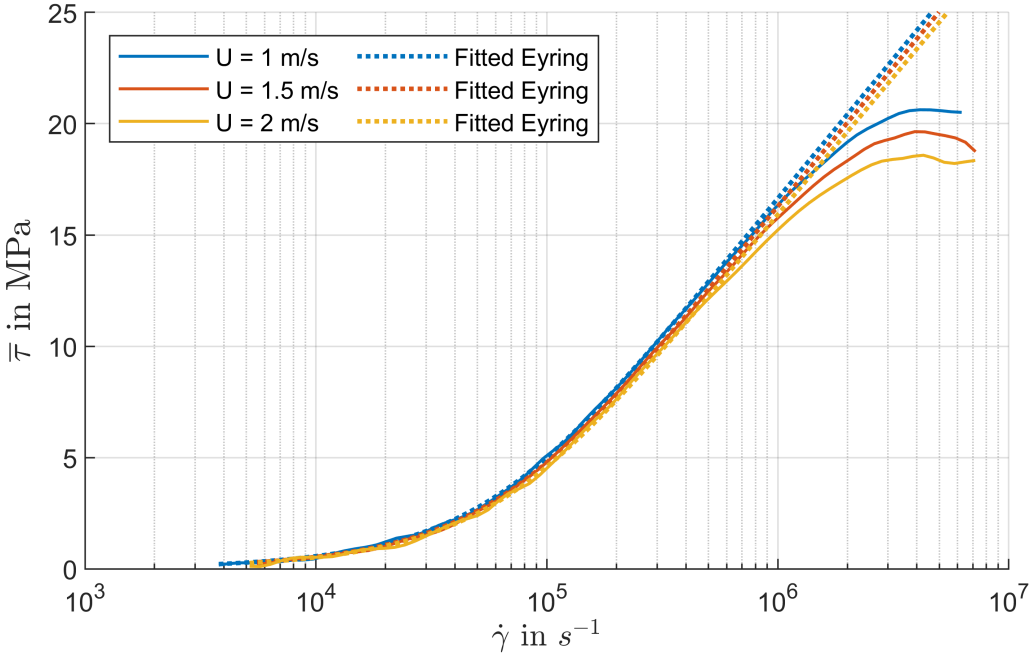

Figure 47: Stress strain curves at $\overline{p} = 544\ MPa$ and $T = 40\ °C$ for three different entrainment speeds. Each curve fitted with associated Eyring fit.

It can be discussed whether the used computational approach is correct. Theoretically, measurements conducted at a fixed mean pressure and temperature should result in equal values for z and the Eyring stress for different entrainment speeds. However, this was not observed in practice, as explained above.

One major downside of the experiments in combination with the computational approach is that it calculates the viscosity based on measured data. When doing a measurement at one fixed temperature, the computational approach calculates the viscosity based on this temperature in combination with the experimental results. However, during experiments it was noticed that temperature fluctuated within a deviation of $T \approx 1\ °C$. Under elevated pressures this slight difference in temperature could substantially affect the resulting stress strain curves.

For instance, the experiments as shown in Figure 47 were set at a fixed temperature of $T = 40\ °C$. The computed viscosity's for entrainment speeds of $U = [1\ 1.5\ 2]\ m/s$, were $\eta = [57.5\ 54.2\ 51.8]\ Pas$, respectively. Using the extended Roelands equation to compute the viscosity at a mean pressure of $\overline{p} = 544\ MPa$ and temperature of $T = 39\ °C$ and $T = 41\ °C$ result in viscosity of $\eta = 60\ Pas$ and $\eta = 51\ Pas$ respectively. These calculation suggest that the observed differences in values of z and τ_e across different entrainment speeds may result from small fluctuations in temperature while experimenting.

To account for this issue, an alternative computational approach is used to determine the limiting isothermal shear rate. Instead of fitting the Eyring model to each individual stress strain curve, the method involves averaging the z values, viscosity's and Eyring stresses. This allows a single Eyring fit across different entrainment speeds and is shown in Figure 48.

The same method is used to determine the limiting isothermal shear rate. When the deviation between the stress strain curves and the fitted Eyring model exceeds the specified tolerance,

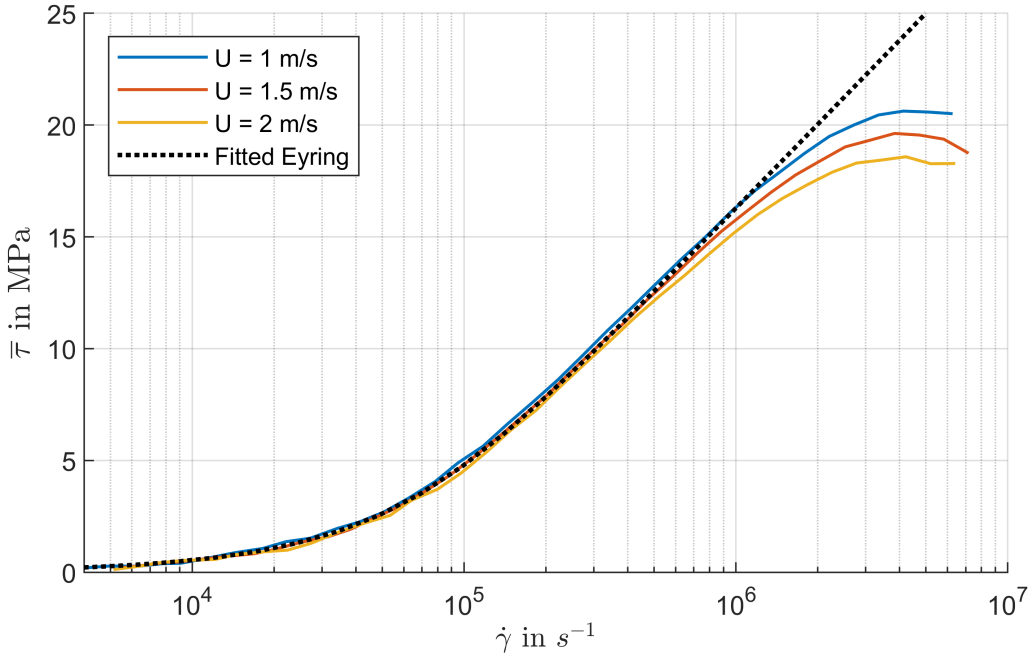

Figure 48: Stress strain curves at $\overline{p} = 544\ MPa$ and $T = 40\ °C$ for three different entrainment speeds, all fitted with the Eyring model computed with the average of the three parameters.

limiting isothermal shear rate is found. With this approach the limiting isothermal shear rate, and therefore the start of viscous shear heating, shows dependency on the entrainment speed. The relationship between limiting isothermal shear rate and the entrainment speed for this alternative approach is plotted in Figure 46b. An entrainment speed of $U = 2\ m/s$ consistently shows lower limiting isothermal shear rates than at an entrainment speed of $U = 1\ m/s$, which corresponds with existing literature [62].

To decide which method is preferred to determine the limiting isothermal shear rate is not straightforward. Correcting for different entrainment speeds using a single Eyring fit, as depicted in Figure 48, may be problematic due to minor variations in the experimental setup, such as the aforementioned temperature fluctuations. However if experiments are conducted under the exact same conditions, the original computational approach should give a consistent z value, viscosity and Eyring stress at a fixed pressure and temperature across various entrainment speeds. It can be argued that, under more precise testing conditions, the original approach as shown in Figure 47, should compute results similar to those obtained using the alternative computational approach shown in Figure 48.

5.3.3 Impact on viscous shear heating within the cold rolling process

Considering the decrease in limiting isothermal shear rate with entrainment speed for the cold rolling process it definitely impacts the occurrence of viscous shear heating. According to the original approach, where entrainment speed does not affect the onset of viscous shear heating, it was concluded that viscous shear heating only occurs within the last stand of CM 11 and the last two stands of CM 12. However, considering the dependency on entrainment speed it is assumed that viscous shear heating occurs earlier in the cold mills. An estimation is that it occurs already in the third stand of CM 11. An accurate prediction can unfortunately not be made, as extrapolating the points from Figure 46b would provide misleading indications of the limiting isothermal shear rate at higher entrainment speeds. Additional data is required to make a more accurate approximation of the limiting isothermal shear rate at elevated entrainment speeds.

5.4 Assumption film thickness within the work zone

It is assumed that the film thickness in the work zone is equivalent to the surface roughness of the work roll $h = R_a$. This assumption is based on the fact that cold rolling operates within the mixed lubrication regime. As discussed in section 2.2, the mixed lubrication regime is characterized by a film thickness that is approximately of the same order as the surface roughness. However, considering a film thicknesses of $h = 0.9r_a$ and $h = 1.1r_a$ suggests that these values also fall within the mixed lubrication regime. It can be questioned whether the approximation $h = r_a$ is sufficiently accurate. A film thickness of $h = 0.9R_a$ results in higher maximum shear rates within the stands and assuming a film thickness of $h = 1.1R_a$ will lead to lower maximum shear rate within the stands. The impact of changing the assumption of the film thickness to the aforementioned values is shown in Figure 49. It can be stated that the occurrence of viscous shear heating in the stands remains unchanged.

The cold rolling process operates in the mixed lubrication regime and as stated in section 2.2, this regime is active within the film parameter range of $0.5 < \lambda < 3$. This suggests that the film thickness can fluctuate between $h = 0.5R_a$ and $h = 3R_a$. Figure 49c and Figure 49d show the entry shear rate of the cold mill stands at these conditions respectively.

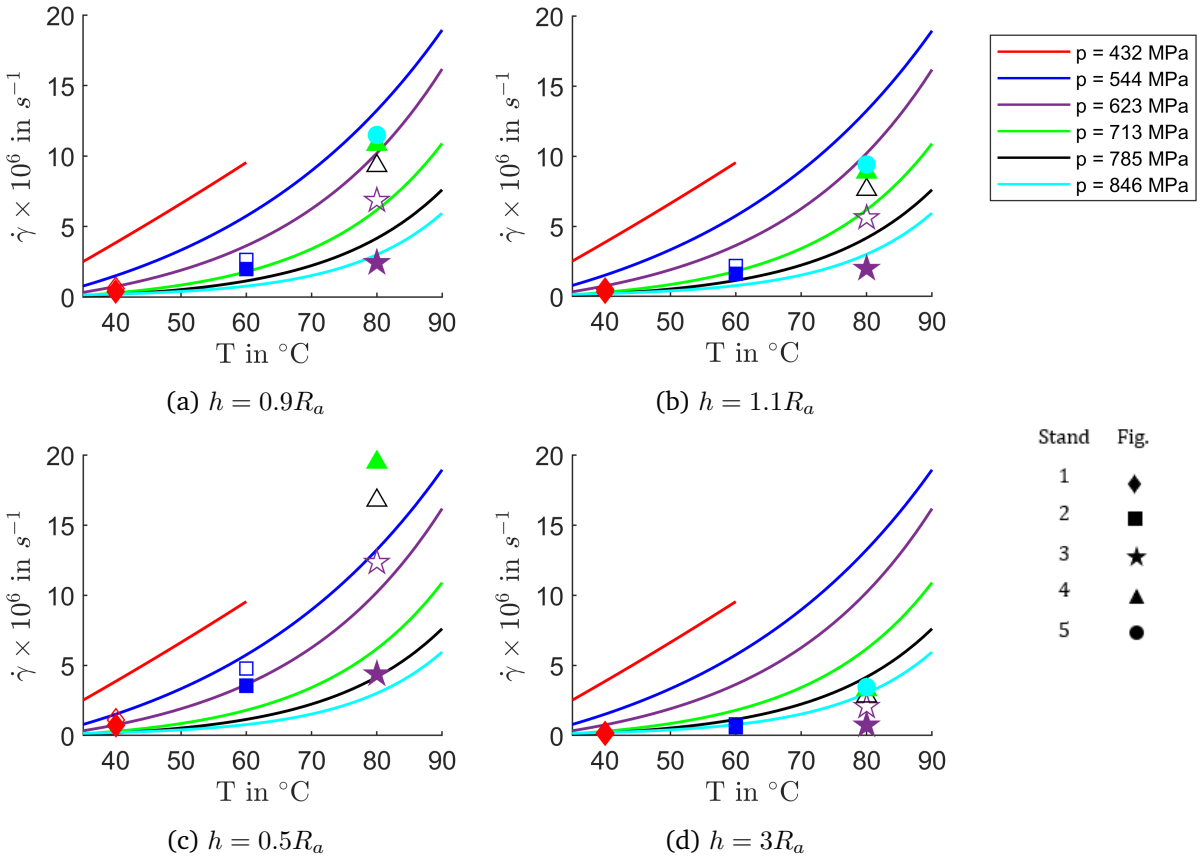

(a) $h = 0.9R_a$ (b) $h = 1.1R_a$

(c) $h = 0.5R_a$ (d) $h = 3R_a$

Figure 49: Entry shear rate of CM 11 (open) and CM 12 (solid) compared to the limiting isothermal shear rate for a different assumption of the film thickness.

When considering a film thickness equal to half the surface roughness ($h = 0.5R_a$), viscous shear heating occurs, beside the fourth stands in both cold mills and the last stand of CM 12, also in the third stand of CM 11. The entry shear rate in the third stand of CM 11, indicated by the open star in Figure 49c, is $\dot{\gamma} \approx 12.5 \times 10^6\ s^{-1}$ which exceeds the limiting isothermal shear rate of $\dot{\gamma} = 10 \times 10^6\ s^{-1}$. Considering a film thickness which is three times the surface roughness ($h = 3R_a$), the film thickness is relatively thick, which results in a decrease in shear rate in the

cold mills. This effect can be seen in Figure 49d. Almost all entry shear rates of the stands remain below the limiting isothermal shear rate, except for the last stand of CM 12. The entry shear rate of this stand exceeds the limiting isothermal shear rate barely and therefore small signs of viscous shear heating may occur in this stand.

Another assumption concerning the film thickness is that the film thickness is constant over the rolling direction in the work zone. However, it is known from theory [6, 19] that this is not the case. As illustrated in Figure 12, the real contact area within the work zone increases along the rolling direction, indicating a decrease in film thickness. This is in line with existing equations for the film thickness over the work zone as provided by Cuperus [19].

$$h(x) = h_0 \left(\frac{u_{roll} + u_{entry}}{u_{roll} + u_{strip}(x)} \right) \tag{41}$$

Where h_0 is the film thickness at the entry, u_{roll} is the velocity of the work roll, u_{entry} the velocity of the strip at the entry of the roll bite and $u_{strip}(x)$ the changing velocity of the strip within the work zone.

Considering the decreasing film thickness, as described in the equation above, the maximum shear rate within the stands exhibits only slight variations. It is noteworthy that the film thickness at the entry where the shear rate is at its maximum in the work zone, remains unchanged. Figure 50 shows the shear rate with decreasing film thickness (dashed line) over the rolling direction, in comparison to the constant film thickness indicated by the solid line. This comparison shows that the assumption of a constant film thickness across the work zone is justified, for the purposes of this thesis.

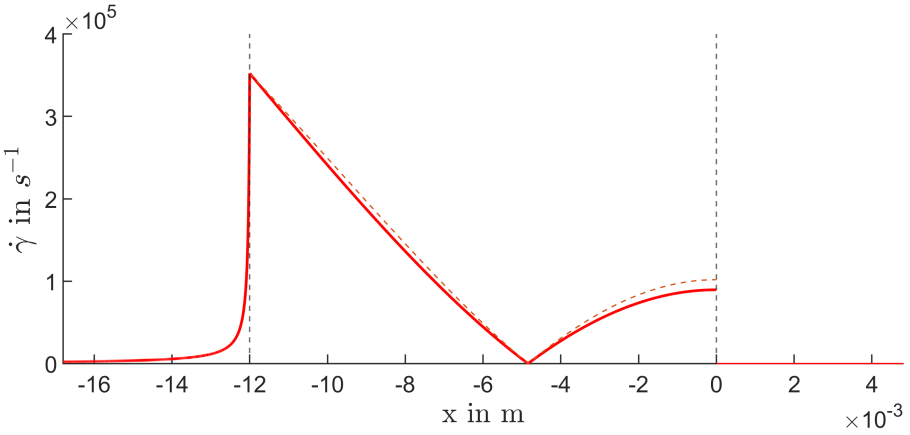

Figure 50: shear rate in the lubricant of stand 1 over rolling direction x with constant film thickness (solid line) and varying film thickness (dashed red line). Vertical dashed lines indicates the boundaries of the work zone.

6 Conclusion

This thesis investigated whether the occurrence of viscous shear heating, within the cold rolling process, has to be taken into account in friction models. The main research question was: "*Under which conditions can viscous shear heating be expected within a cold rolling tandem mill?*"

Ball-on-disc experiments were conducted to study the behavior of the lubricant in an EHL contact. The investigated lubricant exhibits non-Newtonian behavior in the form of shear thinning, which can be modelled by using the Eyring formulation. At a certain shear rate, the heat generation due to internal friction becomes that significant, that thermal effects begin to play a role. The heat generated within the lubricant reduces its viscosity, leading to a decrease in shear stress. The Eyring model is no longer applicable when this phenomena occurs and therefore the determination whether this aspect occurs within the cold rolling process is necessary.

A critical aspect of this study is the influence of pressure, temperature, and entrainment speed on viscous shear heating. The results from ball-on-disc experiments indicated that the occurrence of viscous shear heating is influenced by pressure and temperature. Specifically, an increase in pressure or a decrease in temperature causes viscous shear heating to occur at lower shear rates. Although the results showed that entrainment speed did not directly affect the occurrence of viscous shear heating, it is expected that higher entrainment speeds dissipate less heat into the solid at contact, causing a higher temperature rise, which subsequently leads to viscous shear heating occurring at lower shear rates.

The appearance of viscous shear heating within the cold rolling process at standard cold mill operations is investigated. It is found that viscous shear heating will occur within the last stand of cold mill 11 and the last two stands of cold mill 12. In these stands, the pressure is relatively high due to hardening of the workpiece and the film thickness is relatively low due to decreased surface roughness parameters of the work roll. This finding highlights the necessity to incorporate viscous shear heating into mixed lubrication friction models to ensure accurate predictions. Neglecting viscous shear heating in friction models can result in overestimating the shear stress in the contact.

To reflect back on the main research question: Viscous shear heating can be expected in a stand of the cold mill when operating at high pressure and low temperature in combination with high sliding speed and low film thickness. The latter results in a high shear rate that can easily exceed the limiting isothermal shear rate of the lubricant.

7 Recommendations

To further investigate the understanding of viscous shear heating within the cold rolling process, it is recommended to perform experiments with a ball-on-disc set up, which allows testing at higher entrainment speeds. By measuring the effects of increased entrainment speeds, a deeper insight into the relationship between entrainment speed and viscous shear heating can be given. This will enable a more accurate prediction of viscous shear heating withing the cold rolling process.

To ensure the accuracy and consistency of test results, it is recommended to check the specimens more frequently in between tests. The specimens undergo wear and a wear track will be formed while testing. This wear track increases the surface roughness and a transition from full film to mixed lubrication will occur. This transition can significantly affect the experimental outcomes as asperities get into contact and not only the traction of the lubricant is measured. Therefore it is crucial to check the surface roughness of the specimens in between tests to determine if the tests will still be within the full film lubrication regime. If it is indicated that wear and increased surface roughness is detected, the specimens has to be replaced by a new set.

Another improvement that can be done while testing to enhance the accuracy and consistency of the outcomes is to implement better temperature control. Even small temperature fluctuations can have a significant impact at the end results, especially at lower temperatures. A minor change in temperature while testing can influence the accuracy of the limiting isothermal shear rate. Advanced temperature control can dismiss these errors and will lead to a better approximation of the limiting isothermal shear rate.

References

[1] R. Davies, T. Domanti, S. Paardekooper, and G. Wallace, *International Rolling Technology Course*. Industrial Automation Services Pty Ltd, 31 ed., 10 2007.

[2] P. Montmitonnet, L. Fourment, U. Ripert, Q. T. Ngo, and A. Ehrlacher, "State of the art in rolling process modelling," *BHM Berg- und Hüttenmännische Monatshefte*, vol. 161, 2016.

[3] C. Roberts, "Mechanical Principles of Rolling," *Iron and Steelmaker (I and SM)*, vol. 25, 1998.

[4] M. A. Mekicha, "Wear particles formation in cold rolling," 2021. Doctoral thesis, University of Twente, Enschede.

[5] K. F. Karhausen and H. Pawelski, "Mechanics and Friction in Metal Rolling," *Encyclopedia of Lubricants and Lubrication*, 2014.

[6] A. Azushima, *Tribology in sheet rolling technology*. Springer Link, 2016.

[7] T. v. Kármán, "8. Beitrag zur Theorie des Walzvorganges," *ZAMM - Journal of Applied Mathematics and Mechanics / Zeitschrift für Angewandte Mathematik und Mechanik*, vol. 5, pp. 139–141, 1925.

[8] D. Boemer, "Numerical Modeling of Friction in Lubricated Cold Rolling," 2020. Doctoral thesis, Université de Liège, Liège.

[9] Y. J. Liu, A. K. Tieu, D. D. Wang, and W. Y. Yuen, "Friction Measurement in Cold Rolling," *Journal of Materials Processing Technology*, vol. 111, 2001.

[10] M. Laugier, M. Tornicelli, C. S. Leligois, D. Bouquegneau, D. Launet, and J. A. Alvarez, "Flexible Lubrication Concept. The future of Cold Rolling Lubrication," *Journal of Engineering Tribology*, vol. 225, pp. 949–958, 2011.

[11] R. Guillaument, S. Vincent, J. P. Caltagirone, M. Laugier, and P. Gardin, "Plate-out Modelling for Cold-Rolling Systems Lubricated with Oil-in-Water Emulsions," *Journal of Engineering Tribology*, vol. 225, pp. 905–914, 2011.

[12] O. Reynolds, "On the Theory of Lubrication and its Application," *Philosophical Transactions of Royal Society of London A*, vol. 177, 1886.

[13] L. Jacobs, J. van der Lugt, and M. de Rooij, "Contribution of Viscous Shear to Friction in Cold Rolling of Low-Carbon Steel," *Tribology International*, 2023.

[14] N. Marsault, "Modélisation du Régime de Lubrification Mixte en Laminage à Froid," 1998. Doctoral thesis, l'École des Mines de Paris, Paris.

[15] Z. L. Qiu, W. Y. Yuen, and A. K. Tieu, "Mixed-Film Lubrication Theory and Tension Effects on Metal Rolling Processes," *Journal of Tribology*, vol. 121, 1999.

[16] W. Wilson and J. Walowit, "An Isothermal Hydrodynamic Lubrication Rheory for Strip Rolling with Front and Back Tension," *Tribology Convention*, vol. 9, pp. 169–172, 1971.

[17] K. Saeki and Y. Hashimoto, "On the Oil Film Thickness in Cold Rolling of Thin Plate," *Japan Society Technology*, 1967.

[18] A. Azushima, "Determination of Oil Film Thickness in Rolling from the Relationship between Surface Roughness of Strip and Roll," *Bull JSME*, vol. 21, 1978.

[19] R. Cuperus, W. ten Napel, W. Neumann, and R. Smits, "Measurements of Film Thickness and Friction in Cold Rolling," *Proceedings of the 5th International Tribology Conference*, pp. 549–554, 1998.

[20] D. Zhu, G. Biresaw, S. J. Clark, and T. J. Kasun, "Elastohydrodynamic Lubrication With O/W Emulsions," *Journal of Tribology*, vol. 116, 1994.

[21] S. Cassarini, "Modélisation du Film Lubrifiant dans la Zone d'Entrée, pour la Lubrification par Émulsion en Laminage à Froid," *École Nationale Supérieure des Mines de Paris*, 2007. Doctoral thesis, l'École des Mines de Paris, Paris.

[22] L. J. Jacobs, K. N. Dam, D. J. Wentink, M. B. Rooij, J. van der Lugt, D. J. Schipper, and J. P. Hoefnagels, "Effect of Asymmetric Material Entrance on Lubrication in Cold Rolling," *Tribology International*, vol. 175, 2022.

[23] Y. H. Tsao and L. B. Sargent, "A mixed Lubrication Model for Cold Rolling of Metals," *ASLE Transactions*, vol. 20, 1977.

[24] J. Hitchcock, "Elastic Deformation of Rolls During Cold-Rolling," *A.S.M.E Special research committee on heavy-duty anti-friction bearings*, 1935.

[25] D. Bland and H. Ford, "The Calculation of Roll Force and Torque in Cold Strip Rolling with Tensions," *Proceedings of the Institution of Mechanical Engineers*, vol. 159, pp. 144–163, 1948.

[26] D. Jortner, J. F. Osterle, and C. F. Zorowski, "An Analysis of Cold Strip Rolling," *International Journal of Mechanical Sciences*, vol. 2, pp. 179–194, 1960.

[27] K. Hokkirigawa and K. Kato, "An Experimental and Theoretical Investigation of Ploughing, Cutting and Wedge Formation During Abrasive Wear," *Tribology International*, vol. 21, pp. 51–57, 2 1988.

[28] Z. Y. Zang and X. A. Han, "Study on Boundary Lubrication of Cold Rolling Oil," *Lubrication Engineering*, vol. 47, pp. 823–829, 10 1991.

[29] W. R. Wilson, Y. Sakaguchi, and S. R. Schmid, "A Mixed Flow Model for Lubrication with Emulsions," *Tribology Transactions*, vol. 37, 1994.

[30] P. E. Tabary, M. P. Sutcliffe, F. Porral, and P. Deneuvi, "Measurements of friction in cold metal rolling," *Journal of Tribology*, vol. 118, 1996.

[31] B. Bhushan, "Introduction to Tribology," *Introduction to Tribology, Second Edition*, 2013. Doctoral thesis, Ohio State University, Columbus.

[32] R. Boman and J. P. Ponthot, "Numerical simulation of lubricated contact in rolling processes," *Journal of Materials Processing Technology*, vol. 125, pp. 405–411, 2002.

[33] Y. Carretta, "Modélisation des Conditions d'Apparition du Micro-Hydrodynamisme via la Méthode des Éléments Finis dans la Perspective d'Intégrer ce Phénomène dans un Modèle Numérique de Laminage à Froid," 2014. Doctoral thesis, Université de Liège, Liège.

[34] A. Stephany, "Contribution à l'Étude Numérique de la Lubrification en Régime Mixte en Laminage," vol. 304, 2008. Doctoral thesis, Université de Liège, Liège.

[35] P. M. Lugt, "Lubrication in Cold Rolling: Numerical Simulation using Multigrid Techniques," 1992. Doctoral thesis, University of Twente, Enschede.

[36] K. L. Johnson, "Regimes of Elastohydrodynamic Lubrication," *Journal of Mechanical Engineering Science*, vol. 12, 1970.

[37] S. Bair, "High Pressure Rheology for Quantitive Elastohydrodynamics," 2019. Doctoral thesis, Georgia Institute of Technology, Atlanta.

[38] A. Ertel, "Hydrodynamic Lubrication Based on New Principles," *Akad. Nauk SSSR Prikadnaya Mathematica i Mekhanika*, vol. 3, pp. 41–52, 1939.

[39] F. Sadeghi, "6 - Elastohydrodynamic Lubrication," *Tribology and Dynamics of Engine and Powertrain*, pp. 171–221, 2010.

[40] H. Moes, "Lubrication and Beyond," *University of Twente lecture notes*, 2000.

[41] A. N. Grubin, I. E. Vinogradova, and K. F. Ketova, "Investigation of the Contact of Machine Components," *Central Scientific Research Inst. Tech. Mech. Eng.*, 1949.

[42] D. Dowson and G. R. Higginson, "A Numerical Solution to the Elasto-Hydrodynamic Problem," *Journal of Mechanical Engineering Science*, vol. 1, 1959.

[43] A. W. Crook, "The Lubrication of Rollers II. Film Thickness with Relation to Viscosity and Speed," *Philosophical Transactions of the Royal Society of London. Series A, Mathematical and Physical Sciences*, vol. 254, pp. 223–236, 12 1961.

[44] R. Gohar and A. Cameron, "Optical Measurement of Oil Film Thickness under Elastohydrodynamic Lubrication," *Nature*, vol. 200, pp. 458–459, 1963.

[45] J. Zhao, F. Sadeghi, and M. H. Hoeprich, "Analysis of EHL Circular Contact Start Up: Part I—Mixed Contact Model With Pressure and Film Thickness Results," *Journal of Tribology*, vol. 123, 2001.

[46] H. Spikes, "Basics of EHL for Practical Application," *Lubrication Science*, vol. 27, 2015.

[47] C. Barus, "Isothermals, Isopiestics and Isometrics Relative to Viscosity," *American Journal of Science*, 1893.

[48] L. E. Murch and W. R. D. Wilson, "A Thermal Elastohydrodynamic Inlet Zone Analysis," *Journall of Lubrication Technology*, vol. 97, pp. 212–216, 1975.

[49] C. J. A. Roelands, W. O. Winer, and W. A. Wright, "Correlational aspects of the viscosity-temperature-pressure relationship of lubricating oils," *Journal of Lubrication Technology*, vol. 93, 1971.

[50] S. Bair, "The Unresolved Definition of the Pressure-Viscosity Coefficient," *Scientific Reports*, vol. 12, 2022.

[51] D. Frisch, H. Eyring, and J. F. Kincaid, "Pressure and Temperature Effects on the Viscosity of Liquids," *Journal of Applied Physics*, vol. 11, 1940.

[52] M. Shirzadegan, R. Larsson, and A. Almqvist, "A Low Degree of Freedom Approach for Prediction of Friction in Finite EHL Line Contacts," *Tribology International*, vol. 115, 2017.

[53] H. S. Cheng and B. Sternlicht, "A Numerical Solution for the Pressure, Temperature, and Film Thickness Between Two Infinitely Long, Lubricated Rolling and Sliding Cylinders, Under Heavy Loads," *Journal of Basic Engineering*, vol. 87, pp. 695–704, 1965.

[54] W. Habchi and P. Vergne, "On the Compressive Heating/Cooling Mechanism in Thermal Elastohydrodynamic Lubricated Contacts," *Tribology International*, vol. 88, pp. 143–152, 2015.

[55] T. Reddyhoff, H. A. Spikes, and A. V. Olver, "Compression Heating and Cooling in Elastohydrodynamic Contacts," *Tribology Letters*, vol. 36, pp. 69–80, 2009.

[56] R. Grieve and H. Spikes, "Temperature and Shear Stress in Thin Film EHD Contacts," *Tribology Series*, vol. 38, pp. 511–522, 2000.

[57] P. G. Goksem and R. A. Hargreaves, "The Effect of Viscous Shear Heating on Both Film Thickness and Rolling Traction in an EHL Line Contact - Part I: Fully Flooded Conditions," *Journal of Lubrication Technology*, vol. 100, pp. 346–352, 1978.

[58] W. R. D. Wilson and S. M. Mahdavian, "A thermal reynolds equation and its application in the analysis of plasto-hydrodynamic inlet zones," *Journal of Lubrication Technology*, vol. 96, pp. 572–577, 10 1974.

[59] "MTM - PCS Instruments," 2024. URL: https://pcs-instruments.com/product/mtm/, Date accessed: 10/02/2024.

[60] R. Poole, "The Deborah and Weissenberg numbers," *The British Society of Rheology - Rheology Bulletin*, vol. 53, pp. 32–39, 2012.

[61] H. Blok, "Inverse Problem in Hydrodynamic Lubrication and Design Directives for Lubricated Flexible Surfaces," *Engineering of Material Science*, 1963.

[62] H. C. Liu, B. B. Zhang, N. Bader, G. Poll, and C. H. Venner, "Influences of Solid and Lubricant Thermal Conductivity on Traction in an EHL Circular Contact," *Tribology International*, vol. 146, 2020.

[63] J. A. Greenwood and J. J. Kauzlarich, "Inlet Shear heating in Elastohydrodynamic Lubrication," *Journal of Lubrication Technology*, vol. 95, pp. 417–423, 1973.

[64] M. Trijssenaar, "Emulsion Lubrication in Cold Rolling," 2002. Doctoral thesis, TU Delft, Delft.

A MatLab Coding

A.1 Traction curves

```
clear, clc, close all, warning off
disp('LETS DO THIS :) AND REMEMBER, YOU CAN NOT AFFORD THROWING YOUR LAPTOP OUT OF THE WINDOW, it is too expensive')

size_ball = "big";                          % 'big' , 'small'
Show = "Temp";                              % 'Temp', 'Press', 'Speed'

% Constant Initial parameters
E1 = 2.07*10^11;                            % Youngs modulus of the ball (Pa)
E2 = 2.07*10^11;                            % Youngs modulus of the disk (Pa)
mu1 = 0.29;                                 % Poissons ratio of ball (-)
mu2 = 0.29;                                 % Poissons ratio of ring (-)
E_ = 2/(((1-mu1^2)/E1)+((1-mu2^2)/E2));     % Combined youngs modulus E' (Pa)

names = {};
colors = ['r','b','m','g','k',"#7E2F8E","#EDB120","#A2142F"];

if size_ball == "big"

    R_x = 0.01905/2;                        % Ball radius (m)

    % Load data from the data file
    load('SRR.mat'); load('TractionCoeff.mat'); load('RollingSpeed.mat'); load('SlidingSpeed.mat'); load('TractionForce.mat');

    numFields = numel(fieldnames(SRR));

    % Testing range
    T = [40:10:90,110,130];                 % Temperature (C)
    W = 30:15:75;                           % Normal load (N)
    U = [2,1.5,1];                          % Entrainment speed (m/s)

    if Show == "Temp"

        for i = 1:length(T)

            figure(i), hold on
            title(['Traction curve for T = ',num2str(T(i)),' (C)']);
```

```
37              xlabel('SRR (%)'), ylabel('CoF (-)')
38              grid on
39
40              for j = 1:length(W)
41
42                  % Hertzian contact radius
43                  r_a = ((3*R_x*W(j))/(2*E_))^(1/3);
44
45                  % Pressure p in N/m^2
46                  p = W(j)/(pi*r_a^2);
47
48                  for k = 1:length(U)
49
50                      if k == 2
51                          name = sprintf('Step_%dN_%dC_%d', W(j), T(i)
                                , U(k)*10);
52                      else
53                          name = sprintf('Step_%dN_%dC_%d', W(j), T(i)
                                , U(k));
54                      end
55
56                      names = [names, name];
57
58                      figure(i)
59                      if k == 1
60                          plot(SRR.(name), TractionCoeff.(name), Color
                               =colors(j),LineWidth=1)
61                      elseif k == 2
62                          plot(SRR.(name), TractionCoeff.(name), "--",
                               Color=colors(j),LineWidth=1)
63                      else
64                          plot(SRR.(name), TractionCoeff.(name), ":",
                               Color=colors(j),LineWidth=1.5)
65                      end
66
67                      names_plot = erase(names,'Step');
68                      names_plot = replace(names_plot,'_',' ');
69                      names_plot = replace(names_plot,[num2str(T(i)),'
                            C'],' ');
70                      names_plot = replace(names_plot,'15','1.5');
71                      names_plot = strcat(names_plot, ' m/s');
72
73                  end
74              end
75
76              legend(erase(names_plot((i-1)*(length(U)*length(W)) + 1:
                    end),'_'),'Orientation', 'horizontal', 'Location', '
                    southoutside','NumColumns', 3);
77              fig = gcf;
78              fig.Position = [300, 300, 700, 500];
79              hold off
```

```
80
81          end
82
83      elseif Show == "Press"
84
85          for i = 1:length(W)
86
87              figure(i), hold on
88              title(['Traction curve for W = ',num2str(W(i)),' (N)']);
89              xlabel('SRR (%)'), ylabel('CoF (-)')
90              grid on
91
92              for j = 1:length(T)
93
94                  % Hertzian contact radius
95                  r_a = ((3*R_x*W(i))/(2*E_))^(1/3);
96
97                  % Pressure p in N/m^2
98                  p = W(i)/(pi*r_a^2);
99
100                 for k = 1:length(U)
101
102                     if k == 2
103                         name = sprintf('Step_%dN_%dC_%d', W(i), T(j)
                                , U(k)*10);
104                     else
105                         name = sprintf('Step_%dN_%dC_%d', W(i), T(j)
                                , U(k));
106                     end
107
108                     names = [names, name];
109
110                     figure(i)
111                     if k == 1
112                         plot(SRR.(name), TractionCoeff.(name),Color=
                                colors(j),LineWidth=1)
113                     elseif k == 2
114                         plot(SRR.(name), TractionCoeff.(name), "--",
                                Color=colors(j),LineWidth=1)
115                     else
116                         plot(SRR.(name), TractionCoeff.(name), ":",
                                Color=colors(j),LineWidth=1.5)
117                     end
118
119                     names_plot = erase(names,'Step');
120                     names_plot = replace(names_plot,'_',' ');
121                     names_plot = replace(names_plot,[num2str(W(i)),'
                            N'],' ');
122                     names_plot = replace(names_plot,'15','1.5');
123                     names_plot = strcat(names_plot, ' m/s');
124
```

```
125                 end
126             end
127
128             legend(names_plot((i-1)*(length(U)*length(T)) + 1:end),'
                    Orientation', 'horizontal', 'Location', 'southoutside
                    ','NumColumns', 3)
129             fig = gcf;
130             fig.Position = [300, 300, 700, 500];
131             hold off
132         end
133
134     elseif Show == "Speed"
135
136         for i = 1:length(U)
137
138             figure(i), hold on
139             title(['Traction curve for U = ',num2str(U(i)),' (m/s)'
                    ]);
140             xlabel('SRR (%)'), ylabel('CoF (-)')
141             grid on
142
143             for j = 1:length(W)
144
145                 % Hertzian contact radius
146                 r_a = ((3*R_x*W(j))/(2*E_))^(1/3);
147
148                 % Pressure p in N/m^2
149                 p = W(j)/(pi*r_a^2);
150
151                 for k = 1:length(T)
152
153                     if i == 2
154                         name = sprintf('Step_%dN_%dC_%d', W(j), T(k)
                                , U(i)*10);
155                     else
156                         name = sprintf('Step_%dN_%dC_%d', W(j), T(k)
                                , U(i));
157                     end
158
159                     names = [names, name];
160
161                     figure(i)
162                     if j == 1
163                         plot(SRR.(name), TractionCoeff.(name),Color=
                                colors(k),LineWidth=1)
164                     elseif j == 2
165                         plot(SRR.(name), TractionCoeff.(name), "--",
                                Color=colors(k),LineWidth=1)
166                     elseif j == 3
167                         plot(SRR.(name), TractionCoeff.(name), "-.",
                                Color=colors(k),LineWidth=1)
```

```
168                         else
169                             plot(SRR.(name), TractionCoeff.(name), ":",
                                    Color=colors(k),LineWidth=1.5)
170                         end
171
172                         names_plot = erase(names,'Step');
173                         names_plot = replace(names_plot,'_',' ');
174                         names_plot = replace(names_plot,'15','1.5');
175                         names_plot = replace(names_plot,['C ',num2str(U(
                                i))],'C');
176                     end
177                 end
178
179                 legend(erase(names_plot((i-1)*(length(T)*length(W)) + 1:
                        end),'_'),'Orientation', 'horizontal', 'Location', '
                        southoutside','NumColumns', 8)
180                 fig = gcf;
181                 fig.Position = [300, 300, 700, 500];
182                 hold off
183
184             end
185
186         else
187             disp('Put in Temp, Press, or Speed for Show')
188         end
189
190 elseif size_ball == "small"
191
192     R_x = 0.00635;
193
194     % Load data from the data file
195     load('SRR_small.mat'); load('TractionCoeff_small.mat'); load('
            RollingSpeed_small.mat'); load('SlidingSpeed_small.mat');
            load('TractionForce_small.mat');
196
197     numFields = numel(fieldnames(SRR_small));
198
199     % Testing range
200     T = 40:10:90;                       % Temperature
                                (C)
201     W = 45:15:75;                       % Normal load
                                (N)
202     U = [1.5,1];                        % Entrainment speed
                            (m/s)
203
204     if Show == "Temp"
205
206         for i = 1:length(T)
207
208             figure(i), hold on
209             title(['Traction curve for T = ',num2str(T(i)),' (C)']);
```

```
210             xlabel('SRR (%)'), ylabel('CoF (-)')
211             grid on
212 
213             for j = 1:length(W)
214 
215                 % Hertzian contact radius
216                 r_a = ((3*R_x*W(j))/(2*E_))^(1/3);
217 
218                 % Pressure p in N/m^2
219                 p = W(j)/(pi*r_a^2);
220 
221                 for k = 1:length(U)
222 
223                     if k == 1
224                         name = sprintf('Step_%dN_%dC_%d', W(j), T(i)
                                , U(k)*10);
225                     else
226                         name = sprintf('Step_%dN_%dC_%d', W(j), T(i)
                                , U(k));
227                     end
228 
229                     names = [names, name];
230 
231                     figure(i)
232                     if k == 1
233                         plot(SRR_small.(name), TractionCoeff_small.(
                               name), Color=colors(j),LineWidth=1)
234                     elseif k == 2
235                         plot(SRR_small.(name), TractionCoeff_small.(
                               name), "--",Color=colors(j),LineWidth=1)
236                     else
237                         plot(SRR_small.(name), TractionCoeff_small.(
                               name), ":",Color=colors(j),LineWidth=1.5)
238                     end
239 
240                     names_plot = erase(names,'Step');
241                     names_plot = replace(names_plot,'_',' ');
242                     names_plot = replace(names_plot,[num2str(T(i)),'
                           C'],' ');
243                     names_plot = replace(names_plot,'15','1.5');
244                     names_plot = strcat(names_plot, ' m/s');
245 
246                 end
247             end
248 
249             legend(erase(names_plot((i-1)*(length(U)*length(W)) + 1:
                   end),'_'),'Orientation', 'horizontal', 'Location', '
                   southoutside','NumColumns', 2);
250             fig = gcf;
251             fig.Position = [300, 300, 700, 500];
252             hold off
```

```
253
254         end
255
256     elseif Show == "Press"
257
258         for i = 1:length(W)
259
260             figure(i), hold on
261             title(['Traction curve for W = ',num2str(W(i)),' (N)']);
262             xlabel('SRR (%)'), ylabel('CoF (-)')
263             grid on
264
265             for j = 1:length(T)
266
267                 % Hertzian contact radius
268                 r_a = ((3*R_x*W(i))/(2*E_))^(1/3);
269
270                 % Pressure p in N/m^2
271                 p = W(i)/(pi*r_a^2);
272
273                 for k = 1:length(U)
274
275                     if k == 1
276                         name = sprintf('Step_%dN_%dC_%d', W(i), T(j)
                                , U(k)*10);
277                     else
278                         name = sprintf('Step_%dN_%dC_%d', W(i), T(j)
                                , U(k));
279                     end
280
281                     names = [names, name];
282
283                     figure(i)
284                     if k == 1
285                         plot(SRR_small.(name), TractionCoeff_small.(
                                name),Color=colors(j),LineWidth=1)
286                     elseif k == 2
287                         plot(SRR_small.(name), TractionCoeff_small.(
                                name), "--",Color=colors(j),LineWidth=1)
288                     else
289                         plot(SRR_small.(name), TractionCoeff_small.(
                                name), ":",Color=colors(j),LineWidth=1.5)
290                     end
291
292                     names_plot = erase(names,'Step');
293                     names_plot = replace(names_plot,'_',' ');
294                     names_plot = replace(names_plot,[num2str(W(i)),'
                            N'],' ');
295                     names_plot = replace(names_plot,'15','1.5');
296                     names_plot = strcat(names_plot, ' m/s');
297
```

```
298                 end
299             end
300
301             legend(names_plot((i-1)*(length(U)*length(T)) + 1:end),'
                    Orientation', 'horizontal', 'Location', 'southoutside
                    ','NumColumns', 2)
302             fig = gcf;
303             fig.Position = [300, 300, 700, 500];
304             hold off
305         end
306
307     elseif Show == "Speed"
308
309         for i = 1:length(U)
310
311             figure(i), hold on
312             title(['Traction curve for U = ',num2str(U(i)),' (m/s)'
                    ]);
313             xlabel('SRR (%)'), ylabel('CoF (-)')
314             grid on
315
316             for j = 1:length(W)
317
318                 % Hertzian contact radius
319                 r_a = ((3*R_x*W(j))/(2*E_))^(1/3);
320
321                 % Pressure p in N/m^2
322                 p = W(j)/(pi*r_a^2);
323
324                 for k = 1:length(T)
325
326                     if i == 1
327                         name = sprintf('Step_%dN_%dC_%d', W(j), T(k)
                                , U(i)*10);
328                     else
329                         name = sprintf('Step_%dN_%dC_%d', W(j), T(k)
                                , U(i));
330                     end
331
332                     names = [names, name];
333
334                     figure(i)
335                     if j == 1
336                         plot(SRR_small.(name), TractionCoeff_small.(
                                name),Color=colors(k),LineWidth=1)
337                     elseif j == 2
338                         plot(SRR_small.(name), TractionCoeff_small.(
                                name), "--",Color=colors(k),LineWidth=1)
339                     elseif j == 3
340                         plot(SRR_small.(name), TractionCoeff_small.(
                                name), "-.",Color=colors(k),LineWidth=1)
```

```
341                         else
342                             plot(SRR_small.(name), TractionCoeff_small.(
                                    name), ":",Color=colors(k),LineWidth=1.5)
343                         end
344
345                         names_plot = erase(names,'Step');
346                         names_plot = replace(names_plot,'_',' ');
347                         names_plot = replace(names_plot,'15','1.5');
348                         names_plot = replace(names_plot,['C ',num2str(U(
                                i))],'C');
349                     end
350                 end
351
352                 legend(erase(names_plot((i-1)*(length(T)*length(W)) + 1:
                        end),'_'),'Orientation', 'horizontal', 'Location', '
                        southoutside','NumColumns', 6)
353                 fig = gcf;
354                 fig.Position = [300, 300, 700, 500];
355                 hold off
356
357             end
358
359         else
360             disp('Put in Temp, Press, or Speed for Show')
361         end
362
363 else
364     disp('Put in big or small for size_ball')
365 end
```

A.2 Computational approach

A.2.1 Part I

```
clear, clc, warning off, close all

% Which speed has to be analysed:
U_entrain = 2;                                  % Analysing entrainment
    speed    (m/s)

fric_min = 0.001;

% Constant Initial parameters
E1 = 2.07*10^11;                                % Youngs modulus of the ball
        (Pa)
E2 = 2.07*10^11;                                % Youngs modulus of the disk
        (Pa)
mu1 = 0.29;                                     % Poissons ratio of ball
            (-)
mu2 = 0.29;                                     % Poissons ratio of ring
            (-)
E_ = 2/(((1-mu1^2)/E1)+((1-mu2^2)/E2));         % Combined youngs modulus E'
        (Pa)

folder          = 'C:\Users\lieke\OneDrive\Documenten\UT\Afstuderen\
    MATLAB_TEST_FILES\';
file            = 'Raw_data';

[num,txt,raw]   = xlsread([folder file],[num2str(U_entrain),'mps']);

nsub = 4;
nraw = floor((size(raw,2)+1)/nsub);

for j = 1:nraw

    selnnan=min(~isnan(num(:,(j-1)*nsub+(1:3))),[],2);
    selnnan(1)=false;
    eval(['x' num2str(1) '1=num(1,(j-1)*nsub+1);']); % T
    eval(['x' num2str(1) '2=num(1,(j-1)*nsub+2);']); % W
    eval(['x' num2str(1) '3=num(1,(j-1)*nsub+3);']); % U
    eval(['y' num2str(1) '1=num(2,(j-1)*nsub+1);']); % R_x

    if      x12==10 stress_max = 10e6;
    elseif x12==20 stress_max = 12.5e6;
    elseif x12==30 stress_max = 17.5e6;
    elseif (x12==45) && (y11==0.009525) stress_max = 20e6;
    elseif (x12==60) && (y11==0.009525) stress_max = 22.5e6;
    elseif (x12==75) && (y11==0.009525) stress_max = 25e6;
    elseif (x12==45) && (y11==0.00635) stress_max = 30e6;
    elseif (x12==60) && (y11==0.00635) stress_max = 32.5e6;
    elseif (x12==75) && (y11==0.00635) stress_max = 35e6;
    else    disp('Load not found')
```

```
42      end
43
44      a_H = ((3*x12*y11)/(2*E_))^(1/3);
45      fric_max = stress_max * pi * a_H^2;
46
47      sely = num(:,(j-1)*nsub+3) > fric_min & num(:,(j-1)*nsub+3) <
            fric_max;
48
49      eval(['y' num2str(1) '2=num(selnnan & sely,(j-1)*nsub+2);']);
50      eval(['y' num2str(1) '3=num(selnnan & sely,(j-1)*nsub+3);']);
51
52      x0 = [0.5 , 7];     % Initial guess for z and tau_e value
53      x = fminsearch(@f_EHL_otherspeeds,x0);
54
55      result_h(j) = h_moes;
56      result_z(j) = x(1);
57      result_eta(j) = Eta;
58      result_tau(j) = x(2);
59      result_alpha_star(j) = alpha_a;
60      result_lsq(j) = lsqsum;
61      result_lambda(j) = lambda;
62      result_r_a(j) = r_a;
63      result_T(j) = x11;
64      result_W(j) = x12;
65      result_avspeed(j) = x13;
66
67  end
68
69  file = 'Results data fitting.xlsm';
70  [suc,msg] = xlswrite([folder file],[result_T',result_W',
        result_avspeed',result_z', result_alpha_star', result_eta',
        result_tau', result_h',result_lambda',result_r_a'] ,['Real values
         ',num2str(U_entrain),'mps'], 'A2' );
71
72
73  disp(['Results are in file: ',file])
```

A.2.2 Part II

```
function f = f_EHL_otherspeeds(x)

% Initial parameters
E1 = 2.07*10^11;                                % Youngs modulus of the ball
        (Pa)
E2 = 2.07*10^11;                                % Youngs modulus of the disk
        (Pa)
mu1 = 0.29;                                     % Poissons ratio of ball
           (-)
mu2 = 0.29;                                     % Poissons ratio of ring
           (-)
E_ = 2/(((1-mu1^2)/E1)+((1-mu2^2)/E2));         % Combined youngs modulus E'
        (Pa)


s = 1.0014;                                     % Material parameter
                (-)
Eta_s = 0.03657;                                % Kinematic viscosity
    datasheet (Pa s)
p_s = 0;                                        % Zero gauge pressure
               (Pa)
T_s = 40;                                       % Base temperature
                  (C)
p_0 = -0.2*10^(9);                              % Universal parameter
               (Pa)
T_0 = -135;                                     % Universal parameter
               (C)
p_atm = 101325;                                 % Athmospheric pressure
             (Pa)
R_q_ball = 0.029e-06;                           % Surface roughness ball/
    disc    (m)
R_q_disc = 0.009e-06;

% optimization parameters
z_R=x(1);
tau_e=x(2)*1e6;

% read parameters specifying the experiment
T               = evalin('base', ['x11;']);
W               = evalin('base', ['x12;']);
avspeed         = evalin('base', ['x13;']);
R_x             = evalin('base', ['y11;']);
SlidingSpeed    = evalin('base', ['y12;']);
TractionForce   = evalin('base', ['y13;']);

% Define parameters related to the oil rheolgy
Eta_a = Eta_s * exp((log(Eta_s)+9.67)*(((p_atm-p_0)/(p_s-p_0))^z_R
    *((T_s-T_0)/(T-T_0))^s-1));
alpha_a = (log(Eta_a)+9.67) * z_R / abs(p_0);
alpha_star = alpha_a / (1+((1-z_R)/(alpha_a * abs(p_0))));
```

```
37
38 assignin('base', 'alpha_a', alpha_a );
39
40 % Film thickness with MOES formula
41 N = W/(E_*R_x^2) * ((E_*R_x)/(Eta_a*2*avspeed))^(3/4);
42 L = alpha_star * E_ * ((Eta_a*2*avspeed)/(E_*R_x))^(1/4);
43 H_RI = 145*(1.796^(-15/7))*(N^(-2));
44 H_EI = 3.18*(1.63^(-14/25))*(N^(-2/15));
45 H_RP = 1.29*(1.691^(-2/3))*(L^(2/3));
46 H_EP = 1.48*(1.63^(-7/20))*(N^(-1/12))*(L^(3/4));
47 s_moes = (3/2) * (1 + exp(-1.2 * (H_EI/H_RI) ) );
48 H_moes = (((H_RI^(3/2))+( H_EI^(-4) + 0.1)^(-3/8) )^(2*s_moes/3) + (
       H_RP^(-8) + H_EP^(-8) )^(-1*s_moes/8) )^(1/s_moes);
49 h_moes = R_x * ((E_*R_x)/(Eta_a*2*avspeed))^(-0.5) * H_moes;
50
51 assignin('base', 'h_moes', h_moes );
52
53 % Lambda value
54 lambda = h_moes / sqrt(R_q_ball^2+R_q_disc^2);
55
56 assignin('base', 'lambda', lambda);
57
58 % Hertzian contact conditions
59 r_a = ((3*R_x*W)/(2*E_))^(1/3);
60 p_mean = W/(pi*r_a^2);
61
62 assignin('base','r_a', r_a);
63
64 % Experimental shear rate and shear stress
65 ShearRate = (SlidingSpeed/1000)/h_moes;
66 ShearStress = TractionForce / (pi*r_a^2);
67
68 % Eyring fit of shear stress
69 Eta = Eta_s * exp((log(Eta_s)+9.67)*(((p_mean-p_0)/(p_s-p_0))^z_R*((
       T_s-T_0)/(T-T_0))^s-1));
70 fitshearstress = tau_e*asinh(ShearRate*Eta/tau_e);
71 diffshearstress = (fitshearstress - ShearStress);
72 lsqsum = sum(diffshearstress.^2);
73
74 assignin('base', 'Eta', Eta );
75 assignin('base', 'lsqsum', lsqsum );
76
77 f = lsqsum;
```

A.3 Starting point Viscous shear heating

```
clear, clc, warning off, close all

disp('LETS DO THIS :) AND REMEMBER, YOU CAN NOT AFFORD THROWING YOUR LAPTOP OUT OF THE WINDOW, it is too expensive')

U = [1,1.5,2];

% Tolerance of error from which thermal effects play a role
Tolerance = 1e6;

% Load data from the data file
load('SRR.mat'); load('TractionCoeff.mat'); load('RollingSpeed.mat'); load('SlidingSpeed.mat'); load('TractionForce.mat');
load('SRR_small.mat'); load('TractionCoeff_small.mat'); load('RollingSpeed_small.mat'); load('SlidingSpeed_small.mat'); load('TractionForce_small.mat');

folder  = 'C:\Users\lieke\OneDrive\Documenten\UT\Afstuderen\MATLAB_TEST_FILES\';
file    = 'Results data fitting.xlsm';

% Figure properties
colors = ['r','b',"#7E2F8E",'g','k','c','m',"#EDB120","#A2142F"];
legendLabels = {};
legendLabels2 = {};

% Graph for start of viscous shear heating
figure(9), hold on
title('Starting strain for viscous shear heating')
xlabel('Pressure (MPa)'), ylabel('ShearRate (s^{-1})')
xlim([400,1200]),ylim([10^5,2*10^7])
if length(U)==3
    annotation('textbox',[.78 .2 .12 .2],'String','__  1 m/s  -  -  1.5 m/s  2 m/s')
    title('Starting strain for viscous shear heating')
elseif length(U) == 1
    title(['Starting strain for viscous shear heating at U = ', num2str(U),' m/s'])
end
fig10 = gcf;
fig10.Position = [300, 300, 700, 350];

% Graph for Eyring stress
figure(10), hold on
title(['Eyring stress at U = ',num2str(U_entrain),' m/s'])
xlabel('Pressure (MPa)'), ylabel('Eyring stress (Pa)')
set(gca, 'YScale', 'log')
xlim([400,1200]),ylim([0,3*1e7])
if length(U) == 3
    annotation('textbox',[.78 .2 .12 .2],'String','__  1  m/s  -
```

```
        -   1.5 m/s            2   m/s')
44      title('Eyring stress')
45  elseif length(U) == 1
46      title(['Eyring stress at U = ',num2str(U),' m/s'])
47  end
48  fig10 = gcf;
49  fig10.Position = [300, 300, 700, 350];
50
51  % Graph for alpha coefficient
52  figure(11), hold on
53  xlabel('Pressure (MPa)'), ylabel('\alpha')
54  xlim([400,1200])
55  if length(U) ==3
56      annotation('textbox',[.78 .2 .12 .2],'String','__   1   m/s    -
        -   1.5 m/s            2   m/s')
57      title('pressure-viscosity coefficient')
58  elseif length(U) == 1
59      title(['Pressure-viscosity coefficient at U = ',num2str(U),' m/s
        '])
60  end
61  fig11 = gcf;
62  fig11.Position = [300, 300, 700, 350];
63  hold off
64
65  tbINIT = true;
66
67  for a = 1:length(U)
68
69      U_entrain = U(a);
70
71      if U_entrain == 2
72          end_index = 37;
73      else
74          end_index = 55;
75      end
76
77      [Temp_values]       = xlsread([folder file],['Real values ',
           num2str(U_entrain),'mps'],['$A$2:$A$',num2str(end_index)]);
78      [W_values]          = xlsread([folder file],['Real values ',
           num2str(U_entrain),'mps'],['$B$2:$B$',num2str(end_index)]);
79      [U_values]          = xlsread([folder file],['Real values ',
           num2str(U_entrain),'mps'],['$C$2:$C$',num2str(end_index)]);
80      [z_values]          = xlsread([folder file],['Real values ',
           num2str(U_entrain),'mps'],['$D$2:$D$',num2str(end_index)]);
81      [alpha_values]      = xlsread([folder file],['Real values ',
           num2str(U_entrain),'mps'],['$E$2:$E$',num2str(end_index)]);
82      [Eta_values]        = xlsread([folder file],['Real values ',
           num2str(U_entrain),'mps'],['$F$2:$F$',num2str(end_index)]);
83      [Tau_eyring_values] = xlsread([folder file],['Real values ',
           num2str(U_entrain),'mps'],['$G$2:$G$',num2str(end_index)]);
84      [h_values]          = xlsread([folder file],['Real values ',
```

```
    num2str(U_entrain),'mps'],['$H$2:$H$',num2str(end_index)]);
[r_a_values]        = xlsread([folder file],['Real values ',
    num2str(U_entrain),'mps'],['$J$2:$J$',num2str(end_index)]);
[p_values]          = xlsread([folder file],['Real values ',
    num2str(U_entrain),'mps'],['$K$2:$K$',num2str(end_index)]);

% Testing range
T = unique(Temp_values)';                   % Temperature
                        (C)
p = unique(p_values)';                      % Pressure range
                      (Pa)

% Constant Initial parameters
E1 = 2.07*10^11;                            % Youngs modulus of the
    ball    (Pa)
E2 = 2.07*10^11;                            % Youngs modulus of the
    disk    (Pa)
mu1 = 0.29;                                 % Poissons ratio of ball
              (-)
mu2 = 0.29;                                 % Poissons ratio of ring
              (-)
E_ = 2/(((1-mu1^2)/E1)+((1-mu2^2)/E2)); % Combined youngs
    modulus E'    (Pa)

% Empty matrix to stor Deborah numbers
D_max = zeros(length(T),length(p));

for i = 1:length(T)

    figure(i), hold on
    if length(U) == 1
        title(['Stress strain curve for T = ',num2str(T(i)),' (C
            ) and U = ',num2str(U_entrain),' (m/s)'])
    elseif length(U) == 3
        title(['Stress strain curve for T = ',num2str(T(i))])
    end
    set(gca, 'XScale', 'log')
    xlim([10^3 10^8]) , ylim([0 65])
    grid off
    xlabel('Shear rate (s^{-1})'), ylabel('Shear stress (MPa)')

    % Empty arrays to store data
    Heating_array      = [];
    p_heating_array    = [];
    Eyring_stress      = [];
    alpha_array        = [];

    for j = 1:length(p)

        % Fitted values
        index_T = find(Temp_values==T(i),1);
```

```
125             index_P = find(p_values == p(j),1);
126
127             Tau_eyring  = Tau_eyring_values(index_T+(index_P-1))
                    *10^6;
128             z           = z_values(index_T+(index_P-1));
129             Eta         = Eta_values(index_T+(index_P-1));
130             alpha_star  = alpha_values(index_T+(index_P-1));
131             h           = h_values(index_T+(index_P-1));
132             r_a         = r_a_values(index_T+(index_P-1));
133             W           = W_values(index_T+(index_P-1));
134             p(j);
135
136             % Eyring stres
137             Eyring_stress   = [Eyring_stress , Tau_eyring];
138             alpha_array     = [alpha_array, alpha_star];
139
140             % Shear stress and Shear rate
141             if U_entrain == 1.5
142                 name        = sprintf('Step_%dN_%dC_%d', W, T(i),
                        U_entrain*10);
143             else
144                 name        = sprintf('Step_%dN_%dC_%d', W, T(i),
                        U_entrain);
145             end
146
147             if p(j) > 900e6
148                 % Calculation of shear stress and shear rate (1/2"
                        ball)
149                 ShearStress = TractionForce_small.(name)/(pi*r_a^2);
150                 ShearRate   = sort((SlidingSpeed_small.(name)/1000)/
                        h);
151             elseif p(j) < 900e6
152                 % Calculation of shear stress and shear rate (3/4"
                        ball)
153                 ShearStress = TractionForce.(name)/(pi*r_a^2);
154                 ShearRate   = sort((SlidingSpeed.(name)/1000)/h);
155             end
156
157             % Interpolation of the data:
158             ShearRate_q = logspace(log10(min(ShearRate)),log10(max(
                    ShearRate)),70)';
159             ShearStress_q = interpn(ShearRate,ShearStress,
                    ShearRate_q,'cubic');
160
161             % Deborah nummer
162             for k = 1 : length(ShearStress)
163                 G = E_/(2*(1+mu1));
164                 D(k) = (Eta * 2 * U_entrain) / (2 * G * r_a);
165             end
166             D_max(i,j) = max(D);
167
```

```
168             % Eyring
169             Eyring      = @(x) Tau_eyring * asinh((Eta*x)/Tau_eyring
                    );
170             Eyring_plot = @(x) (Tau_eyring * asinh((Eta*x)/
                    Tau_eyring))/1e6;
171
172             % Find starting point of viscous shear heating
173             Stress_eyring       = Eyring(ShearRate_q);
174             error               = flip(ShearStress_q - Stress_eyring
                    );
175             if  (error(1) >= 0) || (abs(error(1)) <= Tolerance)
176                 figure(i)
177                 xline(0)
178             else
179                 Index_heating       = length(ShearRate_q) - find(
                        error>(-1*Tolerance), 1);
180                 ShearRate_heating   = ShearRate_q(Index_heating+1);
181                 Heating_array       = [Heating_array ,
                        ShearRate_heating];
182                 p_heating_array     = [p_heating_array , p_values(j)
                        ];
183                 p_heating_array     = sort(p_heating_array);
184                 figure(i)
185                 xline(ShearRate_heating,'--',Color=colors(j))
186             end
187
188             % Visualization of fitted Eyring with data
189             figure(i)
190             if      a == 1    plot(ShearRate_q,ShearStress_q/1e6,'.-',
                    Color=colors(j));
191             elseif a == 2    plot(ShearRate_q,ShearStress_q/1e6,'.--'
                    ,Color=colors(j));
192             elseif a == 3    plot(ShearRate_q,ShearStress_q/1e6,'.:',
                    Color=colors(j));
193             end
194             plot(ShearRate_q,Stress_eyring/1e6,Color=colors(j),
                    LineStyle=":",LineWidth=1.5)
195
196             %Setting correct names for the legend of figures 1 - 8
197             if a == 1
198             legendLabels{2*j - 1}    = [num2str(round(p(j)/1000000)),
                    ' MPa'];
199             legendLabels{2*j}        = ['Fitted Eyring ',num2str(
                    round(p(j)/1000000)),' MPa'];
200             end
201
202         end
203
204         %Creating table viscous shear heating
205         collect = table();
206         collect.T = T(i)*ones(size(Heating_array'));
```

```
207         collect.speed = U(a)*ones(size(Heating_array'));
208         collect.P = (p_heating_array/1e6)';
209         collect.LimitStrain = Heating_array';
210         if tbINIT
211             allCollect = collect;
212             tbINIT = false;
213         else
214             allCollect = [allCollect; collect];
215         end
216
217         legend(legendLabels, 'Orientation', 'horizontal','NumColumns
                ', 2);
218         fig = gcf;
219         fig.Position = [300, 300, 700, 500];
220         hold off
221
222         % Legend names for figure 9
223         legendLabels2{i}              = ['T = ',num2str(T(i)),' (C)'
                ];
224
225         % Fitting formula for a and b :  y=a*exp(b*x)
226         f = fit((p_heating_array/1e6)',Heating_array','exp1');
227
228         % Figure starting strain for viscous shear heating
229         figure(9), hold on
230         if      a == 1    pl = plot((p_heating_array/1e6),
                Heating_array,'.-',Color=colors(i),LineWidth=1);
231         elseif a == 2    pl = plot((p_heating_array/1e6),
                Heating_array,'.--',Color=colors(i),LineWidth=1);
232         elseif a == 3    pl = plot((p_heating_array/1e6),
                Heating_array,'.:',Color=colors(i),LineWidth=1);
233         end
234         legend(legendLabels2,Location='Bestoutside')
235         hold off
236
237         % Figure for Eyring stress
238         figure(10), hold on
239         if      a == 1    plot((p/1e6),Eyring_stress,'.-',Color=colors
                (i),LineWidth=1)
240         elseif a == 2    plot((p/1e6),Eyring_stress,'.--',Color=
                colors(i),LineWidth=1)
241         elseif a == 3    plot((p/1e6),Eyring_stress,'.:',Color=colors
                (i),LineWidth=1)
242         end
243         legend(legendLabels2,Location='Bestoutside')
244         hold off
245
246         % Figure for Alpha coefficient
247         figure(11), hold on
248         if      a == 1    plot((p/1e6),alpha_array,'.-',Color=colors(i
                ),LineWidth=1)
```

```
249         elseif a == 2   plot((p/1e6),alpha_array,'.--',Color=colors(
                i),LineWidth=1)
250         elseif a == 3   plot((p/1e6),alpha_array,'.:',Color=colors(i
                ),LineWidth=1)
251         end
252         legend(legendLabels2,Location='Bestoutside')
253         hold off
254
255     end
256
257     disp(['The max De number is ',num2str(max(max(D_max)))])
258
259 end
260
261 %%
262
263 save CollectDat_nb.mat allCollect -v7.3
264 clearvars -except allCollect T
265
266 figure(99)
267 clf
268 pid = linspace(400,1110,20);
269
270 for cntT = 1:1:length(T)
271 cT = T(cntT);
272 idxT = allCollect.T==cT;
273 x = allCollect.P(idxT);
274 y = allCollect.LimitStrain(idxT)*1e-6;
275
276 % Fitting data
277 [xData, yData] = prepareCurveData( x, y );
278 ft = fittype( 'a*exp(b*x)+c', 'independent', 'x', 'dependent', 'y' )
        ;
279 opts = fitoptions( 'Method', 'NonlinearLeastSquares' );
280 opts.Display = 'Off';
281 if      cntT == 1   opts.StartPoint = [2000 -0.015 0.2];
282 elseif  cntT == 2   opts.StartPoint = [500 -0.01 0.26];
283 elseif  cntT == 3   opts.StartPoint = [250 -0.008 0.4];
284 elseif  cntT == 4   opts.StartPoint = [310 -0.0075 0.6];
285     pid = linspace(540,1110,20);
286 elseif  cntT == 5   opts.StartPoint = [210 -0.0055 0.6];
287     pid = linspace(540,1110,20);
288 elseif  cntT == 6   opts.StartPoint = [400 -0.0055 0.6];
289     pid = linspace(540,1110,20);
290 end
291 [fitresult, gof] = fit( xData, yData, ft, opts );
292
293 % Plot data and fit
294 hl = plot(x,y,'.');
295 hold on
296 plot(pid, fitresult.a*exp(pid*fitresult.b)+fitresult.c, '-', "
```

```
    LineWidth",1.3, "Color", hl.Color)
297 legentry{cntT*2-1} = ['T = ', num2str(cT),' C'];
298 legentry{cntT*2} = ['Fitted curve for T = ', num2str(cT),' C'];
299 disp(['T ', num2str(cT), '; a: ', num2str(fitresult.a, '%.2f'), ' b:
      ', num2str(fitresult.b, '%.2f'), ' c: ', num2str(fitresult.c, '
    %.2f'), ' gof: ', num2str(gof.rsquare, '%.3f')])
300 end
301 legend(legentry,'Orientation', 'horizontal','NumColumns', 2)
302 title('Starting strain for viscous shear heating')
303 hax = gca;
304 hax.XLabel.String = 'pressure in MPa';
305 hax.YLabel.String = '\gamma_L x10^6 in s^{-1}';
```

B Results

B.1 MTM Results 3/4" ball

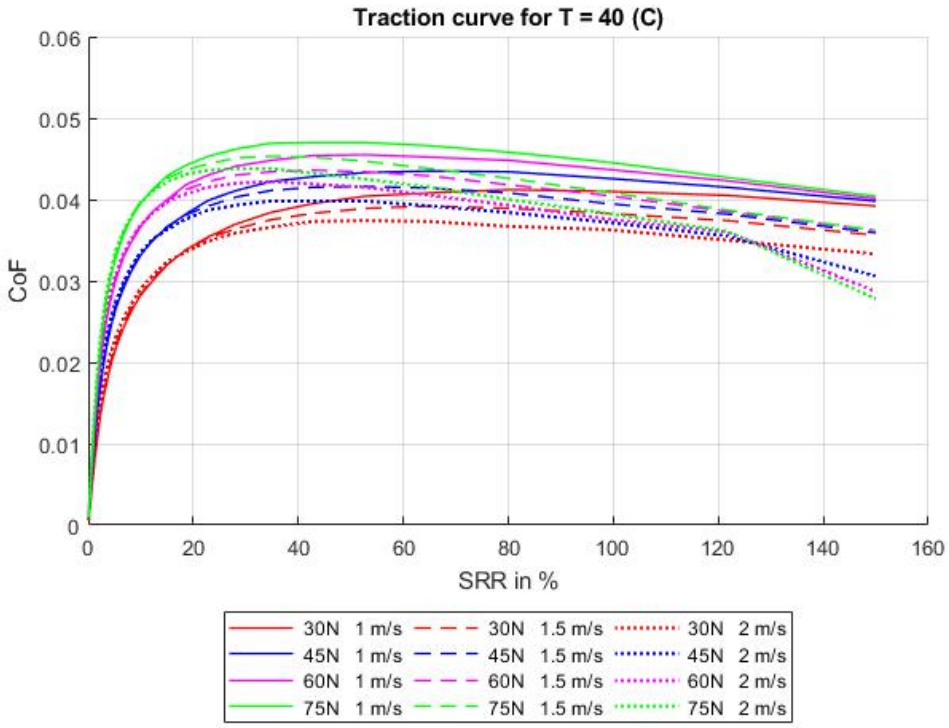

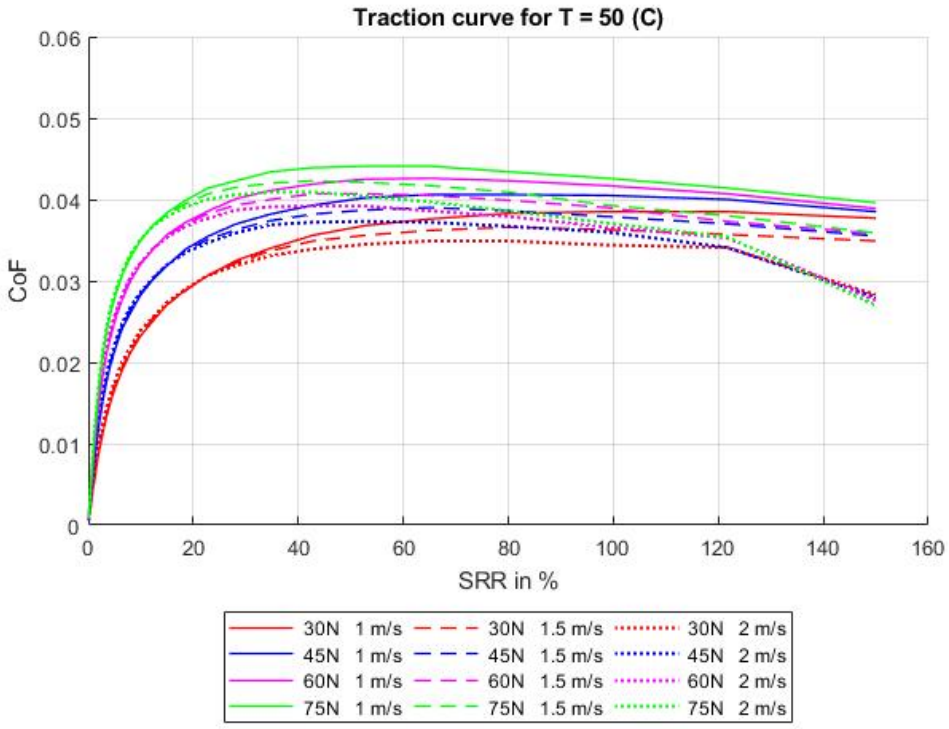

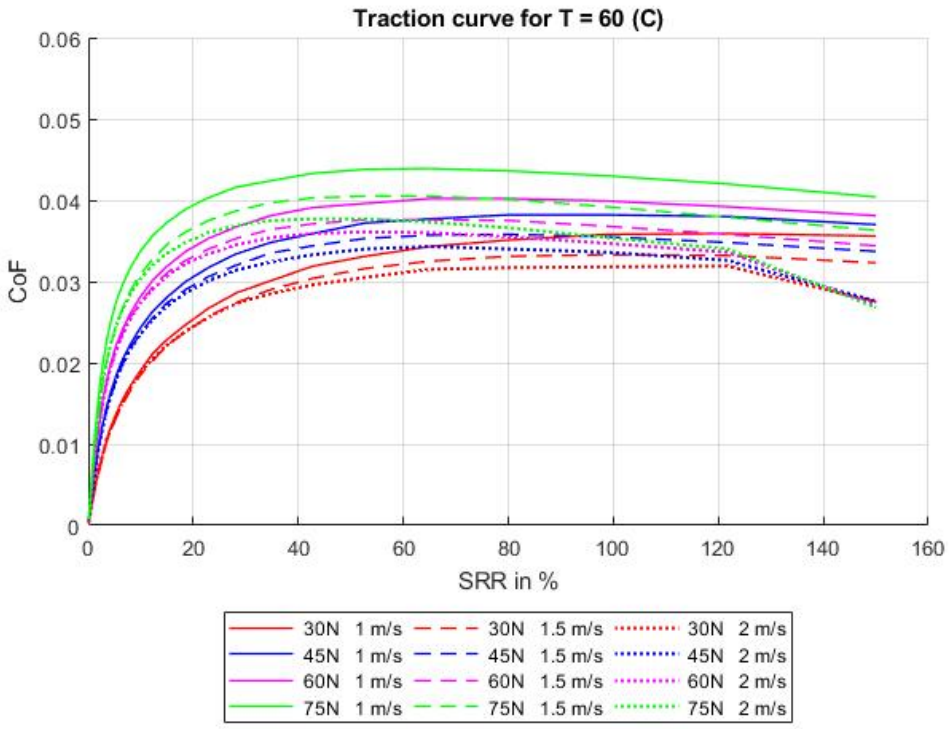
Traction curve for T = 60 (C)
CoF
SRR in %
0.06
0.05
0.04
0.03
0.02
0.01
0
0
20
40
60
80
100
120
140
160
30N 1 m/s
30N 1.5 m/s
30N 2 m/s
45N 1 m/s
45N 1.5 m/s
45N 2 m/s
60N 1 m/s
60N 1.5 m/s
60N 2 m/s
75N 1 m/s
75N 1.5 m/s
75N 2 m/s

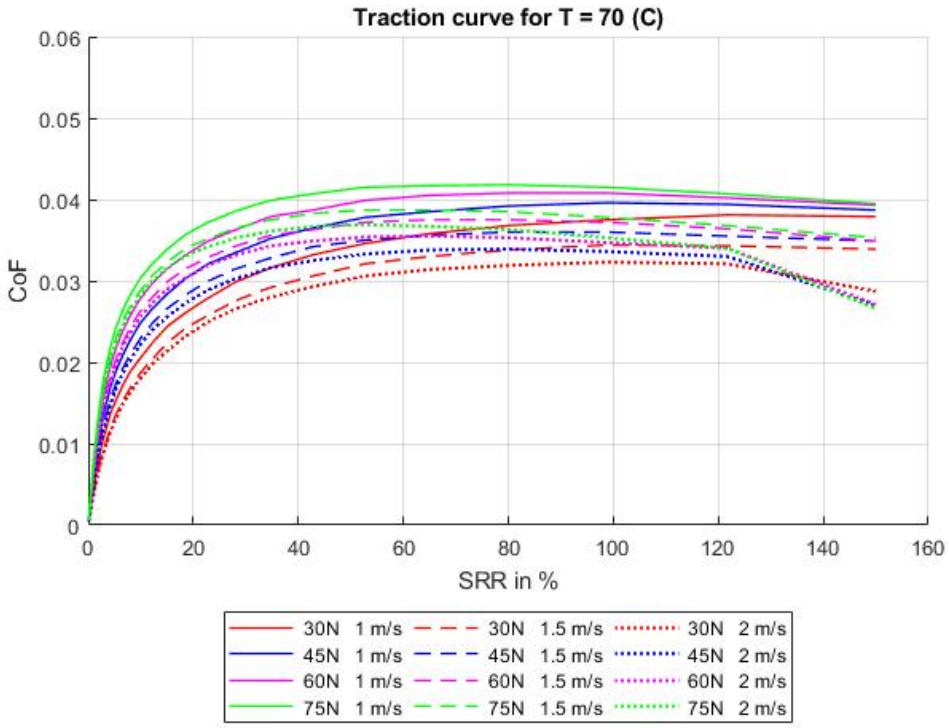
Traction curve for T = 70 (C)
CoF
SRR in %
0.06
0.05
0.04
0.03
0.02
0.01
0
0
20
40
60
80
100
120
140
160
30N 1 m/s
30N 1.5 m/s
30N 2 m/s
45N 1 m/s
45N 1.5 m/s
45N 2 m/s
60N 1 m/s
60N 1.5 m/s
60N 2 m/s
75N 1 m/s
75N 1.5 m/s
75N 2 m/s

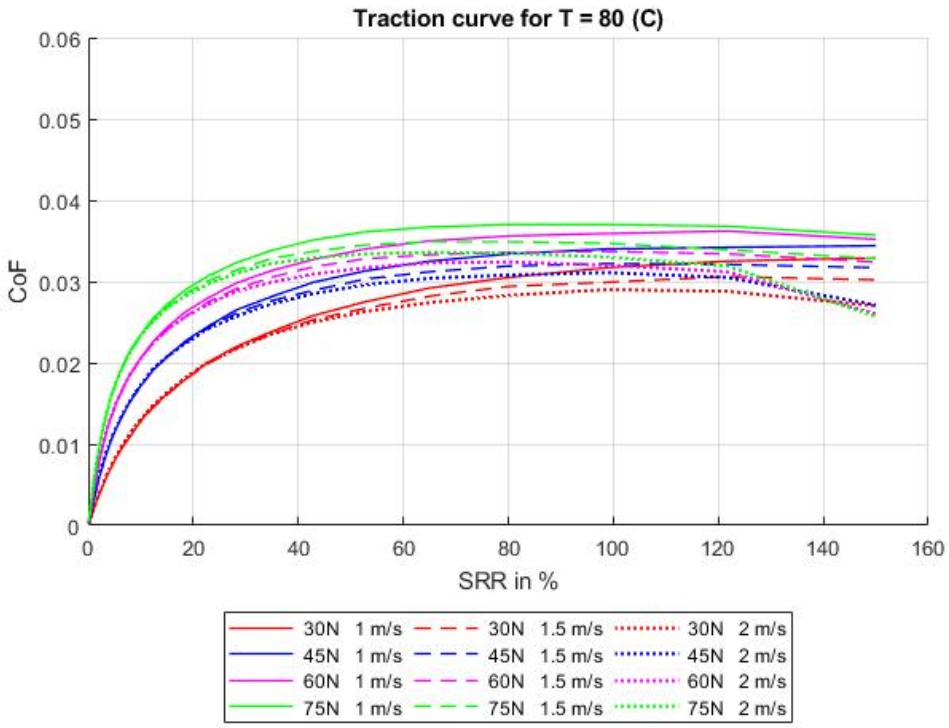
Traction curve for T = 80 (C)
CoF
SRR in %
0.06
0.05
0.04
0.03
0.02
0.01
0
0
20
40
60
80
100
120
140
160
30N 1 m/s
30N 1.5 m/s
30N 2 m/s
45N 1 m/s
45N 1.5 m/s
45N 2 m/s
60N 1 m/s
60N 1.5 m/s
60N 2 m/s
75N 1 m/s
75N 1.5 m/s
75N 2 m/s

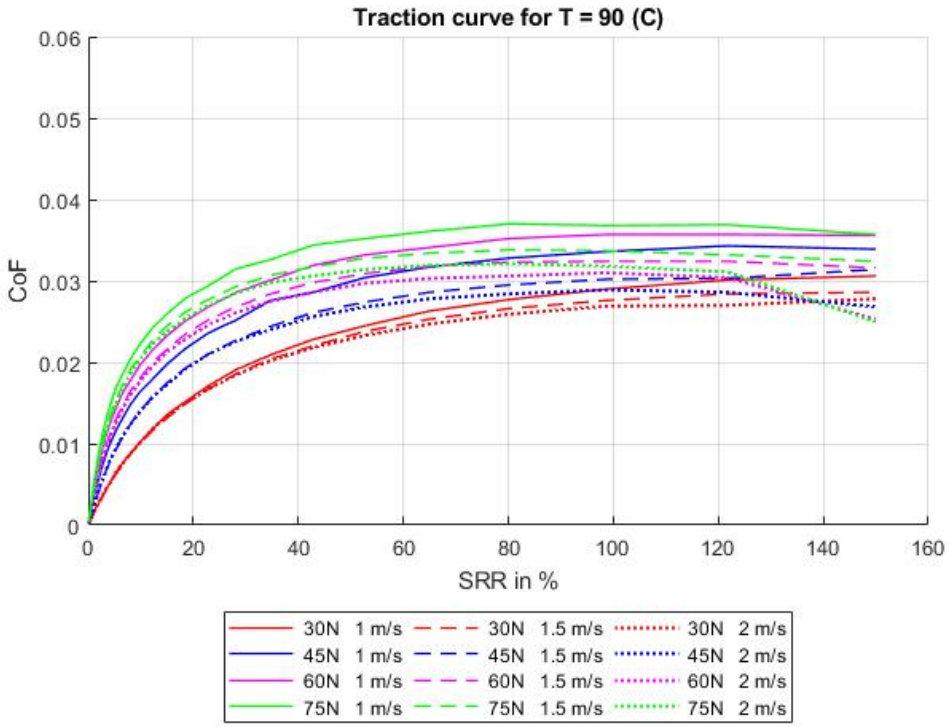
Traction curve for T = 90 (C)
CoF
SRR in %
0.06
0.05
0.04
0.03
0.02
0.01
0
0
20
40
60
80
100
120
140
160
30N 1 m/s
30N 1.5 m/s
30N 2 m/s
45N 1 m/s
45N 1.5 m/s
45N 2 m/s
60N 1 m/s
60N 1.5 m/s
60N 2 m/s
75N 1 m/s
75N 1.5 m/s
75N 2 m/s

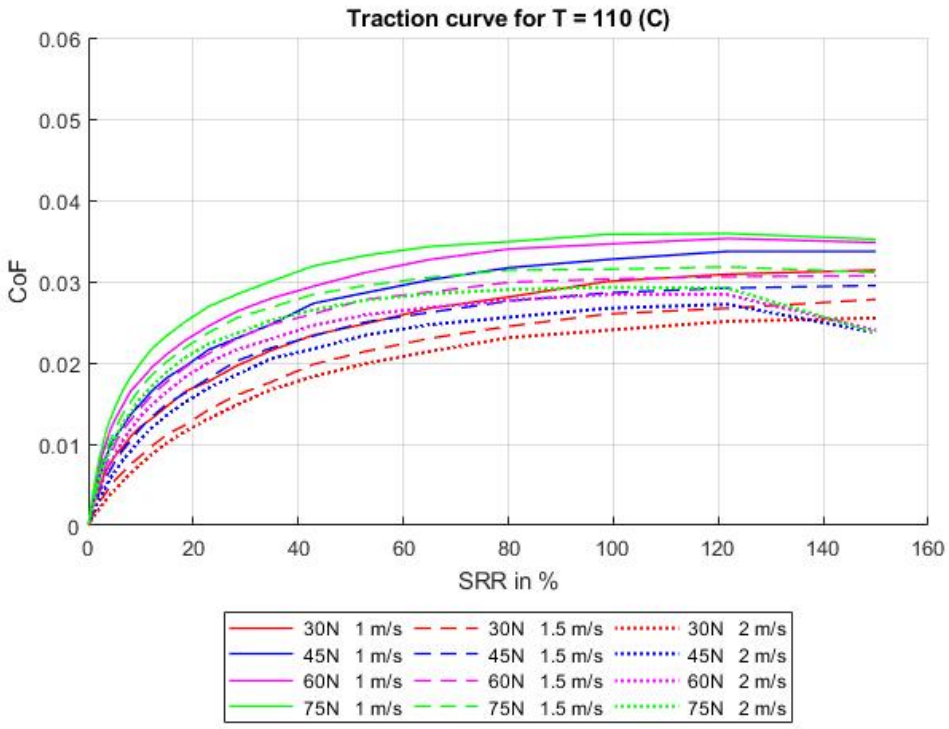
Traction curve for T = 110 (C)
CoF
SRR in %
0.06
0.05
0.04
0.03
0.02
0.01
0
0
20
40
60
80
100
120
140
160
30N 1 m/s
30N 1.5 m/s
30N 2 m/s
45N 1 m/s
45N 1.5 m/s
45N 2 m/s
60N 1 m/s
60N 1.5 m/s
60N 2 m/s
75N 1 m/s
75N 1.5 m/s
75N 2 m/s

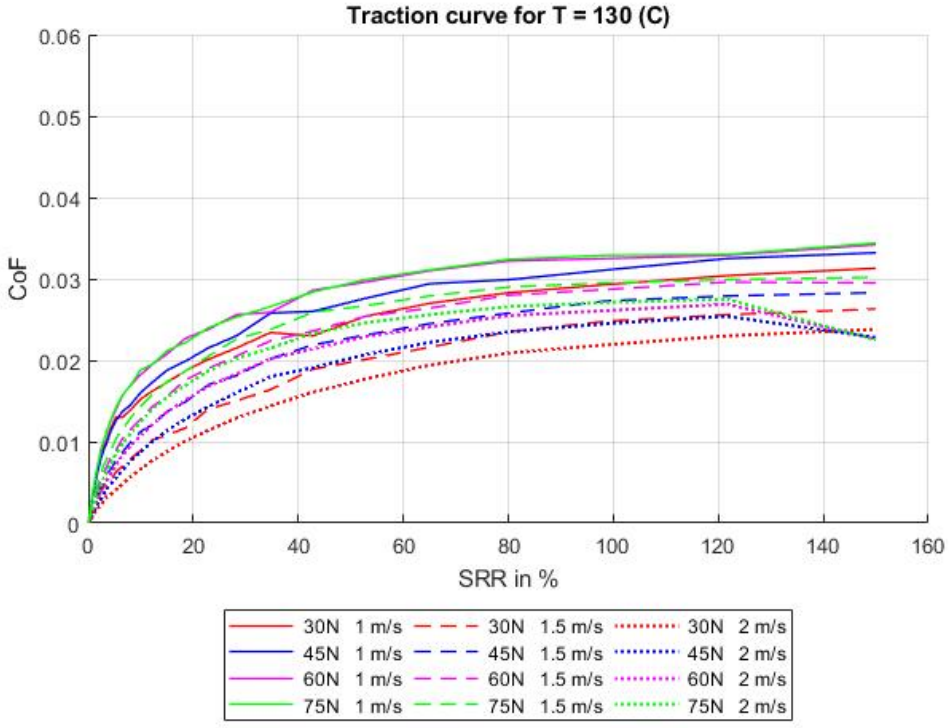
Traction curve for T = 130 (C)
CoF
SRR in %
0.06
0.05
0.04
0.03
0.02
0.01
0
0
20
40
60
80
100
120
140
160
30N 1 m/s
30N 1.5 m/s
30N 2 m/s
45N 1 m/s
45N 1.5 m/s
45N 2 m/s
60N 1 m/s
60N 1.5 m/s
60N 2 m/s
75N 1 m/s
75N 1.5 m/s
75N 2 m/s

B.2 MTM Results 1/2" ball

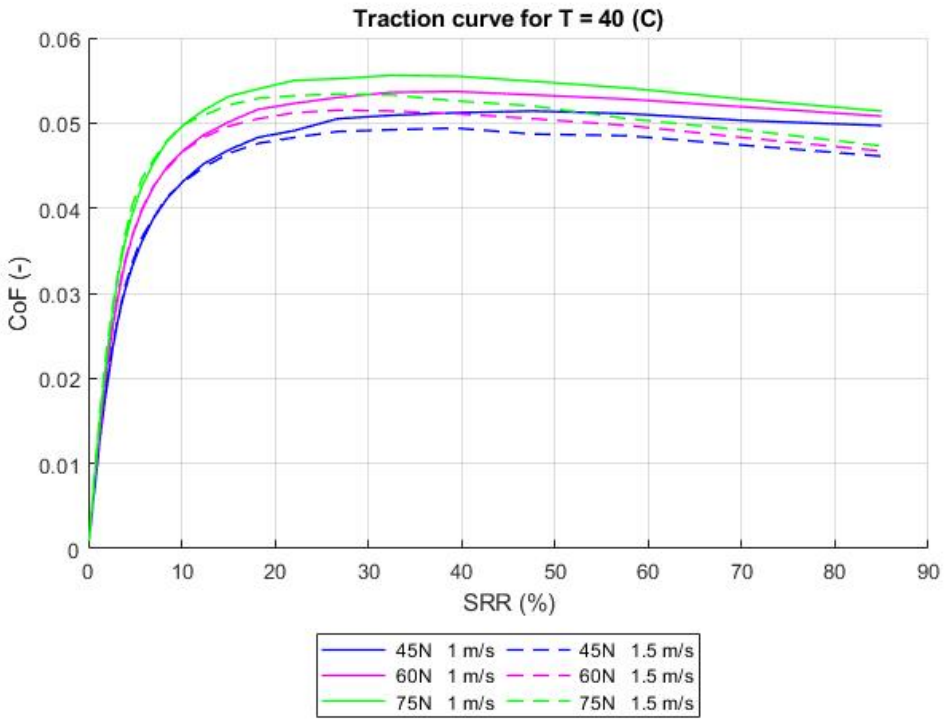

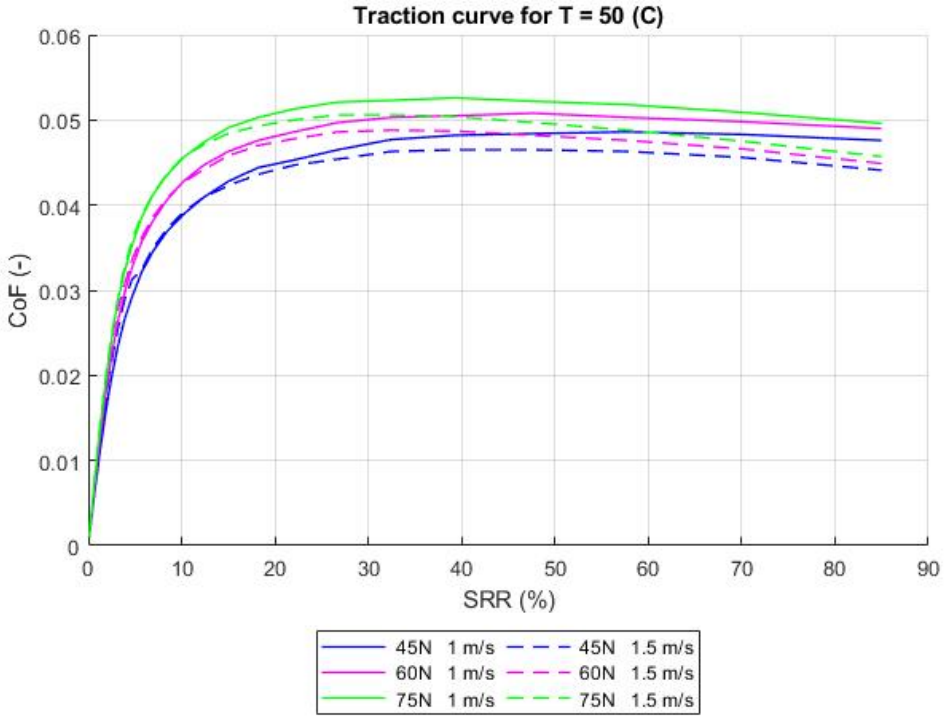

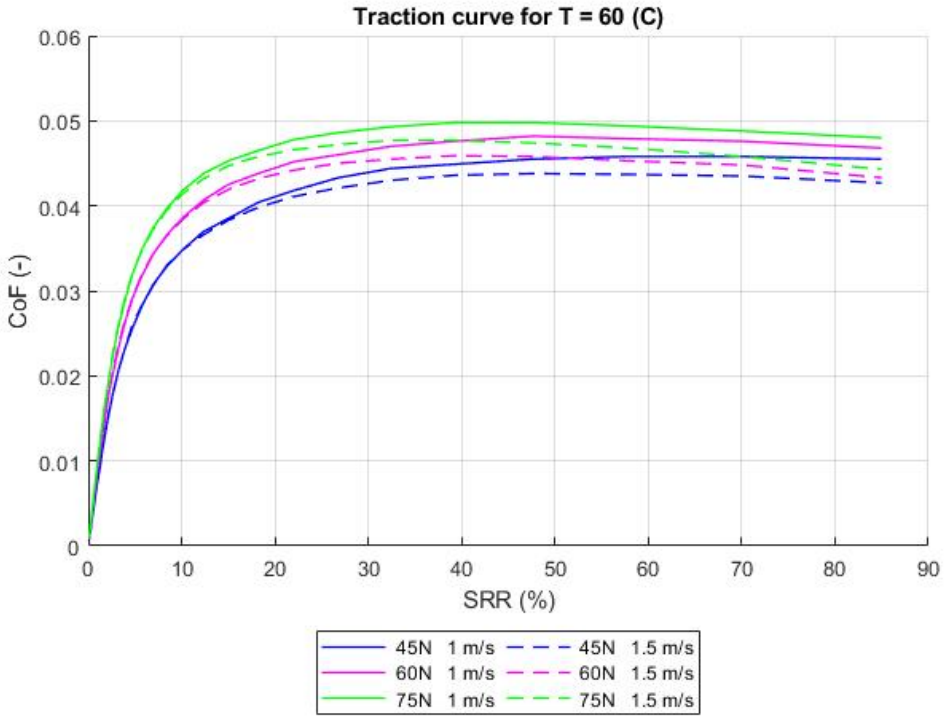
Traction curve for T = 60 (C)
CoF (-)
SRR (%)
0.06
0.05
0.04
0.03
0.02
0.01
0
0
10
20
30
40
50
60
70
80
90
45N 1 m/s
60N 1 m/s
75N 1 m/s
45N 1.5 m/s
60N 1.5 m/s
75N 1.5 m/s

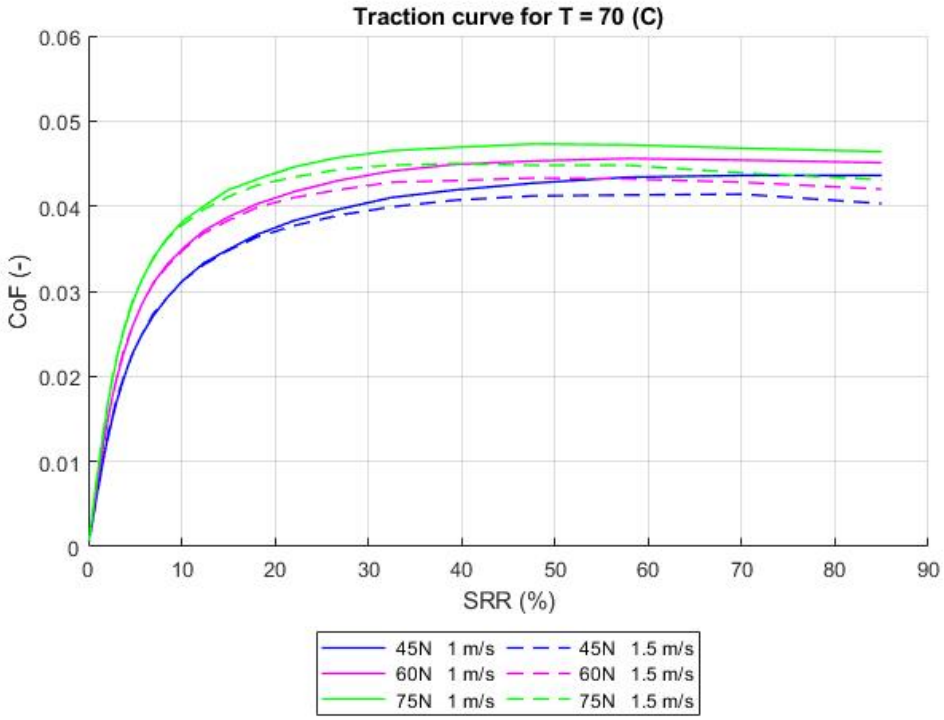
Traction curve for T = 70 (C)
CoF (-)
SRR (%)
0.06
0.05
0.04
0.03
0.02
0.01
0
0
10
20
30
40
50
60
70
80
90
45N 1 m/s
60N 1 m/s
75N 1 m/s
45N 1.5 m/s
60N 1.5 m/s
75N 1.5 m/s

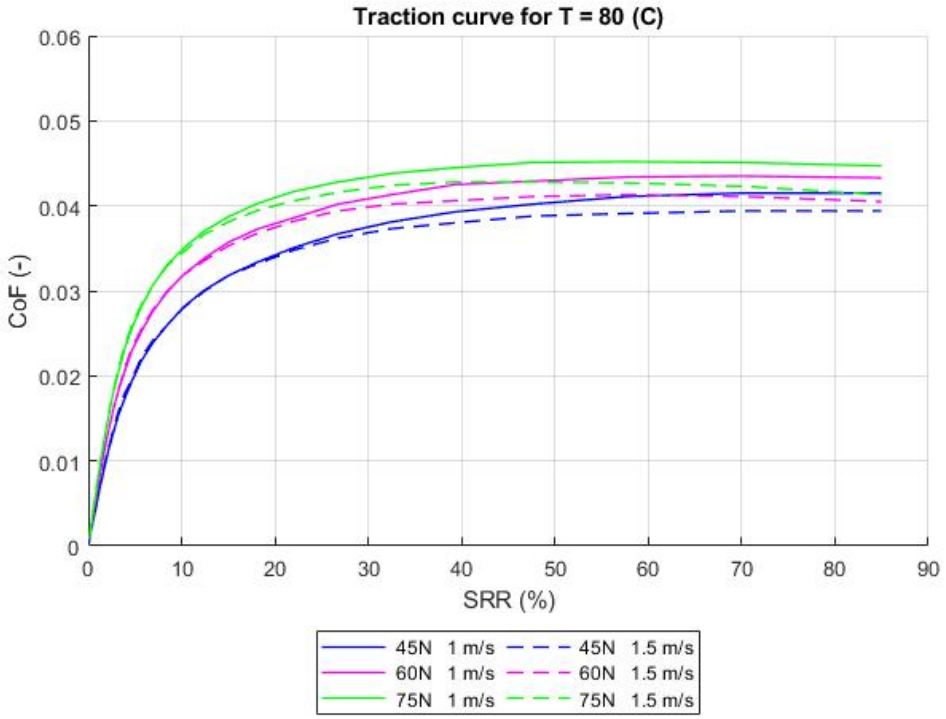
Traction curve for T = 80 (C)
CoF (-)
SRR (%)
0.06
0.05
0.04
0.03
0.02
0.01
0
0
10
20
30
40
50
60
70
80
90
45N 1 m/s
60N 1 m/s
75N 1 m/s
45N 1.5 m/s
60N 1.5 m/s
75N 1.5 m/s

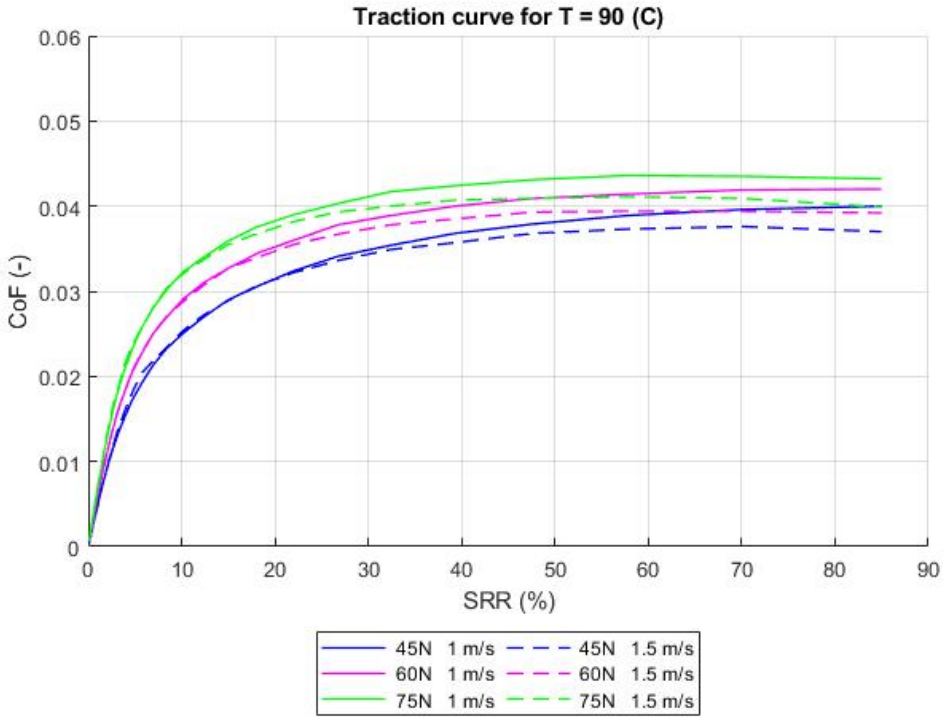
Traction curve for T = 90 (C)
CoF (-)
SRR (%)
0.06
0.05
0.04
0.03
0.02
0.01
0
0
10
20
30
40
50
60
70
80
90
45N 1 m/s
60N 1 m/s
75N 1 m/s
45N 1.5 m/s
60N 1.5 m/s
75N 1.5 m/s

B.3 Stress-Strain curves

Entrainment speed: $U = 1\ m/s$

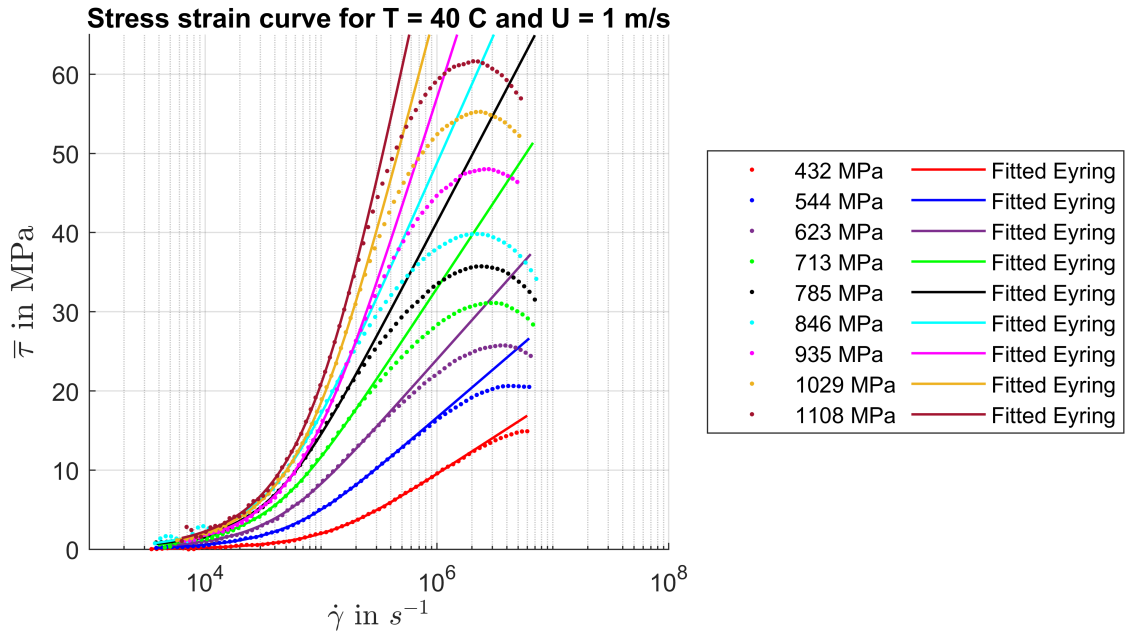

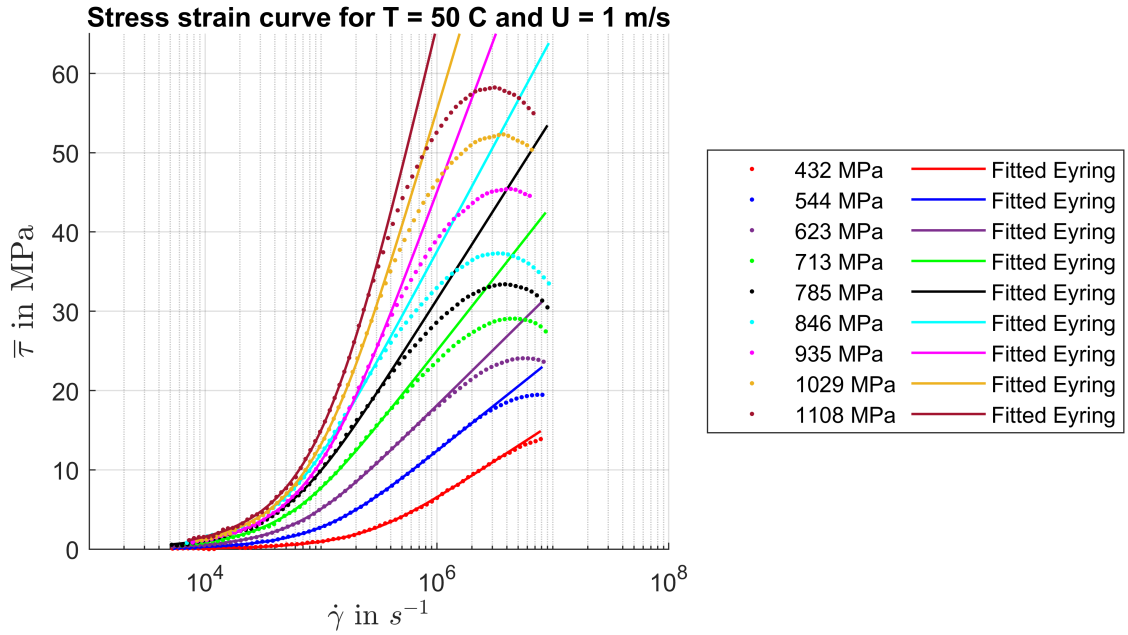

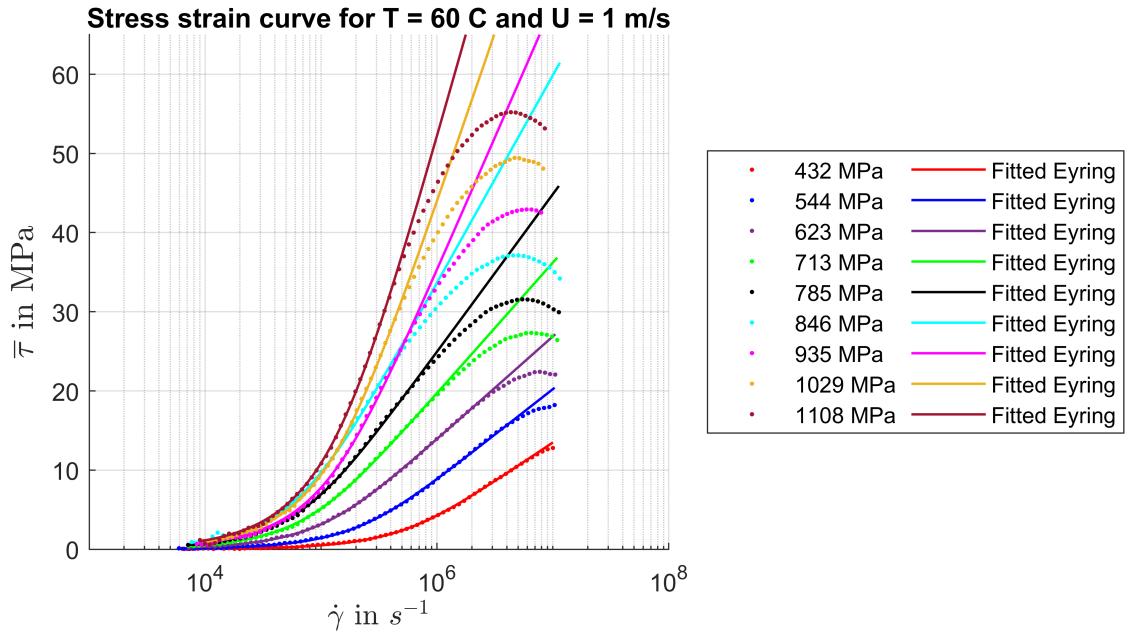
Stress strain curve for T = 60 C and U = 1 m/s
$\overline{\tau}$ in MPa
$\dot{\gamma}$ in s^{-1}
0
10
20
30
40
50
60
10^4
10^6
10^8
432 MPa
544 MPa
623 MPa
713 MPa
785 MPa
846 MPa
935 MPa
1029 MPa
1108 MPa
Fitted Eyring

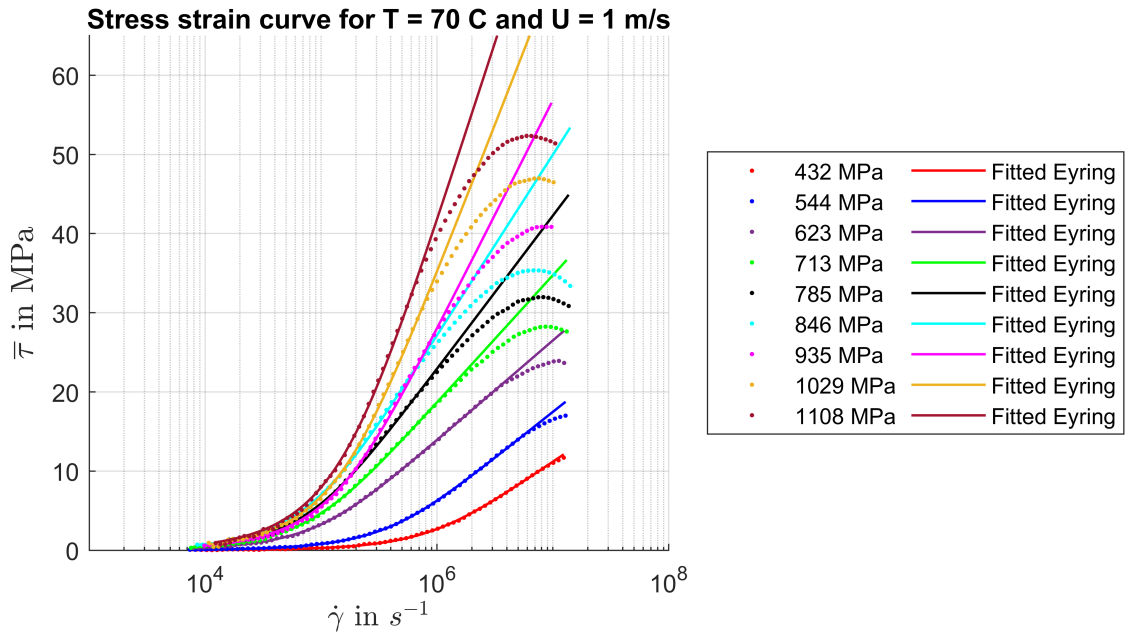
Stress strain curve for T = 70 C and U = 1 m/s
$\overline{\tau}$ in MPa
$\dot{\gamma}$ in s^{-1}
0
10
20
30
40
50
60
10^4
10^6
10^8
432 MPa
544 MPa
623 MPa
713 MPa
785 MPa
846 MPa
935 MPa
1029 MPa
1108 MPa
Fitted Eyring

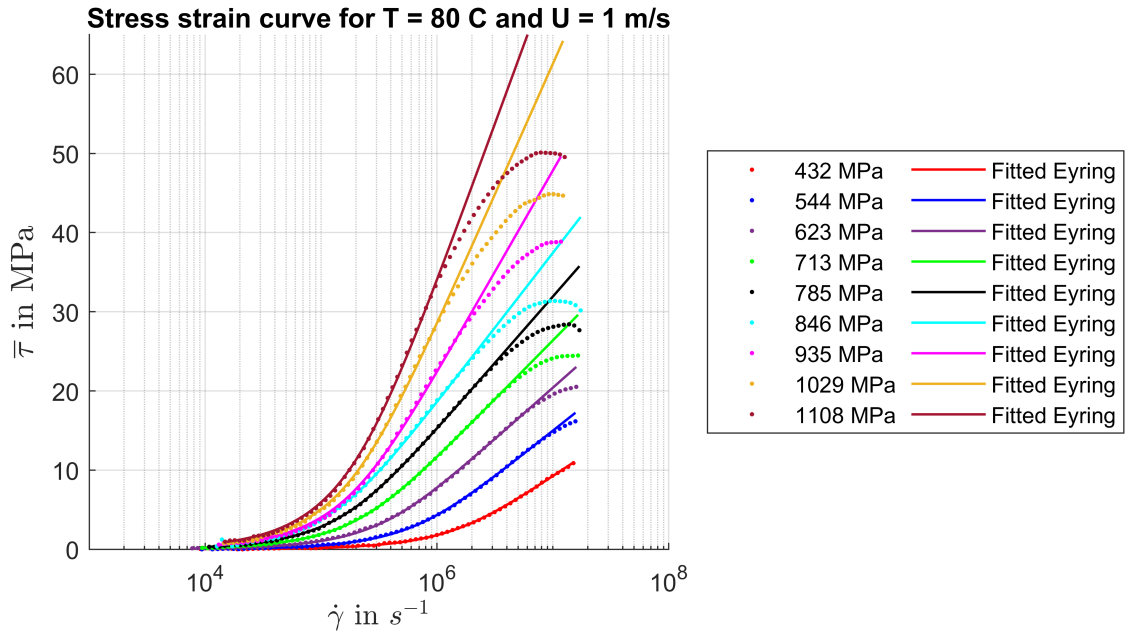
Stress strain curve for T = 80 C and U = 1 m/s
$\overline{\tau}$ in MPa
$\dot{\gamma}$ in s^{-1}
0
10
20
30
40
50
60
10^4
10^6
10^8
432 MPa
544 MPa
623 MPa
713 MPa
785 MPa
846 MPa
935 MPa
1029 MPa
1108 MPa
Fitted Eyring

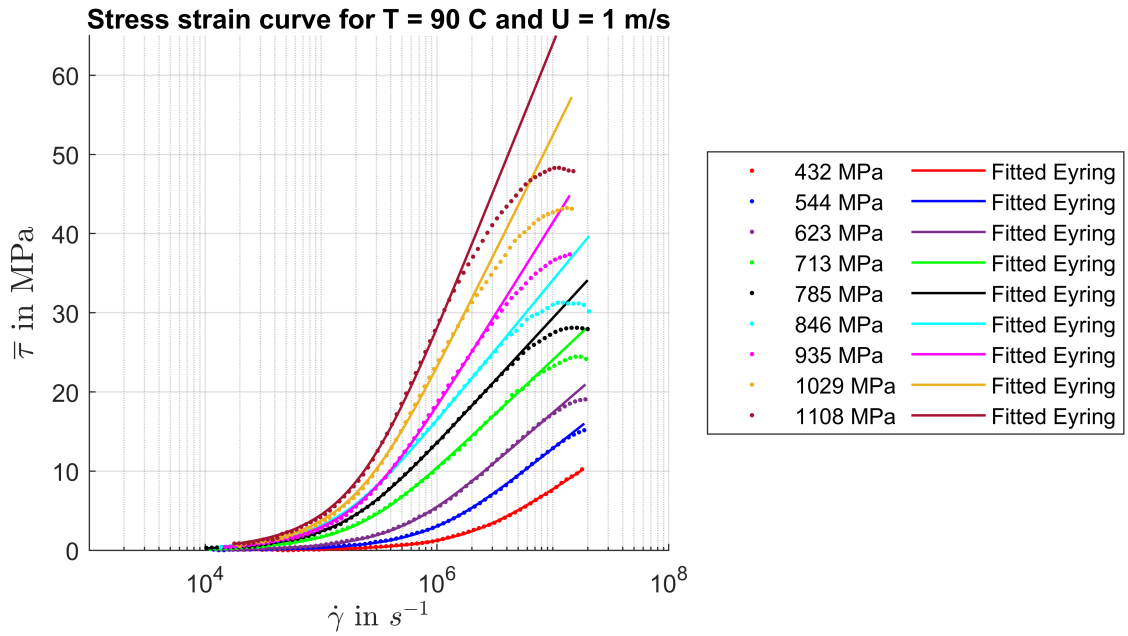
Stress strain curve for T = 90 C and U = 1 m/s
$\overline{\tau}$ in MPa
$\dot{\gamma}$ in s^{-1}
0
10
20
30
40
50
60
10^4
10^6
10^8
432 MPa
544 MPa
623 MPa
713 MPa
785 MPa
846 MPa
935 MPa
1029 MPa
1108 MPa
Fitted Eyring

Entrainment speed: $U = 1.5\ m/s$

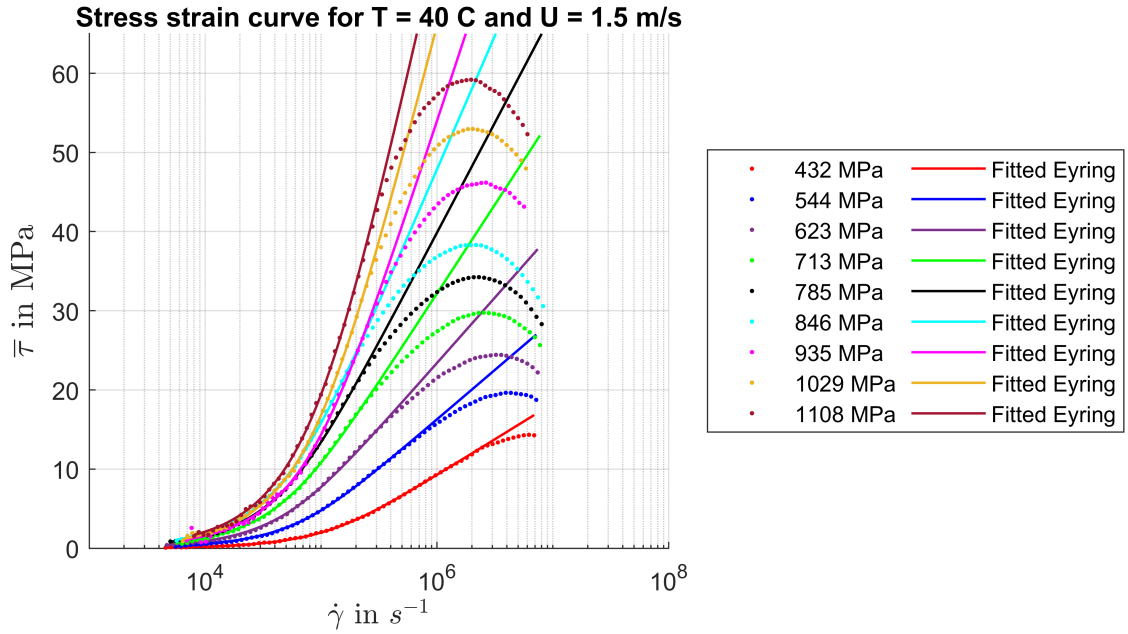

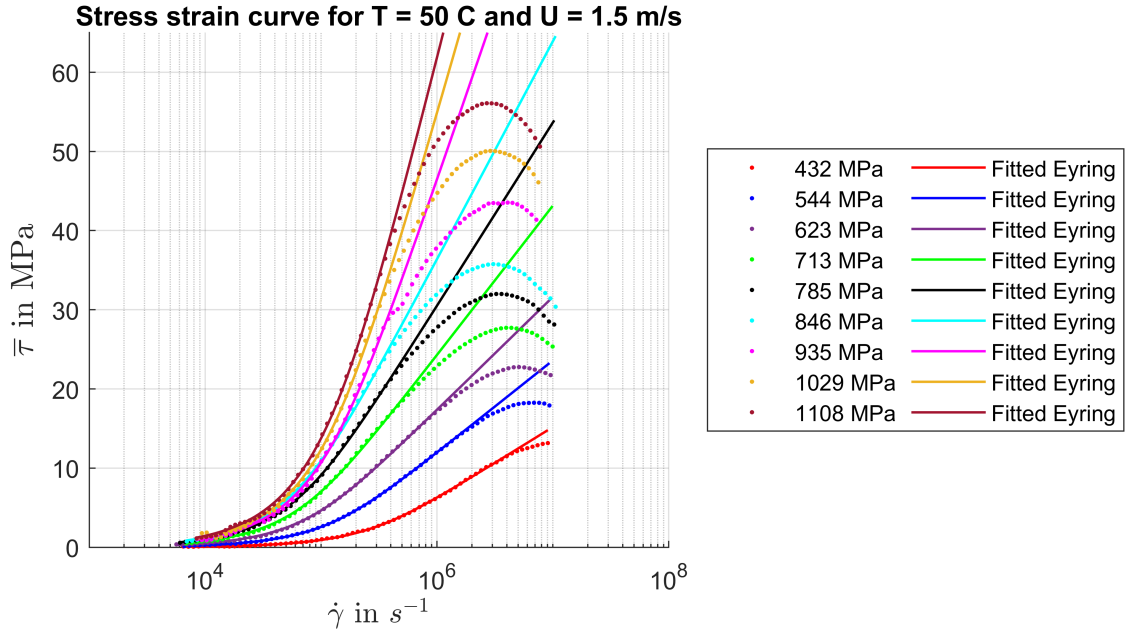

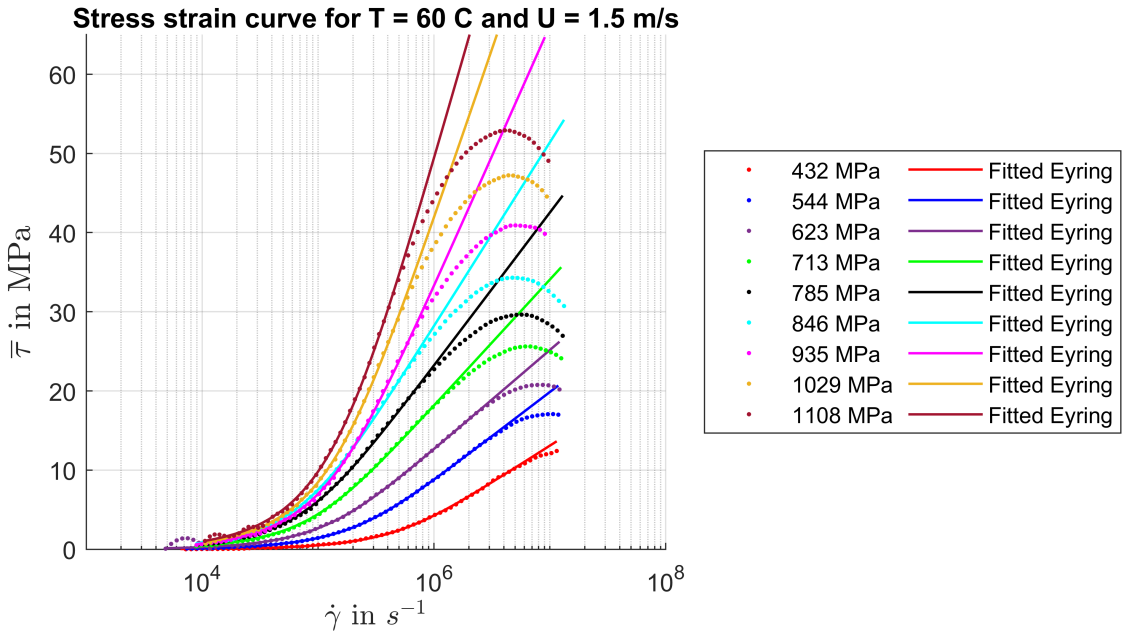
Stress strain curve for T = 60 C and U = 1.5 m/s
$\overline{\tau}$ in MPa
$\dot{\gamma}$ in s^{-1}
0
10
20
30
40
50
60
10^4
10^6
10^8
432 MPa
544 MPa
623 MPa
713 MPa
785 MPa
846 MPa
935 MPa
1029 MPa
1108 MPa
Fitted Eyring

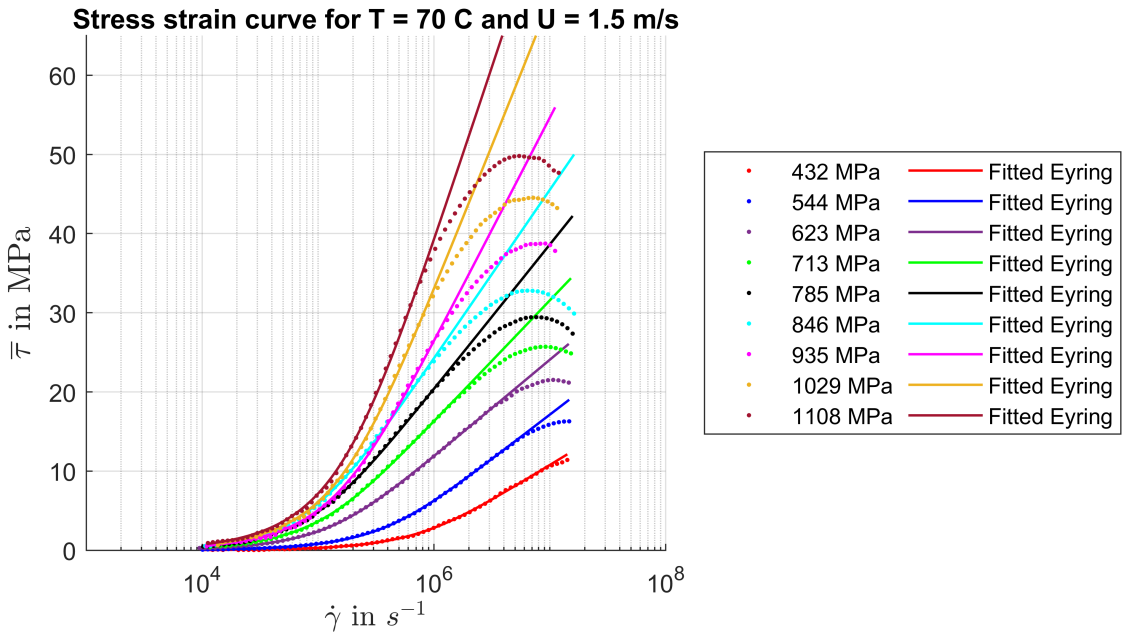
Stress strain curve for T = 70 C and U = 1.5 m/s
$\overline{\tau}$ in MPa
$\dot{\gamma}$ in s^{-1}
0
10
20
30
40
50
60
10^4
10^6
10^8
432 MPa
544 MPa
623 MPa
713 MPa
785 MPa
846 MPa
935 MPa
1029 MPa
1108 MPa
Fitted Eyring

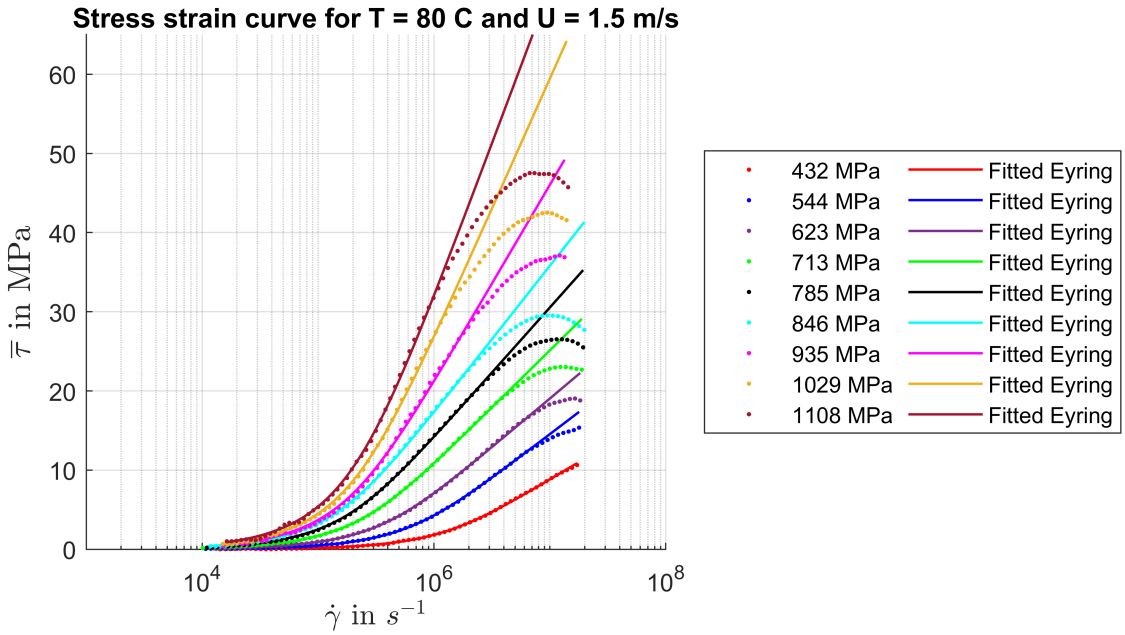
Stress strain curve for T = 80 C and U = 1.5 m/s
$\overline{\tau}$ in MPa
$\dot{\gamma}$ in s^{-1}
0
10
20
30
40
50
60
10^4
10^6
10^8
432 MPa
544 MPa
623 MPa
713 MPa
785 MPa
846 MPa
935 MPa
1029 MPa
1108 MPa
Fitted Eyring

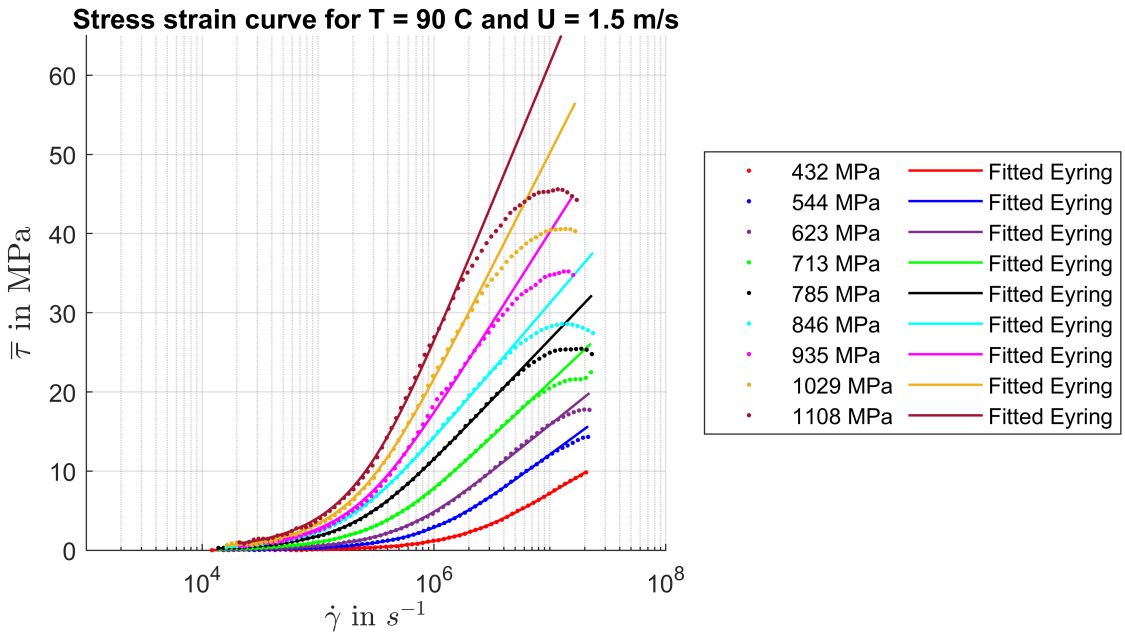
Stress strain curve for T = 90 C and U = 1.5 m/s
$\overline{\tau}$ in MPa
$\dot{\gamma}$ in s^{-1}
0
10
20
30
40
50
60
10^4
10^6
10^8
432 MPa
544 MPa
623 MPa
713 MPa
785 MPa
846 MPa
935 MPa
1029 MPa
1108 MPa
Fitted Eyring

Entrainment speed: $U = 2\ m/s$

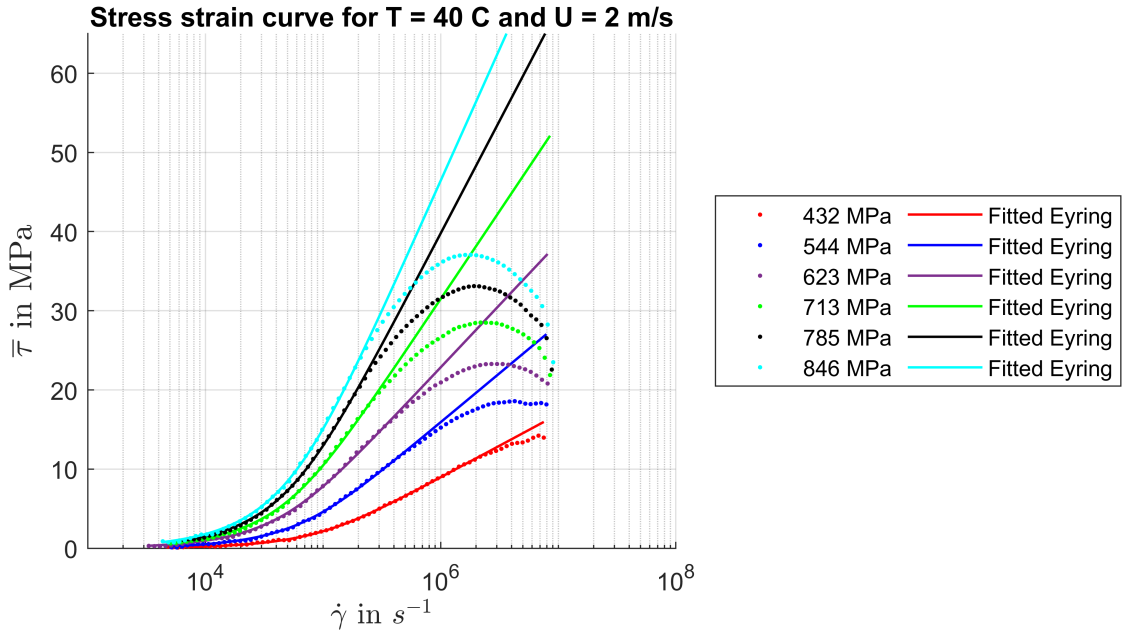

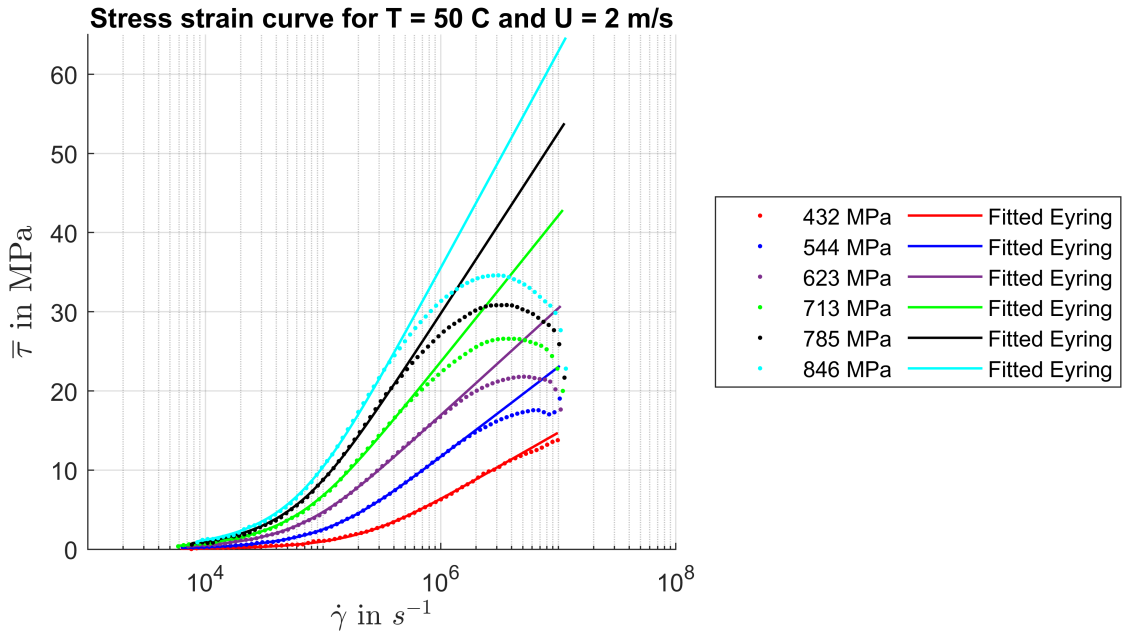

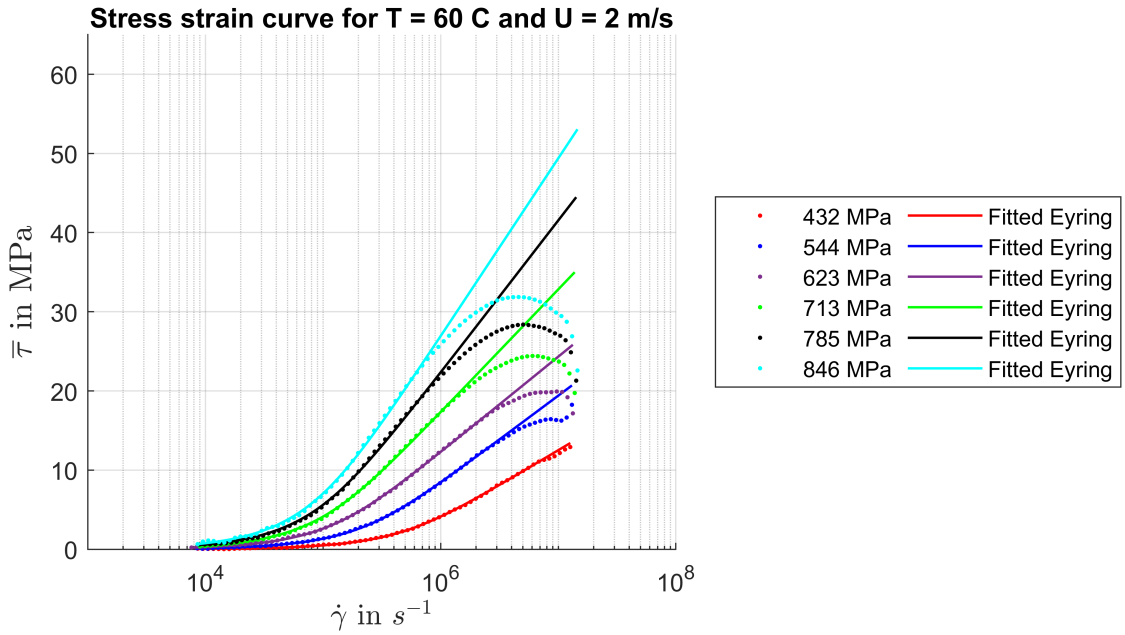
Stress strain curve for T = 60 C and U = 2 m/s
$\overline{\tau}$ in MPa
$\dot{\gamma}$ in s^{-1}
0
10
20
30
40
50
60
10^4
10^6
10^8
432 MPa
544 MPa
623 MPa
713 MPa
785 MPa
846 MPa
Fitted Eyring
Fitted Eyring
Fitted Eyring
Fitted Eyring
Fitted Eyring
Fitted Eyring

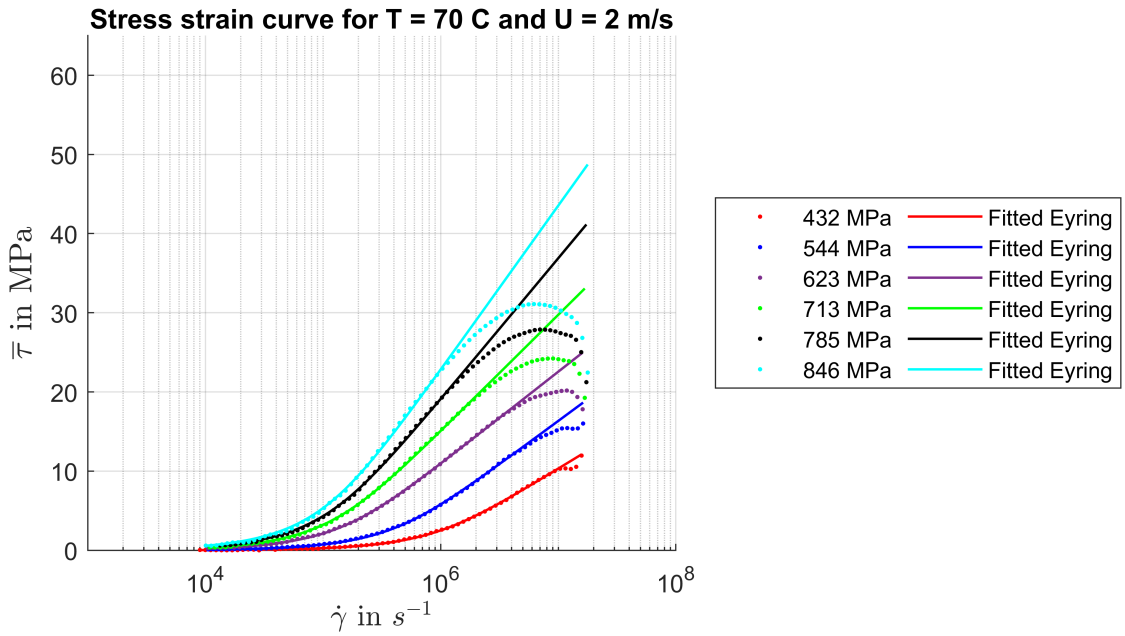
Stress strain curve for T = 70 C and U = 2 m/s
$\overline{\tau}$ in MPa
$\dot{\gamma}$ in s^{-1}
0
10
20
30
40
50
60
10^4
10^6
10^8
432 MPa
544 MPa
623 MPa
713 MPa
785 MPa
846 MPa
Fitted Eyring
Fitted Eyring
Fitted Eyring
Fitted Eyring
Fitted Eyring
Fitted Eyring

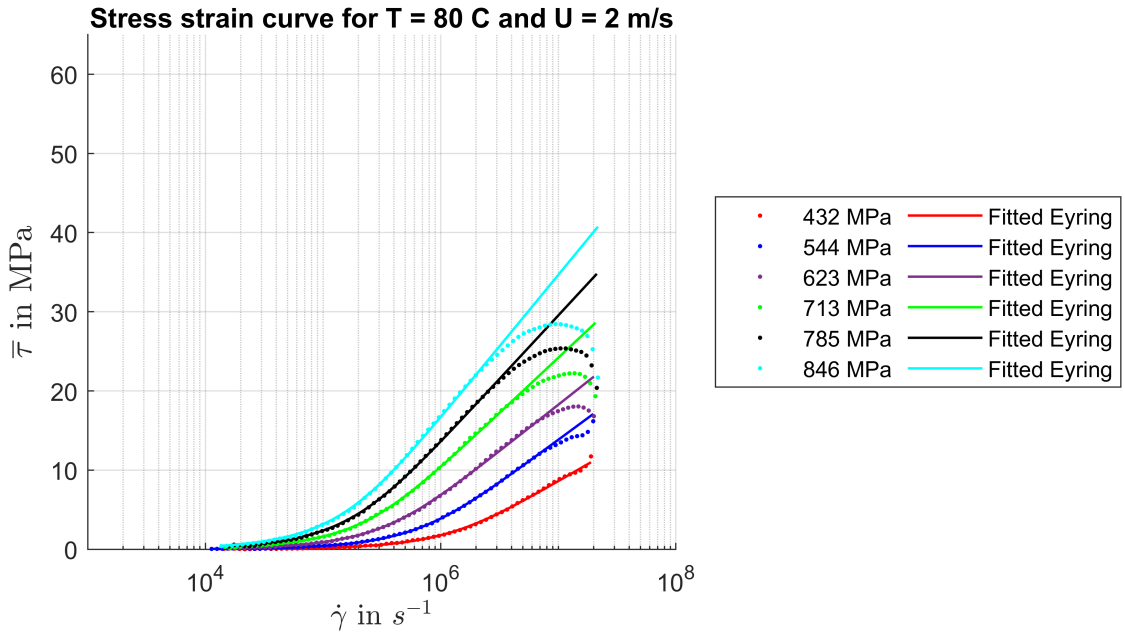
Stress strain curve for T = 80 C and U = 2 m/s
$\overline{\tau}$ in MPa
$\dot{\gamma}$ in s^{-1}
0
10
20
30
40
50
60
10^4
10^6
10^8
432 MPa
544 MPa
623 MPa
713 MPa
785 MPa
846 MPa
Fitted Eyring
Fitted Eyring
Fitted Eyring
Fitted Eyring
Fitted Eyring
Fitted Eyring

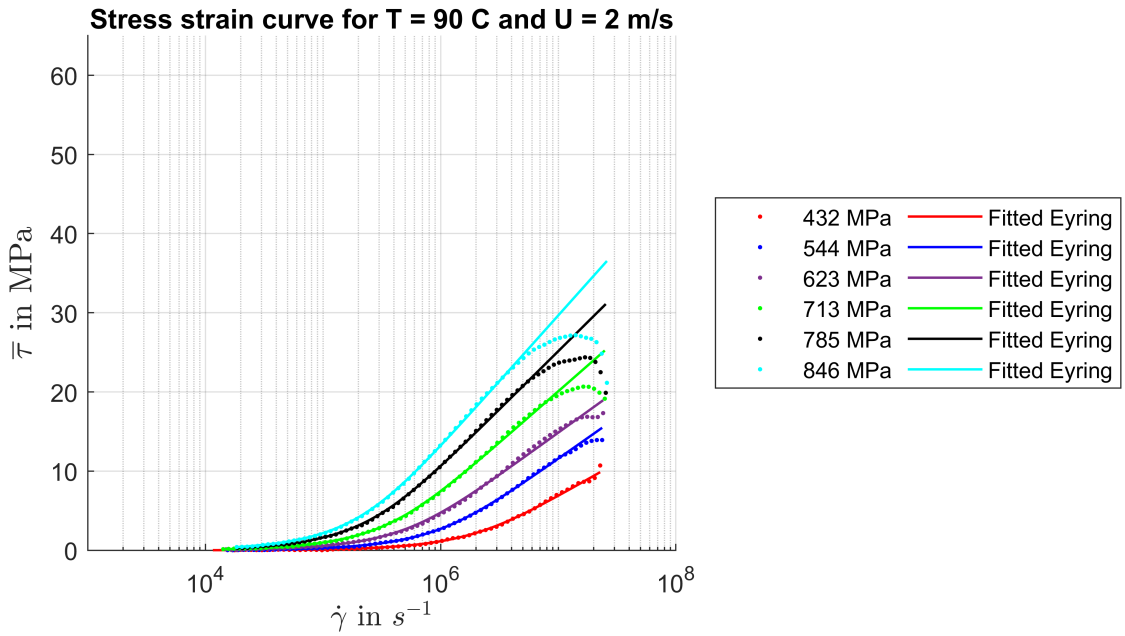
Stress strain curve for T = 90 C and U = 2 m/s
$\overline{\tau}$ in MPa
$\dot{\gamma}$ in s^{-1}
0
10
20
30
40
50
60
10^4
10^6
10^8
432 MPa
544 MPa
623 MPa
713 MPa
785 MPa
846 MPa
Fitted Eyring
Fitted Eyring
Fitted Eyring
Fitted Eyring
Fitted Eyring
Fitted Eyring

C Surface Roughness report

Report of surface roughness measurements of ball and disk from MTM with Sensofar

Measurements:

1. **New ball (50X lens)**

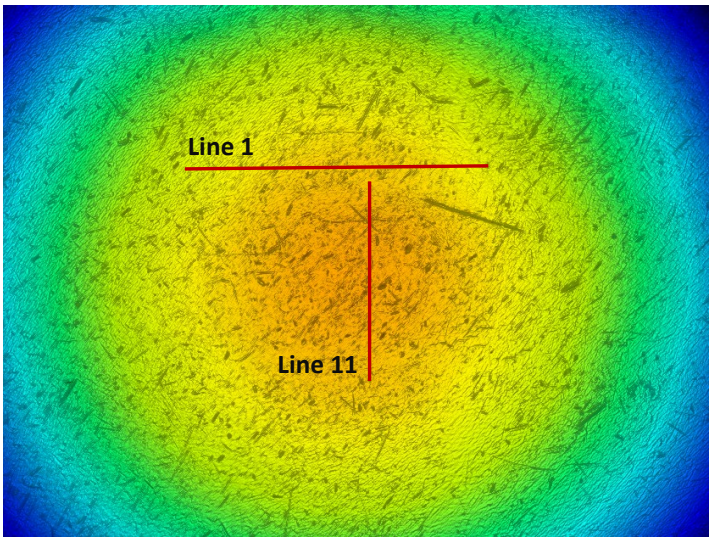

Line Number	Rq (nm)	Line Number	Rq (nm)	Line Number	Rq (nm)
Line 1	33	Line 7	26	Line 13	42
Line 2	31	Line 8	24	Line 14	30
Line 3	31	Line 9	25	Line 15	30
Line 4	28	Line 10	28	Line 16	26
Line 5	22	Line 11	28	Line 17	29
Line 6	29	Line 12	34	Line 18	22

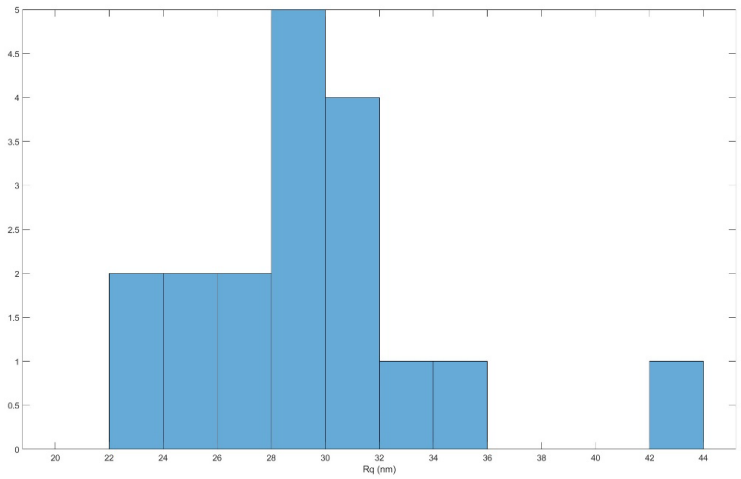

2. New disk (50X lens)

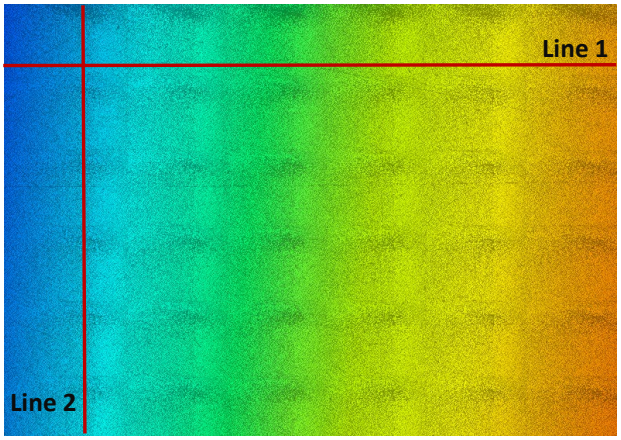

Line Number	Rq (nm)	Line Number	Rq (nm)	Line Number	Rq (nm)
Line 1	7	Line 7	6	Line 13	9
Line 2	6	Line 8	7	Line 14	19
Line 3	7	Line 9	6	Line 15	8
Line 4	6	Line 10	9	Line 16	17
Line 5	6	Line 11	7	Line 17	11
Line 6	7	Line 12	13	Line 18	12

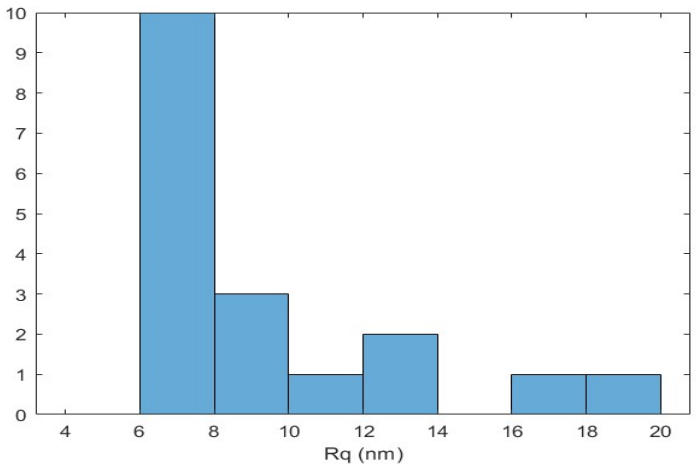

3. Used ball (50X lens)

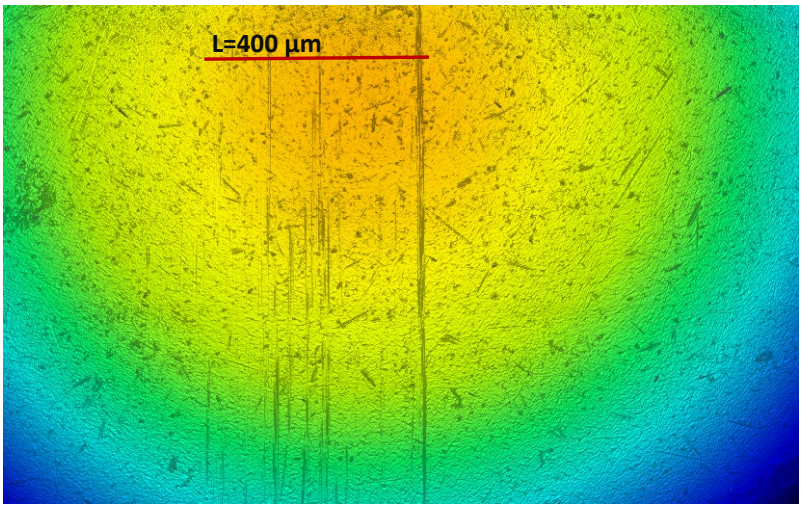

Line Number	Rq (nm)	Line Number	Rq (nm)	Line Number	Rq (nm)
Line 1	36	Line 7	29	Line 13	39
Line 2	39	Line 8	30	Line 14	48
Line 3	34	Line 9	32	Line 15	41
Line 4	36	Line 10	30	Line 16	34
Line 5	39	Line 11	28	Line 17	51
Line 6	43	Line 12	27	Line 18	36

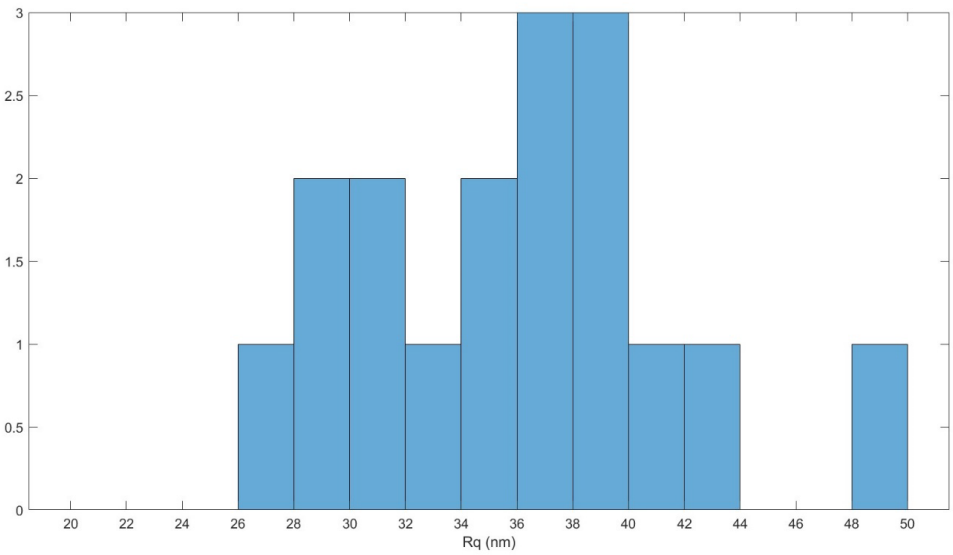

4. Used disk (50X lens)

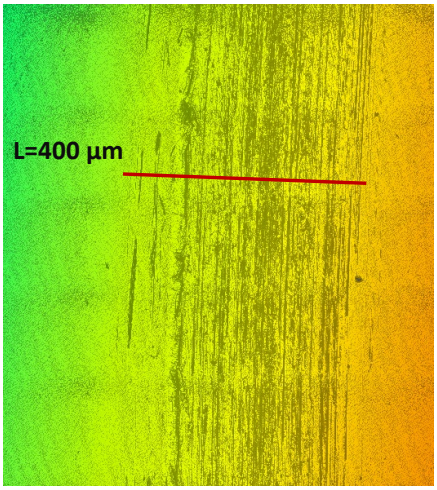

- **Region 1**

Line Number	Rq (nm)	Line Number	Rq (nm)	Line Number	Rq (nm)
Line 1	63	Line 7	34	Line 13	50
Line 2	43	Line 8	29	Line 14	56
Line 3	36	Line 9	38	Line 15	43
Line 4	69	Line 10	58	Line 16	37
Line 5	37	Line 11	38	Line 17	35
Line 6	34	Line 12	43	Line 18	48

- **Region 2**

Line Number	Rq (nm)	Line Number	Rq (nm)	Line Number	Rq (nm)
Line 1	32	Line 7	34	Line 13	58
Line 2	32	Line 8	49	Line 14	49
Line 3	26	Line 9	54	Line 15	52
Line 4	30	Line 10	67	Line 16	54
Line 5	26	Line 11	50	Line 17	62
Line 6	27	Line 12	51	Line 18	54

- **Region 3**

Line Number	Rq (nm)	Line Number	Rq (nm)	Line Number	Rq (nm)
Line 1	48	Line 7	62	Line 13	55
Line 2	54	Line 8	48	Line 14	42
Line 3	50	Line 9	52	Line 15	32
Line 4	60	Line 10	62	Line 16	64
Line 5	58	Line 11	58	Line 17	42
Line 6	58	Line 12	91	Line 18	48

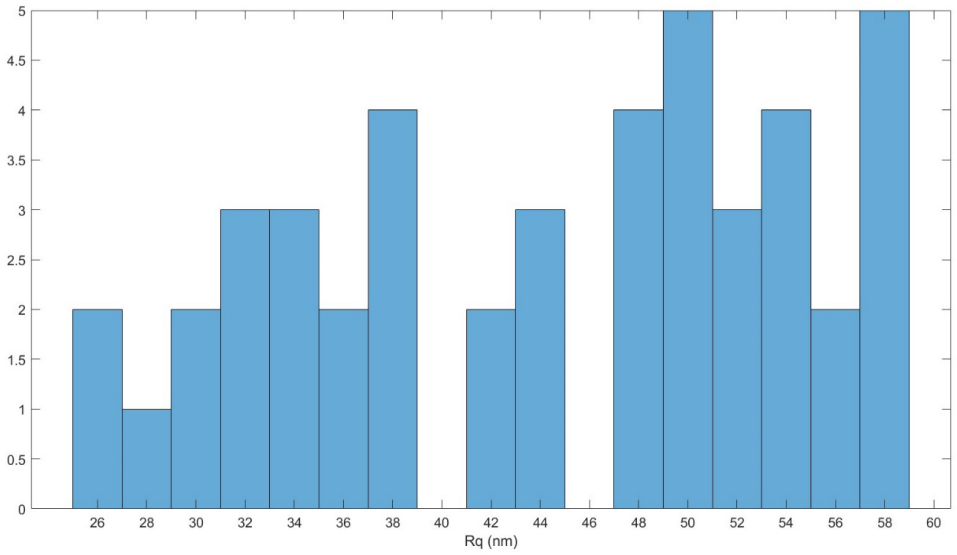

Results:

Sample	New ball	New disk	Used ball	Used disk
Rq by average (nm)	29	9	36	48

D Operational conditions cold mill

D.1 Cold mill 11

D.1.1 Stand 1

Geometry of the work roll and strip

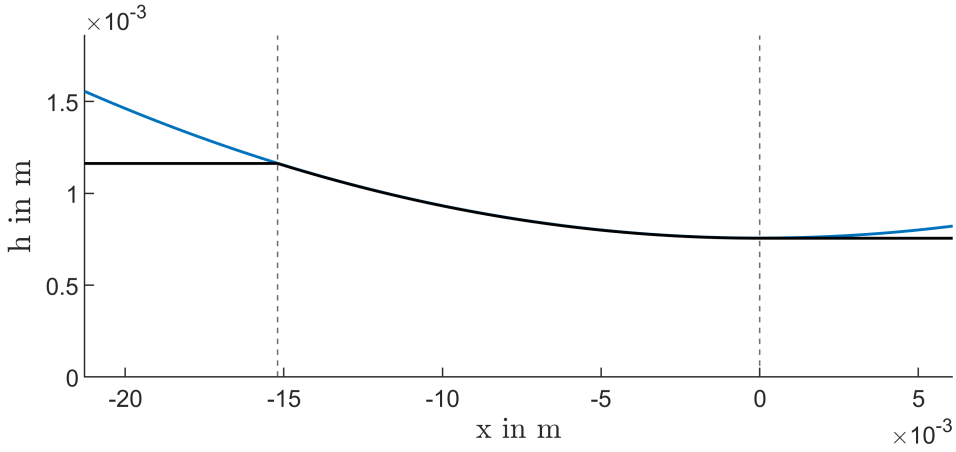

Velocity profile

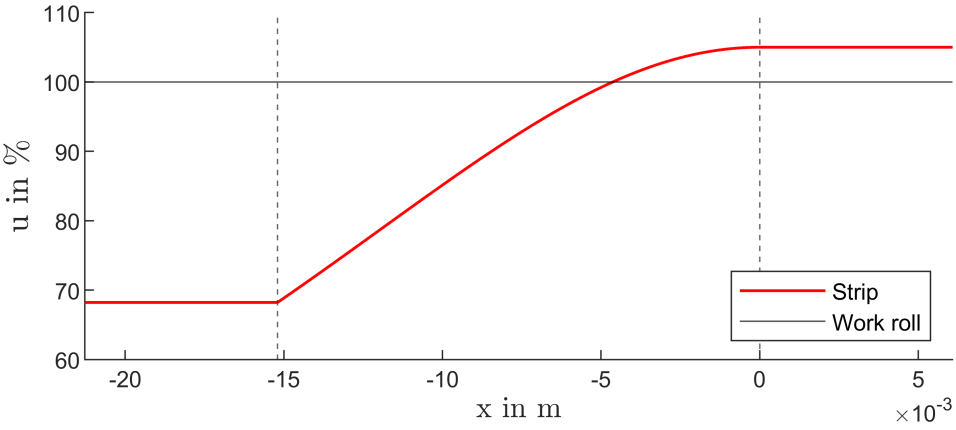

Shear rate profile

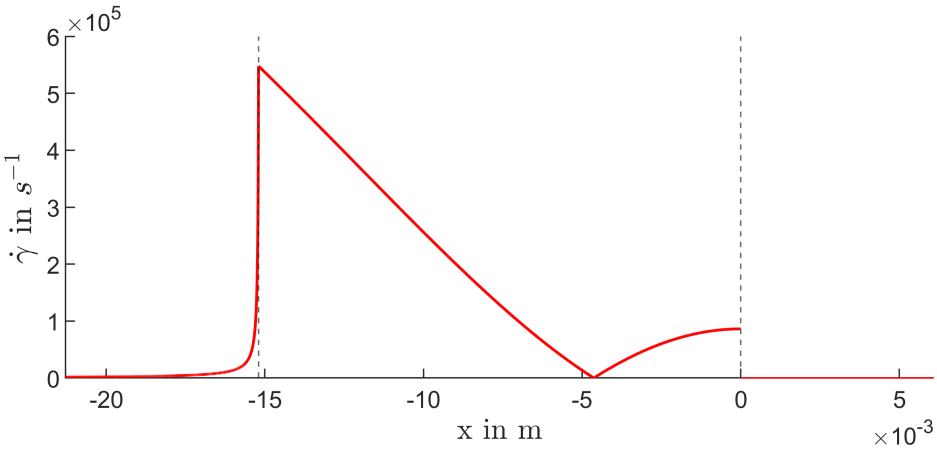

D.1.2 Stand 2

Geometry of the work roll and strip

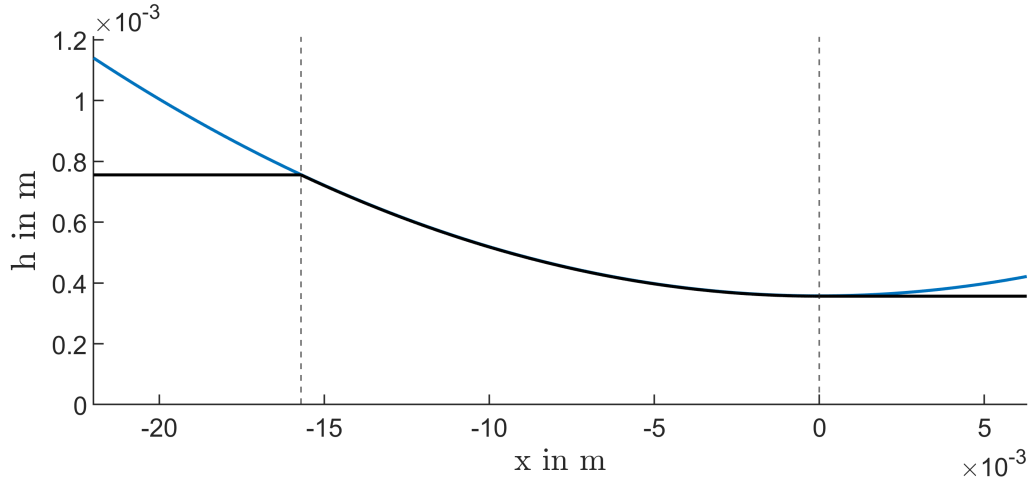

Velocity profile

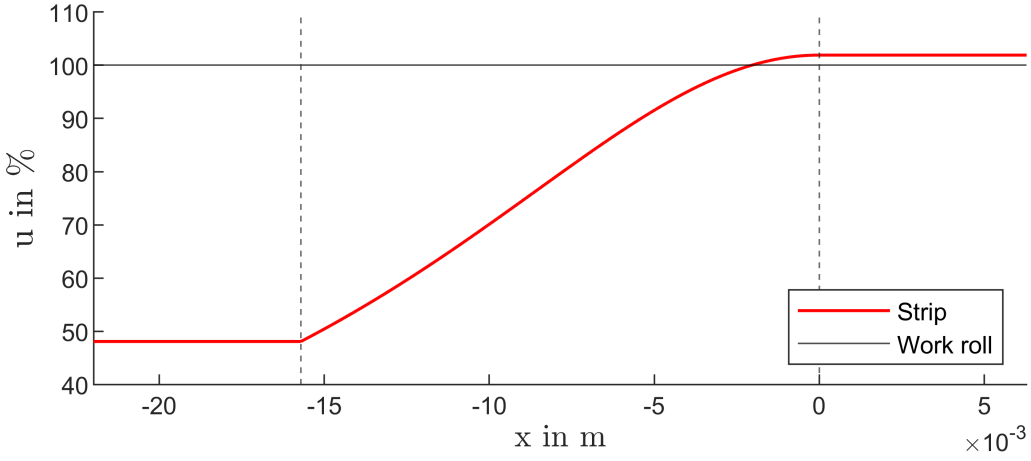

Shear rate profile

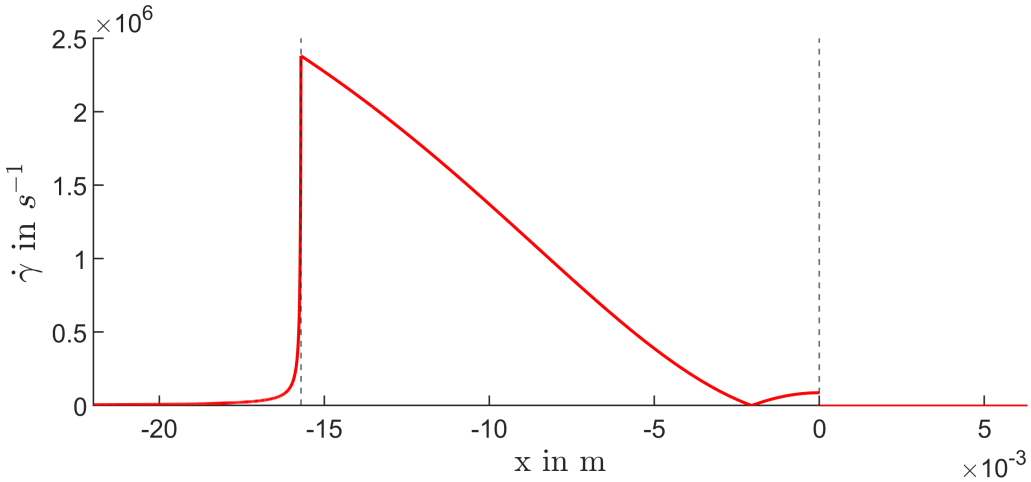

D.1.3 Stand 3

Geometry of the work roll and strip

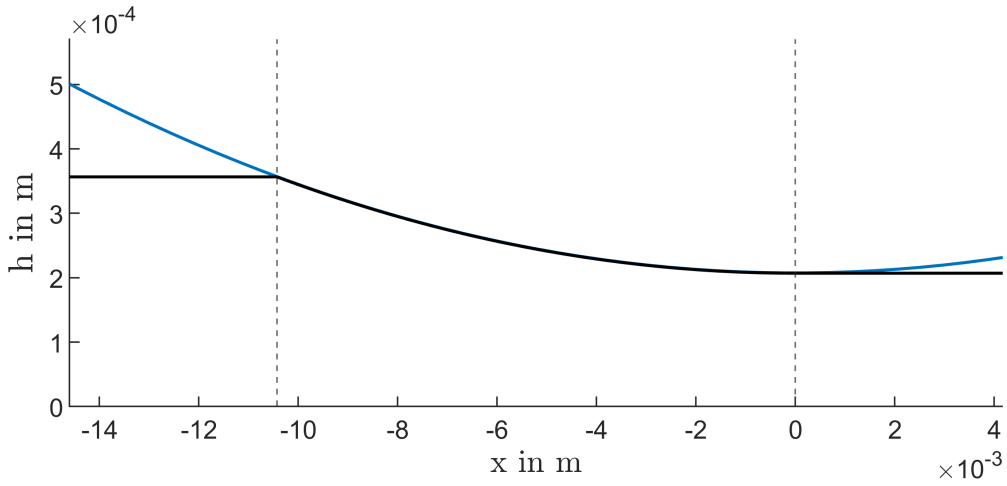

Velocity profile

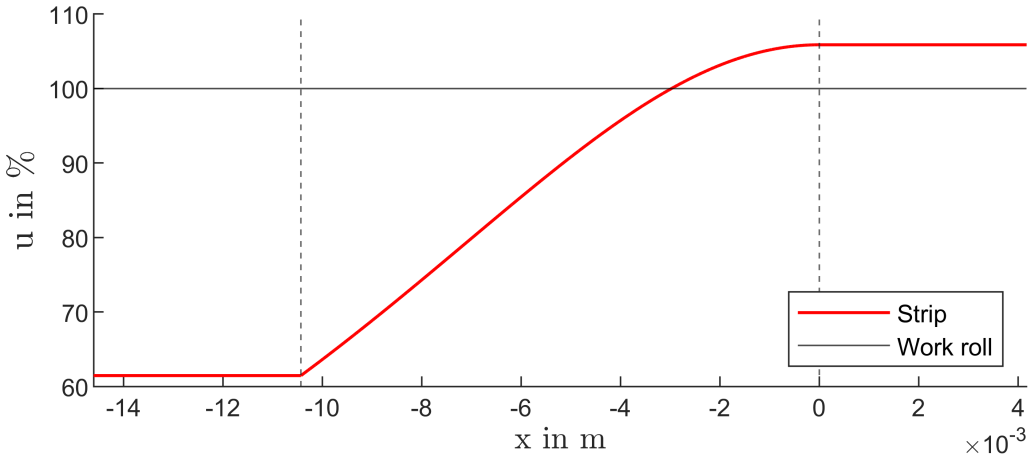

Shear rate profile

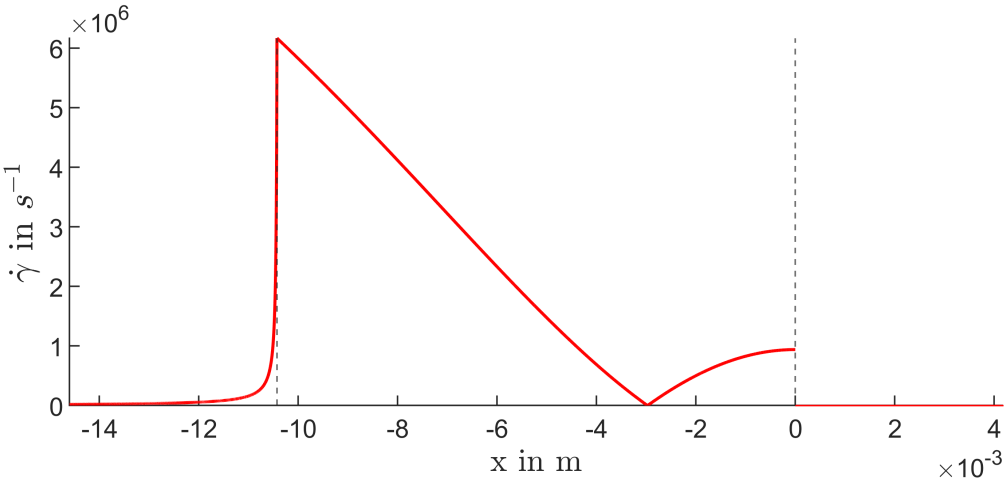

D.1.4 Stand 4

Geometry of the work roll and strip

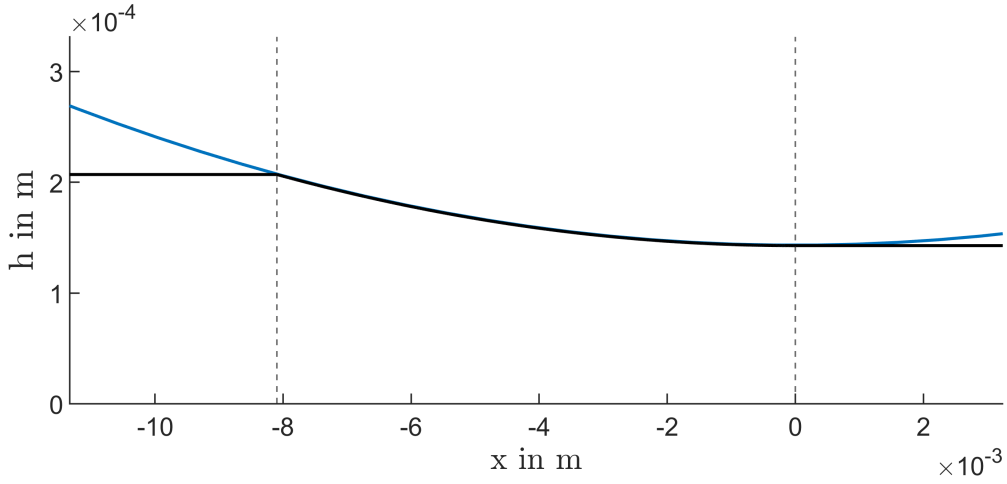

Velocity profile

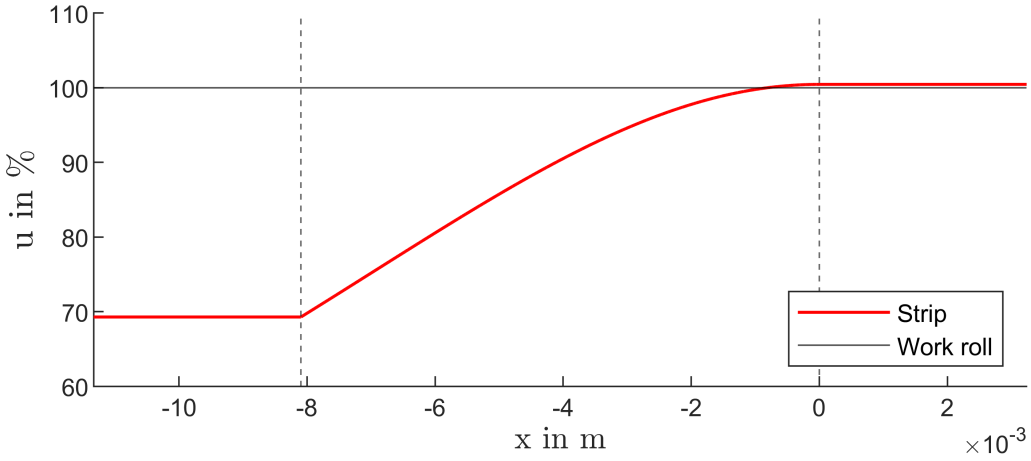

Shear rate profile

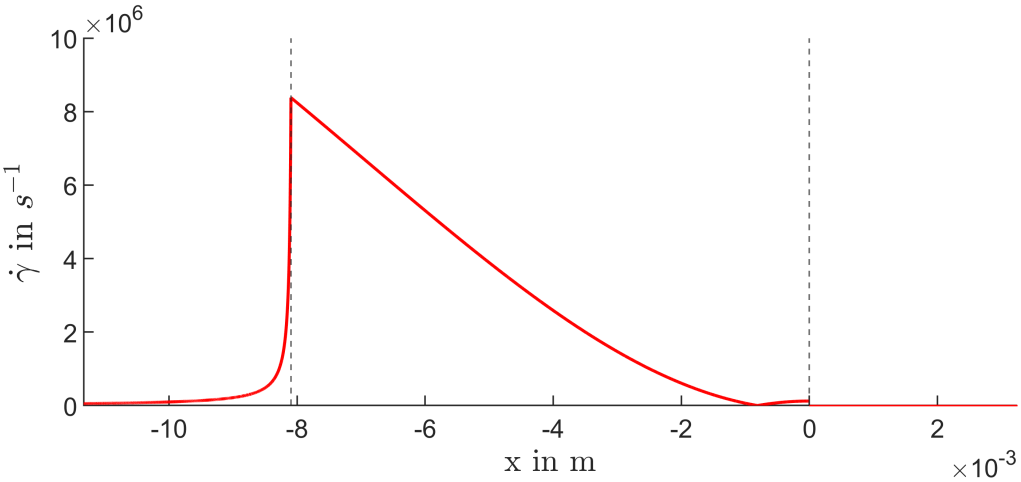

D.2 Cold mill 12

D.2.1 Stand 1

Geometry of the work roll and strip

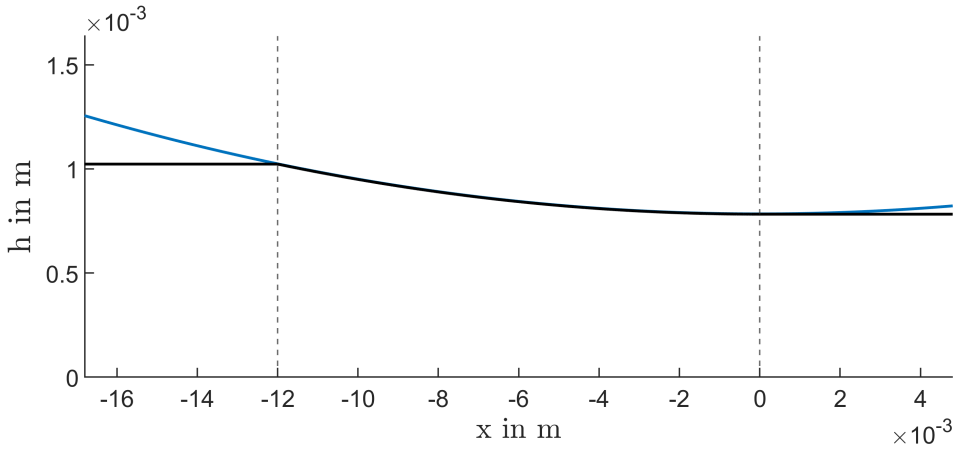

Velocity profile

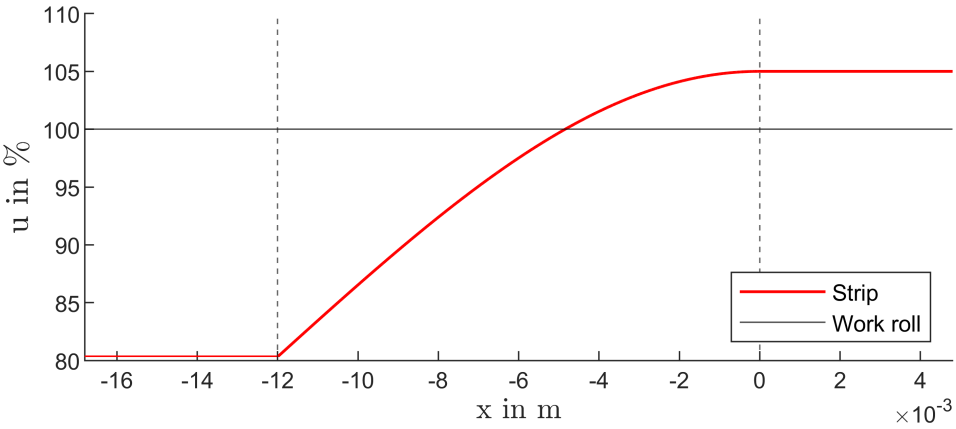

Shear rate profile

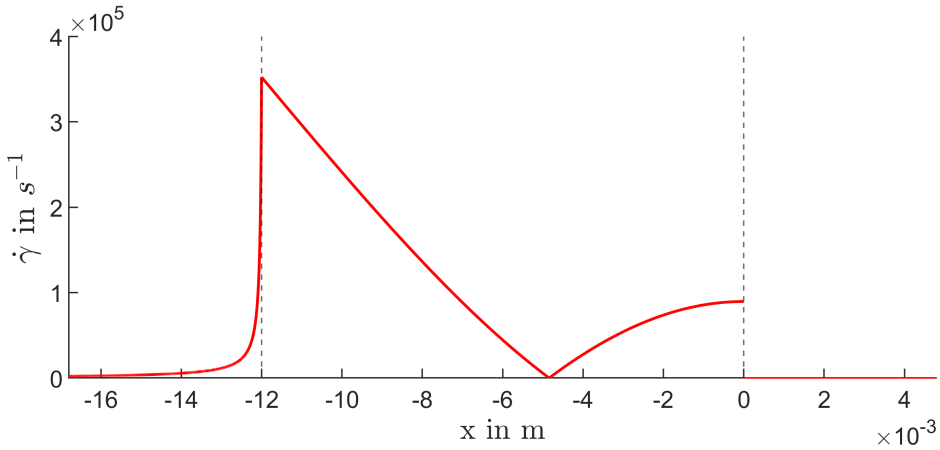

D.2.2 Stand 2

Geometry of the work roll and strip

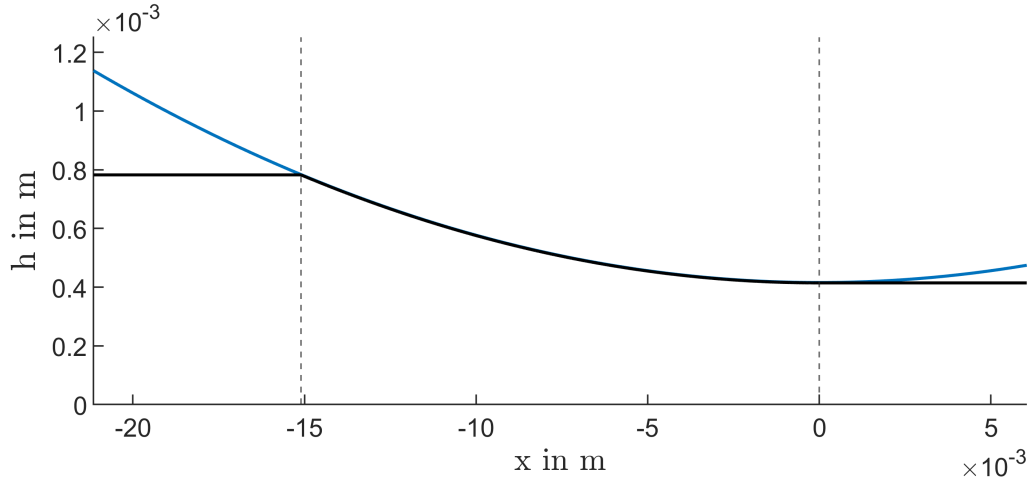

Velocity profile

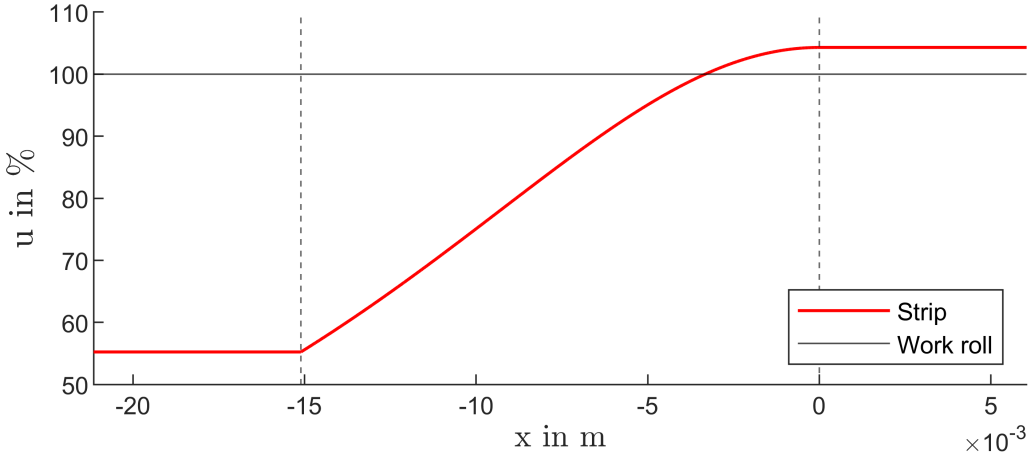

Shear rate profile

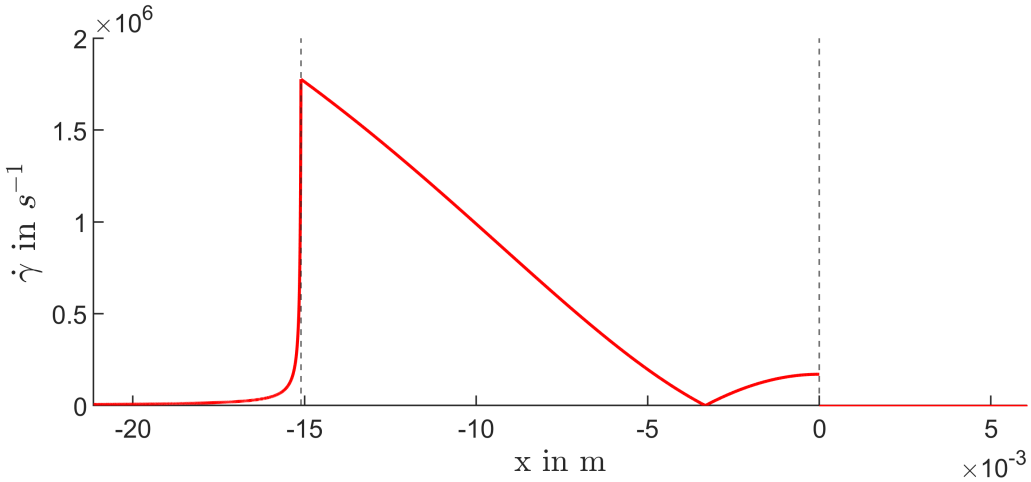

D.2.3 Stand 3

Geometry of the work roll and strip

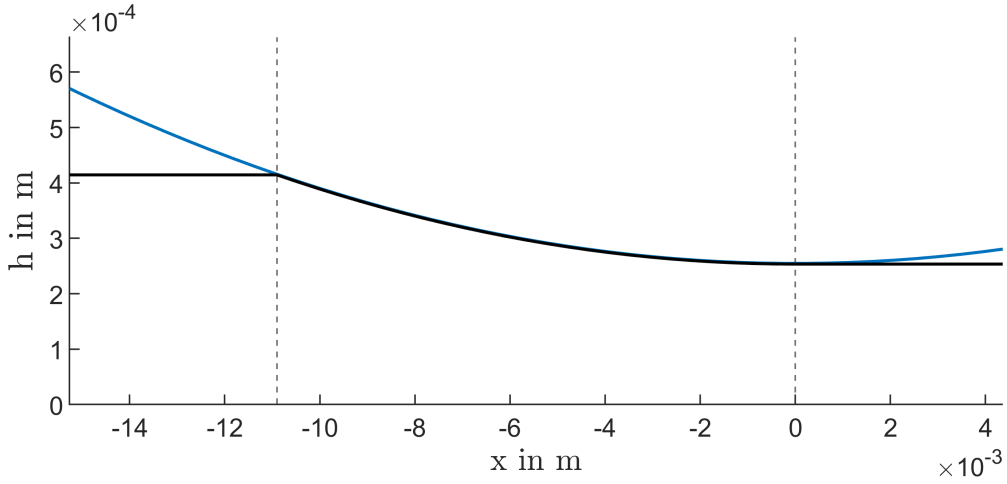

Velocity profile

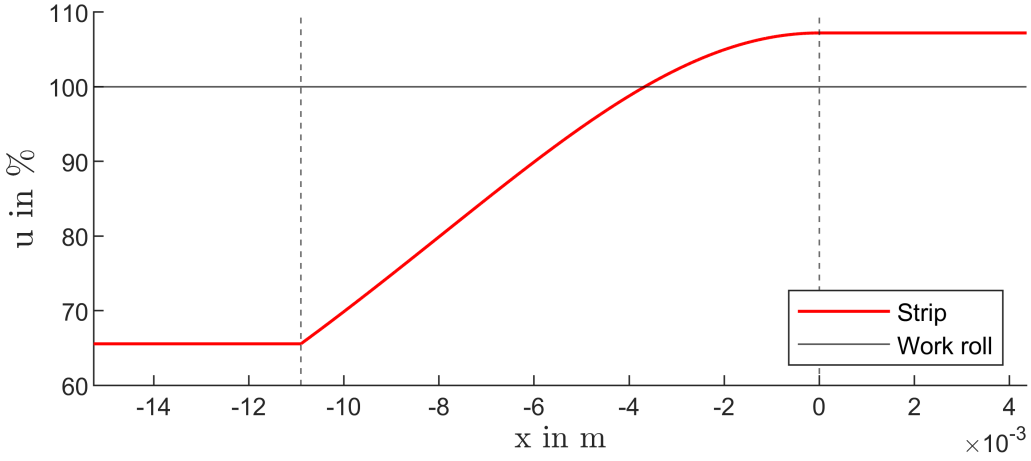

Shear rate profile

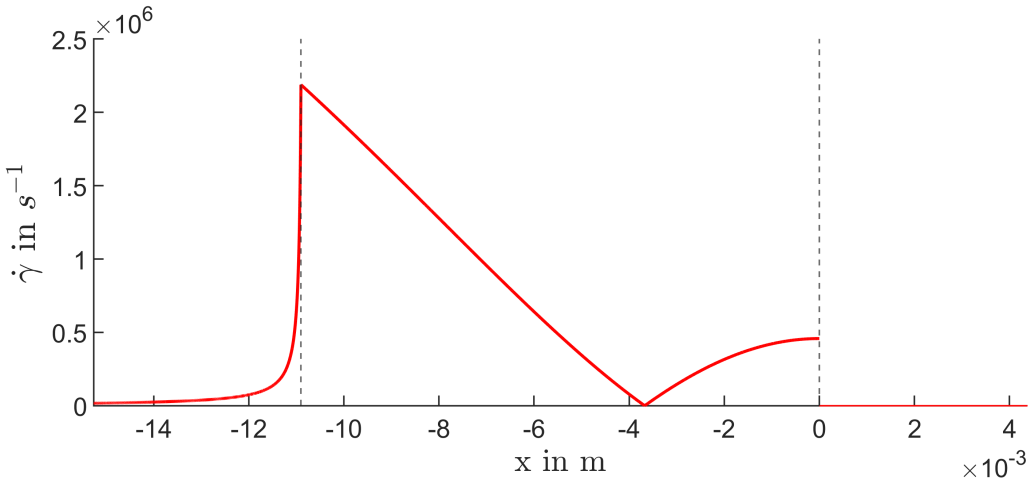

D.2.4 Stand 4

Geometry of the work roll and strip

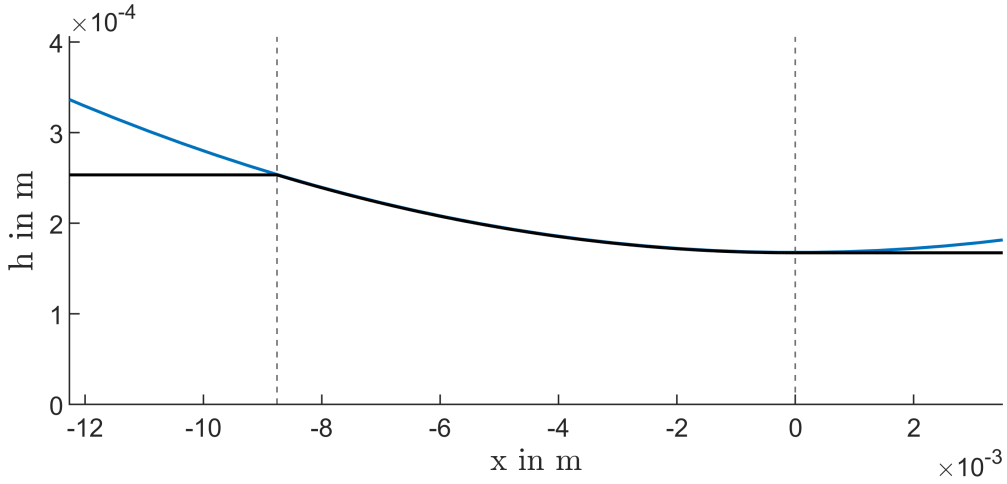

Velocity profile

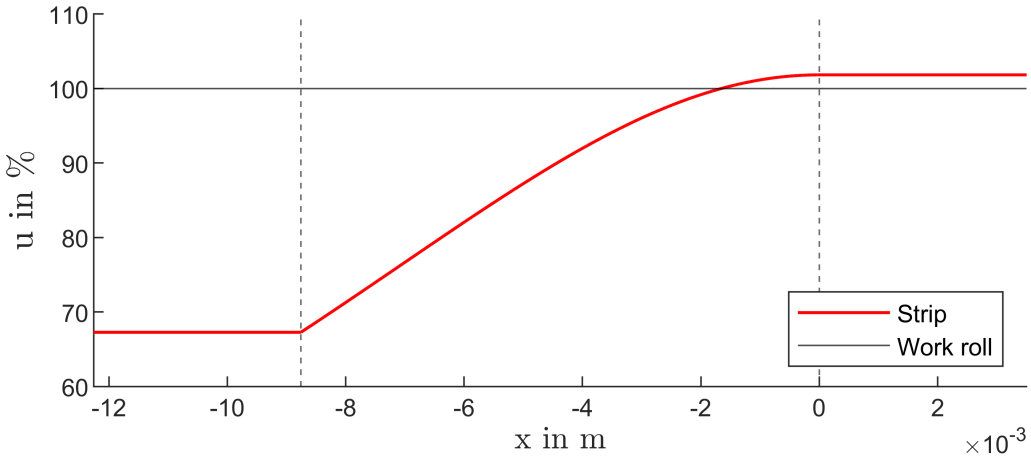

Shear rate profile

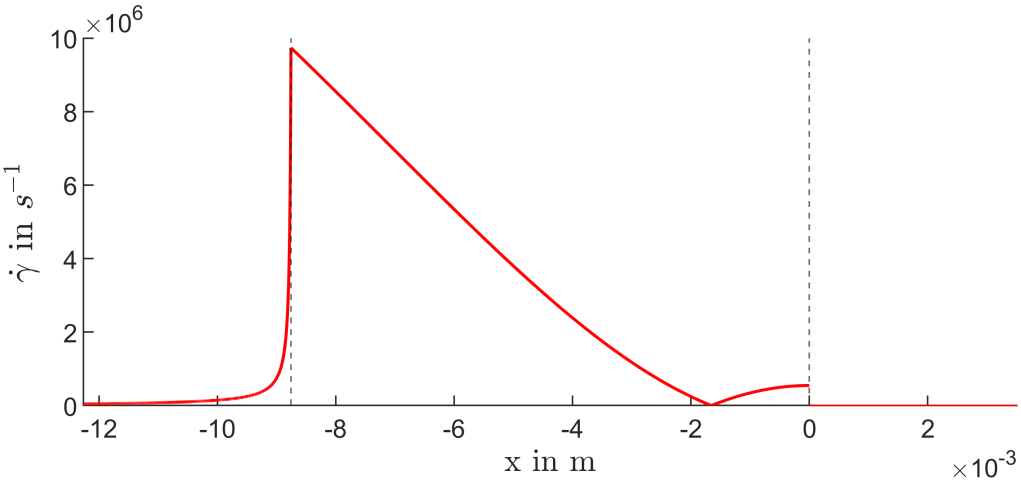

D.2.5 Stand 5

Geometry of the work roll and strip

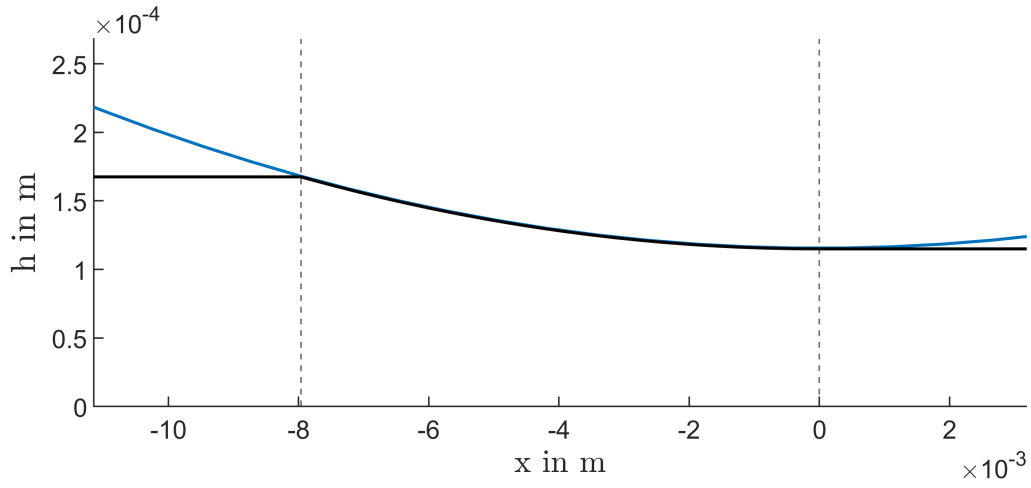

Velocity profile

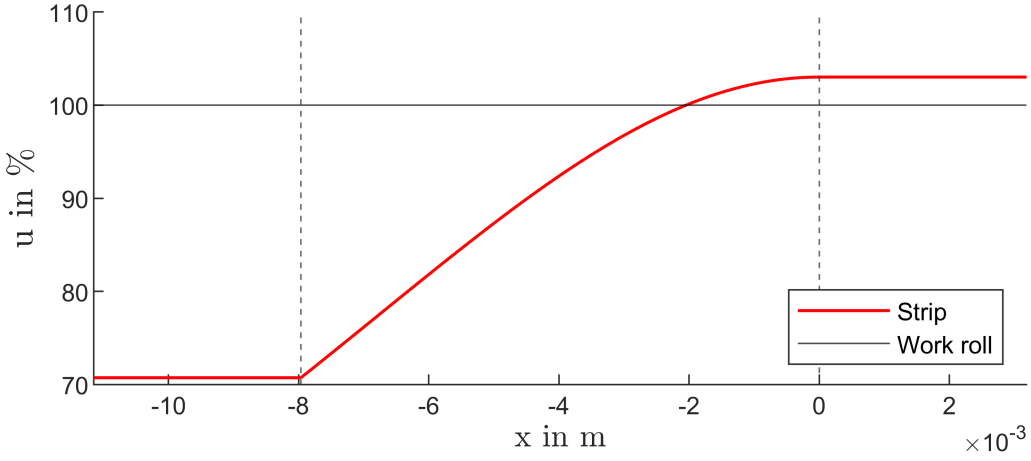

Shear rate profile